UNIVERSITÀ DEGLI STUDI DI PADOVA

DIPARTIMENTO DI GEOSCIENZE

Surface and borehole ERT for hydrological characterisation of the near surface

Master's thesis in Geology and Technical Geology (LM-74)

Supervisors: Professor Jacopo Boaga (University of Padua)
Professor Andreas Kemna (University of Bonn)

Student: Mirko Pavoni (1190610)

Graduation session: 25/09/2020

THESIS INDEX

INDEX OF IMAGES

Chapter 1

Chapter 2

Chapter 3

Chapter 4

INDEX OF TABLES

Chapter 1

Chapter 2

Chapter 3

Chapter 4

1. INTRODUCTION

The main aim of the thesis will be to analyze the advantages and disadvantages of the geophysical technique ERT (ELECTRICAL RESISTIVITY TOMOGRAPHY) in the context of near surface environmental investigations. In the first part of the document a detailed description of the direct current (DC) resistivity method will be presented. We will show (1) the physical principles that rule the propagation of current lines in the subsoil (the three empirical Ohm's laws, Laplace equation and Poisson equation); (2) the different technique and configurations (Wenner, Dipole-dipole, etc) that can be used to collect datasets on the field, focusing particularly on the ERT surface based imaging, ERT borehole based imaging and ERT time-lapse imaging, showing the advantages and disadvantages of each technique and configuration; (3) the importance of defining the correct quality (error) of DC resistivity measurements through the processes of stacking and mostly with reciprocal measurements, as this information is necessary during the inversion process to define a satisfactory misfit between the model prediction and the measured data; (4) the features of the multielectrode instruments and a comparison between the performance of the two owned by the Geosciences Department of Padua (MAE X612EM + and Iris Syscal Pro), with an example of a real study case carried out with both the instruments during my bachelor thesis; (5) a detailed description of the numerical methods (finite differences and finite elements) that are usually applied by the electrical inversion codes; (6) the forward modelling procedure to calculate numerically the synthetic dataset for a fixed subsoil model and electrode configuration; (7) the inverse modelling procedure to calculate the distribution of electrical properties (resistivity or conductivity) of the investigated subsoil; (8) the sensitivity of the resistivity section obtained with the inversion process; (9) the importance of using priori information about the survey site before the measurements and even during the inversion process; (10) the rise of inversion artifacts if the error level of the dataset is not correctly defined.

In the second part of the thesis we will deal with the problem of correctly defining the thickness of conductive clay layers interspersed in more resistive ones (e.g. gravels). In hydrogeological and environmental investigations this is an important issue as the clay layer can act as an aquiclude. Initially, we will deal with this kind of problem through the uses of direct models and we will explore the possible strategies to face the situation. It will be highlighted the effect on ERT surface surveys (with different length of the electrodes line, spacing and configurations) to insert a conductive clay layers, of different thicknesses and at different depths, in a subsoil model with greater resistivities. Subsequently, the same subsoil models will be studied with the ERT cross-borehole technique, to verify if this can improve the inversion results. Furthermore, the ERT technique will be assessed to detect discontinuities of the clay layer due, for instance, to the presence of paleochannels. The discontinuities of the clay layers are very problematic as regards the underground hydrology since they can't act perfectly as an aquiclude and therefore they can allow the communication between surface sources of contaminants and deep aquifers. After the forward modelling analysis, we will present an example of a real study case, performed in the province of Pordenone (NE Italy), where both the ERT technique, surface and cross-borehole, have been realized with a subsoil structure similar to the models that we previously described (clay layer placed between two more resistive layers of gravel). Moreover, we will show the results of a time-lapse ERT acquisition, realized in the same investigation site with the cross-borehole configuration, for a controlled irrigation experiment aimed to verify the correct working of a draining trench.

2. DIRECT CURRENT RESISTIVITY METHOD

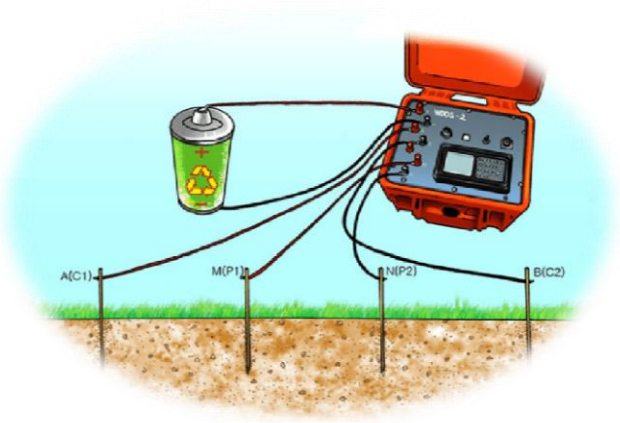

Electrical methods are probably the most widely used near-surface geophysical techniques, certainly for environmental investigations. This is because (1) subsurface electrical properties are often well correlated to the physical and chemical properties of fluids within the pore space (e.g. saturation and salinity) and lithologic properties (e.g. porosity and clay content); (2) the theoretical concepts are relatively straightforward; (3) field measurement techniques are highly scalable, allowing investigations to depths of tens of centimeters to hundreds of meters; (4) instrumentation is relatively low cost and, for DC resistivity at least, straightforward to operate; (5) data analysis techniques have matured robust data inversion tools and are widely available (Binley, 2015).

Modern electrical methods are widely assumed to originate from the work in 1912 by Conrad Schlumberger, who developed a means of metallic ore prospecting using a four-electrode array. Nevertheless, Alfred Williams and Leo Daft developed an electrical prospecting approach in the late nineteenth century and in 1901 formed 'The Electrical Ore-Finding Company Ltd,' which unfortunately proved to have limited success, despite attempts to apply their approach internationally (Vernon, 2008). The company went into receivership in 1905, however, the Daft and Williams equipment and method were adopted and developed in Sweden and elsewhere (Dahlin, 2001). Nevertheless, Schlumberger truly pioneered a successful electrical prospecting method, and throughout the first half of the twentieth century, electrical methods remained relatively similar to the original Schlumberger approach. Only in the last decade, the advent of instrument developments and robust inversion tools, led to a rapid growth in the use of electrical imaging systems. New imaging techniques, such as electrical resistivity tomography (ERT), has improved the applicability of the geoelectrical methods to particular hydrogeological and environmental problems, as the contamination of the subsurface soil or/and ground water from anthropogenic sources (wastes, chemicals, fuels, etc). ERT technique has been successfully applied to the study of fluid flow inside porous and fractured sediments (e.g. Daily et al., 1992; Binley et al., 1996; Slater et al., 1997), to detect and map subsurface contaminant plumes (e.g. Daily et al., 1995; Ramirez et al., 1996) and to monitor contaminant remediation process (e.g. La Brecque et al., 1996).

Electrical properties of the soils may be either investigated passively, as in the self-potential method or actively by the injection of current (low-frequency alternating-current, < 1 kHz) into the ground, as in the resistivity and induced polarization (IP) methods. The direct current (DC) resistivity method, commonly used in professional field, investigates the primary conduction phenomena in terms of signal amplitudes, whereas in the IP methods secondary polarization effects are measured in terms of time-domain discharge curves or frequency-domain phase shifts (Kemna , 2000).

2.1 Physical Principles

Any kind of soil (or rock) offers a certain resistance to the passage of current, therefore we can consider them as ohmic conductors. Considering a homogeneous and isotropic medium, the following Figure 2.1 can be used to define the three empirical Ohm's laws:

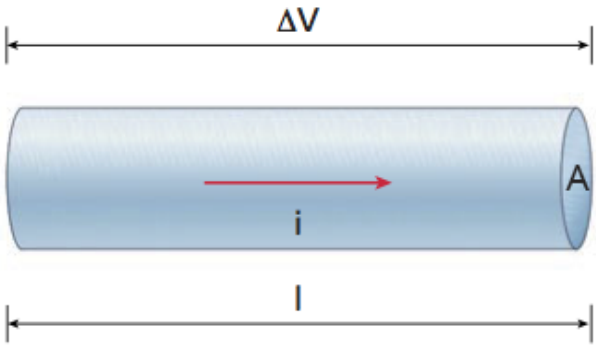

Figure 2.1 Homogeneous-conductive thread

(2.1) First Ohm's law:	$\Delta V = \frac{R}{i}$	where	ΔV = potential difference [V] R = resistance [Ω] i = current intensity [A]
(2.2) Second Ohm's law:	$R = \rho \frac{l}{A}$	where	l = length of the conductive thread [m] A = thread section [m^2] ρ = resistivity [Ω*m]
(2.3) Third Ohm's law:	$j = \frac{i}{A} = \sigma * E$	where	j = current flow [A/m^2] $E = \frac{\Delta V}{l}$ = electric field [V/m] $\sigma = \frac{1}{\rho}$ = conductivity [S/m]

From equation 2.2 it's clear that the electrical resistance of a material depends not only on its physical properties but also on its geometric characteristics. In geophysics it is therefore more practical to use the resistivity, physical parameter independent from the geometry of the medium and linked only to the natural composition of the material. Electrical resistivity is a quantitative measure of the ability of a material to resist the flow of electrical charges within it. On the contrary, conductivity quantifies the ability of a material to be crossed by electric current. The resistivity of a soils and rocks depends on various factors such as mineralogical composition, porosity, presence of fluids and their own conductivity, degree of fracturing, degree of saturation as well as presence of organic substances (hydrocarbons, solvents, etc.). Unconsolidated sediments generally have lower resistivity than rocks, however, precisely for the reason that they are not consolidated, it is more difficult to estimate the value of their resistivity, which is very influenced by the porosity, degree of saturation and the clay content (clay soils commonly have lower resistivity values than sandy soils).

Due to these considerations, it's clear that there isn't one-to-one correspondence between the resistivity value and the kind of soil/rock. In the following Table 2.1 is possible to appreciate how the resistivity values can be very different considering the same lithology:

LITHOLOGY	RESISTIVITY RANGE
Sandstone	60 – 10^4 Ω*m
Clay	1 – 120 Ω*m
Sand	100 – 1000 Ω*m
Silt	10 - 800 Ω*m
Gravel	100-5000 Ω*m
Limestone	100 – 5000 Ω*m
Basalt	10 – 10^5 Ω*m
Marble	100 – 10^8 Ω*m
Granite	100 – 10^6 Ω*m

Table 2.1 Resistivity ranges for some type of rocks and soils

If we consider the injection of current into a homogeneous medium through an electric monopole, as shown in Figure 2.2, the single electrode acts as a point source of power lines, which are radially distributed into the half-space. The electrical potential of a generic point, inside the half-space, decreases moving away from the source and the equipotential surfaces (lines in 2D), always orthogonal to the flow lines, are those of concentric hemispheres with respect to the electrode.

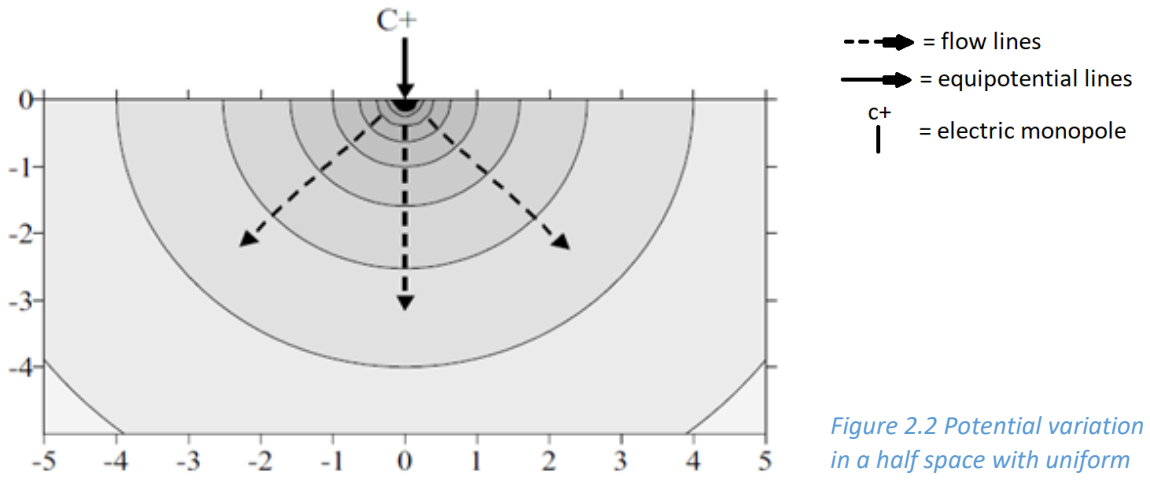

Figure 2.2 Potential variation in a half space with uniform resistivity distribution

According to equation 2.3, the current flow that passes through an equipotential surface is: j = $\frac{i}{2\pi r^2}$ where r is the radius of the hemisphere. Voltage can be considered as the work done by the electric field E to move a charge from ∞ to a distance r and can be expressed as:

$$(2.4) \quad V = \int_r^\infty E\, dr = \int_r^\infty \rho * j\, dr = \int_r^\infty \frac{\rho * i}{2\pi r^2}\, dr = \frac{\rho * i}{2\pi r}$$

The electric monopole just described is an ideal situation, to have current circulation it is necessary to have an electric dipole. If we consider two electrodes, A and B, characterized by a potential difference (e.g. 12V - applied by a battery), the power lines will pass through the medium going from the electrode with greater potential (positive pole A) to the electrode with less potential (negative pole B). The intensity of the electric current i, which flows into the medium, can be measured with an ammeter. The equipotential surfaces (lines in 2D) of the two poles are not those of perfect hemispheres and they cancel each other out at the center of the device. If we consider another pair of electrodes, M and N, a certain potential difference ΔV will arise between them, due to the electric current i circulating into the medium. It's possible to measure the potential difference ΔV of the two poles M-N with a voltmeter. In Figure 2.3 we can appreciate the acquisition scheme:

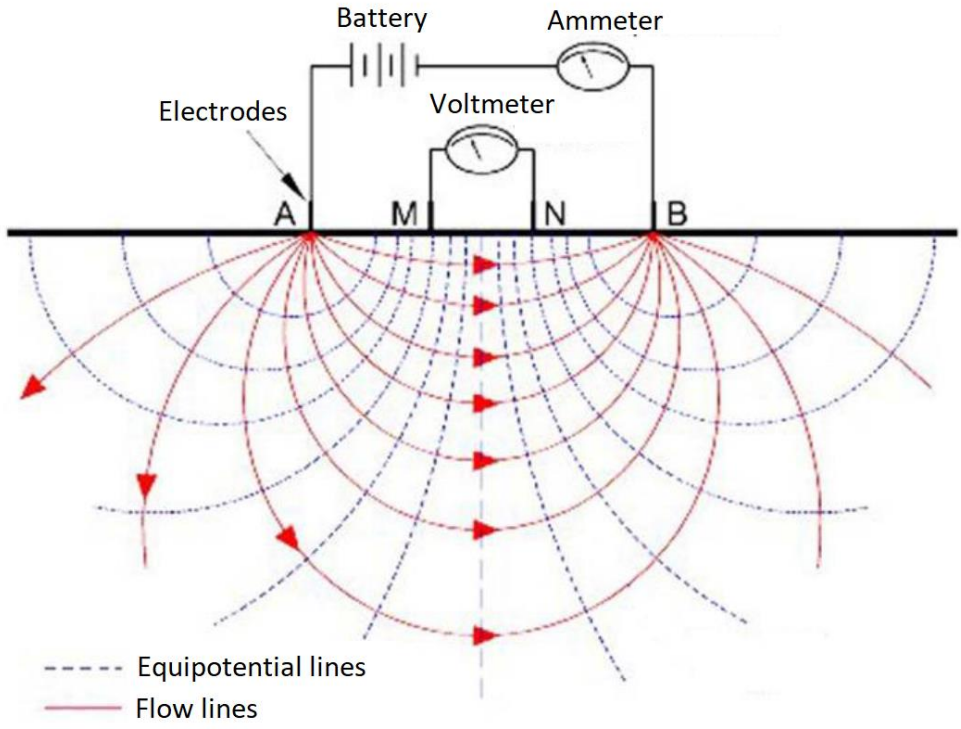

Figure 2.3 Schematization for DC resistivity method measurements

From a mathematical point of view, we can define the potential in M using the equation 2.4:

V(A,M) = Potential in M due to A = $\frac{\rho * i}{2\pi AM}$ where AM is the distance between electrodes A and M;
V(B,M) = Potential in M due to B = $-\frac{\rho * i}{2\pi BM}$ where BM is the distance between electrodes B and M;

$$(2.5)\quad V(M) = \frac{\rho * i}{2\pi}\left(\frac{1}{AM} - \frac{1}{BM}\right)$$

The same procedure can also be applied to the electrode N:

V(A,N) = Potential in N due to A = $\frac{\rho * i}{2\pi AN}$ where AN is the distance between electrodes A and N;
V(B,N) = Potential in N due to B = $-\frac{\rho * i}{2\pi BN}$ where BN is the distance between electrodes B and N;

$$(2.6)\quad V(N) = \frac{\rho * i}{2\pi}\left(\frac{1}{AN} - \frac{1}{BN}\right)$$

Therefore, the potential difference (ΔV) measured between M and N can be calculated as:

$$(2.7)\quad \Delta V = V(M) - V(N) = \frac{\rho * i}{2\pi}\left(\frac{1}{AM} - \frac{1}{BM} - \frac{1}{AN} + \frac{1}{BN}\right)$$

The geometric factor K is defined as:

$$(2.8)\quad K = 2\pi\left(\frac{1}{AM} - \frac{1}{BM} - \frac{1}{AN} + \frac{1}{BN}\right)^{-1}$$

ΔV - i - K are known, they are measured, so it is possible to compute the resistivity of the medium:

$$(2.9)\quad \rho_a = \frac{\Delta V}{i} K$$

The calculated resistivity is the real one only if the medium is homogeneous and isotropic. If the measurements are performed in the field, these conditions are hardly realized because the soils are typically heterogeneous. The measured resistivity is influenced by the contribution of the different resistivities of the elements present in the subsoil. Furthermore, the resistivity calculated with the equation 2.9 considers the electrodes placed on a flat surface, also this condition is not always realized on the field and the preferential distribution of the flow lines in the topographic lows influences the measurement. For these reasons the measured resistivity is defined as apparent and to obtain a real resistivity model of the subsoil an inversion process is necessary (it will be described in chapter 2.5).

2.2 Measurements Practices

2.2.1 Surface-Based Imaging

The easiest way to determinate the apparent resistivity in the field is to use the four-electrode configuration 'quadrapole', as described in the previous chapter 2.1. The electrodes used for the measurements are typically stainless-steel stakes. The size of the stakes will depend on the survey scale. For most near-surface studies, electrodes are typically 1 cm in diameter, 30 cm long and pushed in the ground for no more than 10 cm. The use of stainless steel prevents corrosion on the electrodes, which can be problematic for the potential electrodes as the chemical reactions will lead to electrochemical signals that could influence the measurements. In addition, any coating on the electrode will influence the contact between the electrode and the soil. The electrical resistance across this contact should not be too high, less than a few kΩ, otherwise the voltage that we measure will be influenced (Binley, 2015). To avoid polarization of the electrodes, an alternating power source is utilized. A switched square wave, as shown in Figure 2.4, is the most common current waveform and it is generally applied at frequencies of about 0.5 to 5 Hz.

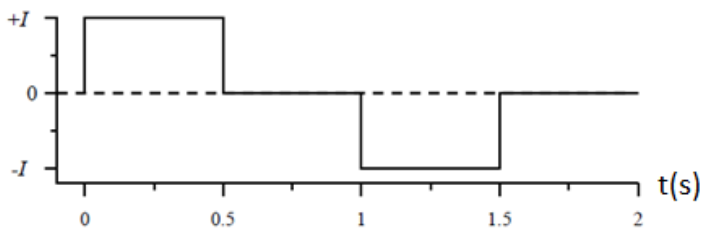

Figure 2.4 Typical current waveforms for DC resistivity measurements

The potential difference (ΔV) measured at the potentiometric electrodes (M-N), and therefore the apparent resistivity calculated, is influenced by the distribution of the power lines in the subsoil. This distribution depends on several factors:

- The characteristics of investigated subsoil. As we can see in Figures 2.5, there is a preferential distribution of the flow lines in the most conductive medium (1).

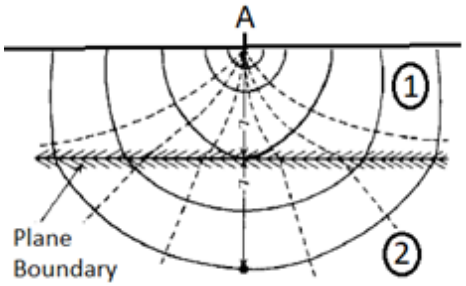

Figure 2.5 Schematization of the preferential distribution of the flow lines in the upper and most conductive medium (1)

= Flow lines
= Equipotential lines

- The distance between the electrodes. As we can see in Figure 2.6, greater is the separation between electrodes A and B, greater is the diffusion of the flow lines in the ground and consequently the depth of the investigation.

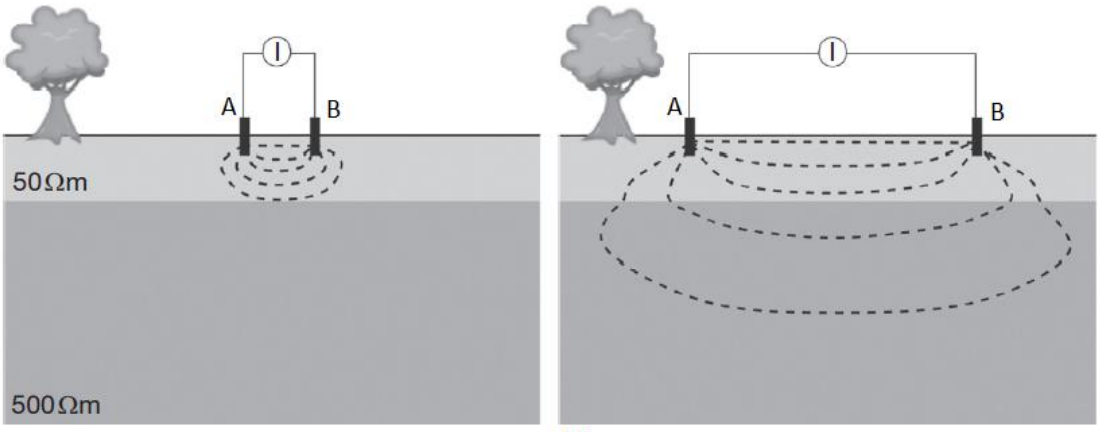

Figure 2.6 Schematization of the distribution of the flow lines in response of the different distance of the electrodes A-B

- The topography. As we can see in Figure 2.7, even in a homogeneous medium there is a preferential distribution of the flow lines in the topographic lows. The position of each electrode must be perfectly known (this is an important input data for the inversion codes).

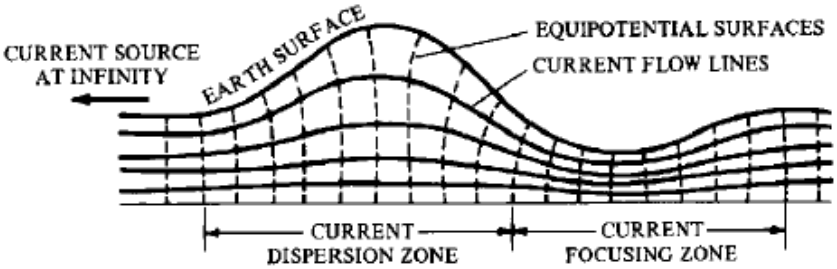

Figure 2.7 Schematization of the distribution of the flow lines in a homogeneous medium with an irregular topography

- The geometric configuration of the electrode quadrapole. There are different kind of geometries that can be used in the field for ground-based studies, for instance the Wenner and Dipole–dipole arrays. As we can see in Figure 2.8, for each configuration there is a different distribution of the flow lines in the subsoil.

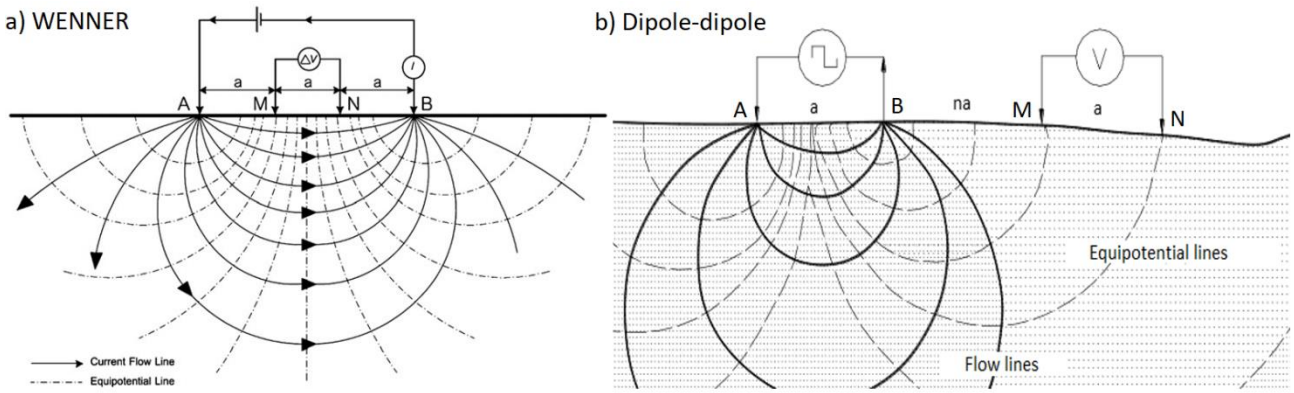

Figure 2.8 Examples of electrode quadrapole geometries: (a) Wenner and (b) Dipole-dipole

In the Wenner array configuration, the distances A-M, M-N, and B-N are all equal to a value *a*. If we apply equation 2.8, in order to get the geometric factor K, the apparent resistivity for this configuration can be expressed as:

$$\rho_a = \frac{2\pi a \Delta V}{i} \quad (2.10)$$

In the dipole–dipole array configuration, the current electrode dipole A-B is adjacent to the potential electrode dipole M-N, the dipoles have an equal width *a* and are separated by a distance *na*. In this case, the apparent resistivity can be written as:

$$\rho_a = \pi n(n+1)(n+2)a\frac{\Delta V}{i} \quad (2.11)$$

The different geometries have advantages and disadvantages, the choice of the configuration should be based on the target of the investigation and expected signal strength. Figure 2.9 shows an example of sensitivity patterns for the Wenner and Dipole–dipole configurations:

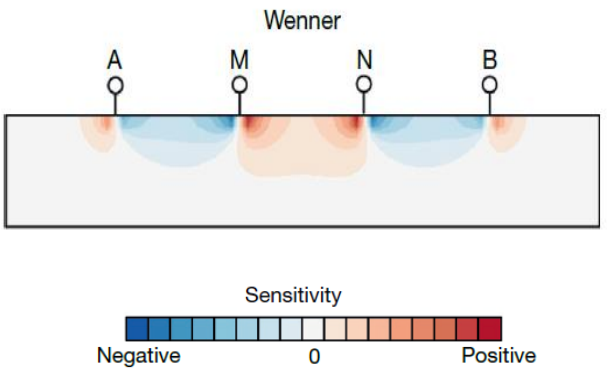

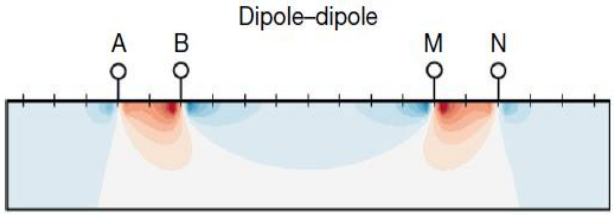

Figure 2.9 Sensitivity patterns for Wenner and Dipole-dipole arrays in a homogeneous medium

The Figure 2.9 highlights the greater lateral sensitivity of the Dipole–dipole array, in contrast to the Wenner configuration which shows a better vertical sensitivity. The Wenner configuration is more suitable if horizontal structures (such as stratifications) need to be identified. Instead, as regards the identification of vertical structures (with horizontal variations of resistivity – such as faults or walls), it is more convenient to use the Dipole-dipole configuration. Note that, sensitivities may be positive or negative, this is due to fact that an increase in observed apparent resistivity may be due to increases in resistivity in part of the region or decreases in other parts. Roy and Apparao (1971) provide a depth of investigation for various four-electrode arrays. Their analysis suggests that suitable depths for Wenner and Dipole–dipole arrays are respectively 0.11L and 0.18L, where L is the longest distance between electrodes. It should be noted that these depths are based on assumption of uniform resistivity, which is "impossible" to find in natural subsoils. The signal strength is also an important consideration when selecting measurement arrays: Dipole–dipole configuration can result in weak voltage gradients at the receiver, particularly for large separation between transmitter pair and receiver pair, while for closely spaced dipoles, high voltage input can result in "over voltages" (saturation of the receiver). In contrast, the Wenner array provide relatively stable and stronger signals due to the location of the receiver pair within the current electrode pair (Binley, 2015). Regardless of the array, large geometric factors may produce small voltage differences, which are prone to error. In other words, the conversion of measured voltages to apparent resistivity is subject to larger error. A critical cut-off is determined based on the expected electrical conductivity of the subsoil and the instrument specifications. Figure 2.5 (Lewis & Johnson) highlights, holding a constant intensity of electric current i=50 mA and assuming an instrument error of 1 μV, the measurement error of the voltage, translated into error in calculated apparent resistivity, as a function of K, for three different values of resistivity: 50, 500, and 5000 Ω*m.

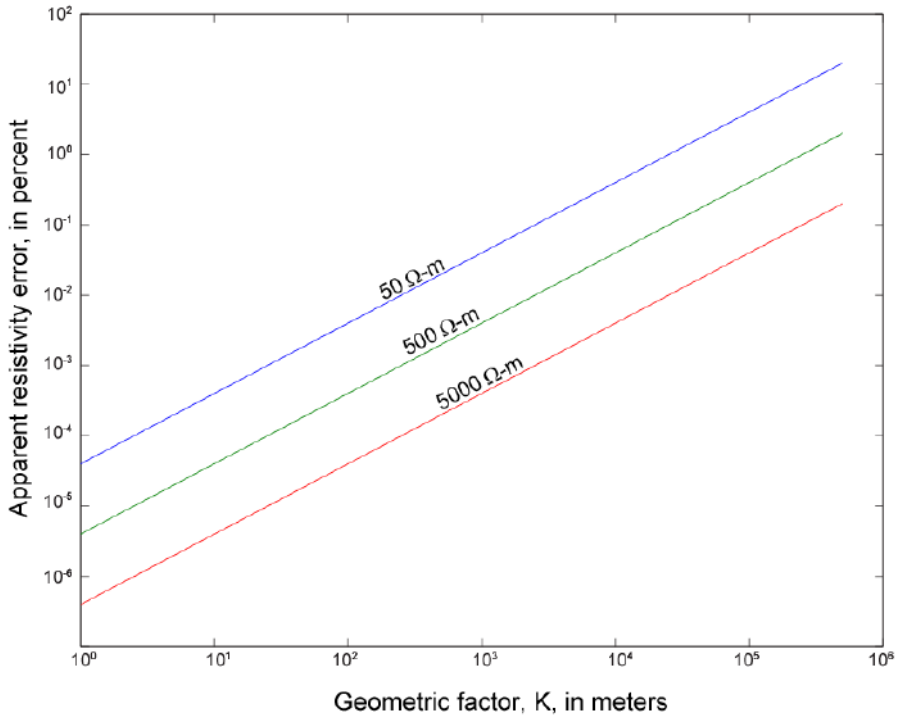

*Figure 2.10 Apparent resistivity error (%) as a function of K, for three different homogeneous medium: 50, 500 and 5000 Ω*m*

If the measurements are taken moving laterally the electrode quadrapole, it is possible to create a resistivity profile at constant depth. If we consider a subsoil with lateral variation of the resistivity, as shown in Figure 2.11.a, the apparent resistivities calculated, by taking measurement moving the electrode quadrapole laterally (with a dipole-dipole configuration), are represented in Figure 2.11.b:

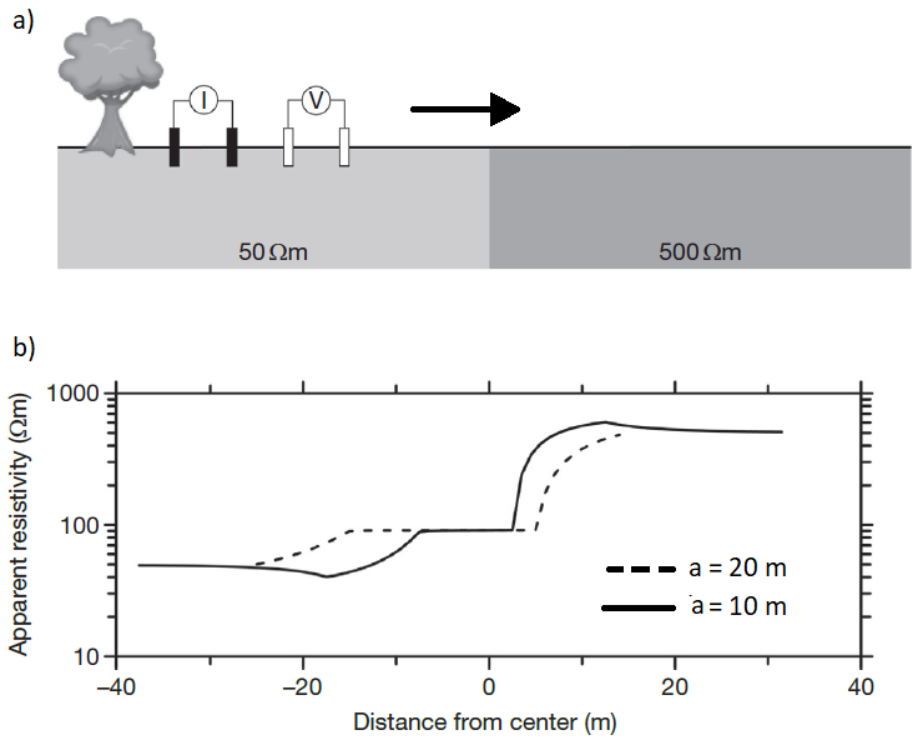

Figure 2.11 Lateral profile of apparent resistivity. The solid line indicates the measured apparent resistivity for a 10 m-spaced dipole and the dashed line shows the equivalent for a 20 m-spaced dipole

Note that, when the measurements are taken in the far left and right regions of the survey, the apparent resistivity is equal to the real one because the medium under investigation is homogeneous. Instead, close to the divide, a variation in apparent resistivity is observed as the measurement samples both the units with different resistivities. As expected, in comparison with the 10 m spaced configuration, the 20 m spaced array shows a greater influence of the contrast in resistivity further away from the divide.

If we increase the distance between the electrodes with each measurement, keeping the center of the electrode quadrapole unchanged, a vertical electrical sounding (VES) is obtained. As previously defined, the measurement error increases with the increasing of the electrodes spacing and therefore with the depth of investigation. The Schlumberger array (see Figure 2.12.a) is commonly used for VES surveys. In the Schlumberger configuration, the current electrodes A-B are outside the potential electrodes M-N, as in Wenner array, but the distance between the electrodes M-N is much smaller than that between the current electrodes (distance MN < 0.2AB). This kind of configuration has intermediate characteristics (penetration, signal strength, lateral and vertical sensitivity) in comparison with the Wenner and Dipole-dipole arrays. For a Schlumberger array VES, the spacing AB is normally increased in a logarithmic sequence, keeping the potential electrode dipole M-N fixed. The results are presented as a plot of the logarithm of apparent resistivity versus the logarithm of AB/2, as shown in Figure 2.12.b. Using data modeling tools (described in chapter 2.5), these data

are analysed in order to obtain 1D resistivity structure, a sequence of layers with relative thicknesses and resistivity. An example of a VES investigation is shown in the Figure 2.12 below, where a 10 m thick low-resistivity (50 Ω*m) unit overlies a more resistive unit (500 Ω*m).

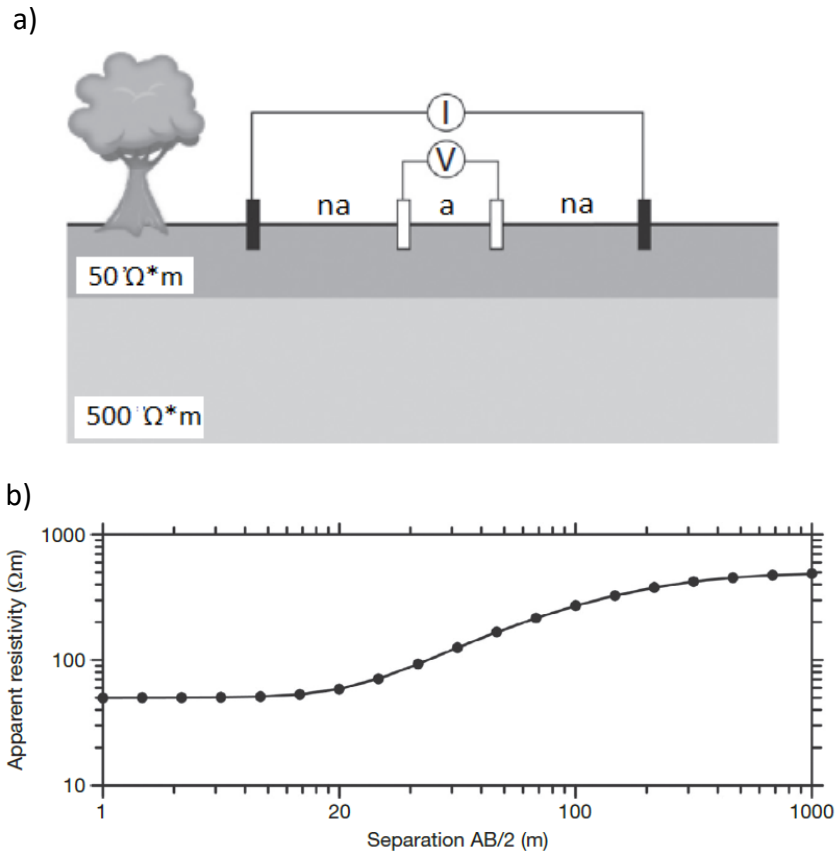

Figure 2.12 (a) Schematic example of VES survey in the field and (b) the result

Note that, shorter array spacing measurements of apparent resistivity are not influenced by the deeper resistivity unit. As the array gets larger, the effect of the near-surface layer is reduced but the upper layer still has an impact on the apparent resistivity measured, even at very large electrode separations. If we check Figure 2.6, which highlights the same subsoil structure but with the flow lines represented, we can appreciate how, as expected, for longer electrode spacing the current paths penetrate deeper but the near-surface low-resistivity unit has still an effect of reducing the depth of current flow. Therefore, as previously discussed, the depth of the investigation is influenced not only by the geometry of the electrode array and the type of array (Wenner, Schlumberger, Dipole-dipole) but also by the resistivity structure of the subsoil under investigation.

If VES and lateral reistivity measurements are made both along the same profile, then we are able to develop a 2D vertical section of resistivity. This kind of investigation is defined as ELECTRICAL RESISTIVITY TOMOGRAPHY (ERT). Such surveys can be realized with only four electrodes, although the process will be extremely labor-intensive. Nowadays, 2D imaging surveys are routinely performed with multielectrode configurable instruments. Modern multielectrode instruments permit connection to an array of even more than one hundred electrodes, connected to the instrument through a multicore cable. To better understand the concept of the ERT surveys it is useful to check Figure 2.13, wich shows an example of ERT acquisition scheme with a Dipole-dipole configuration.

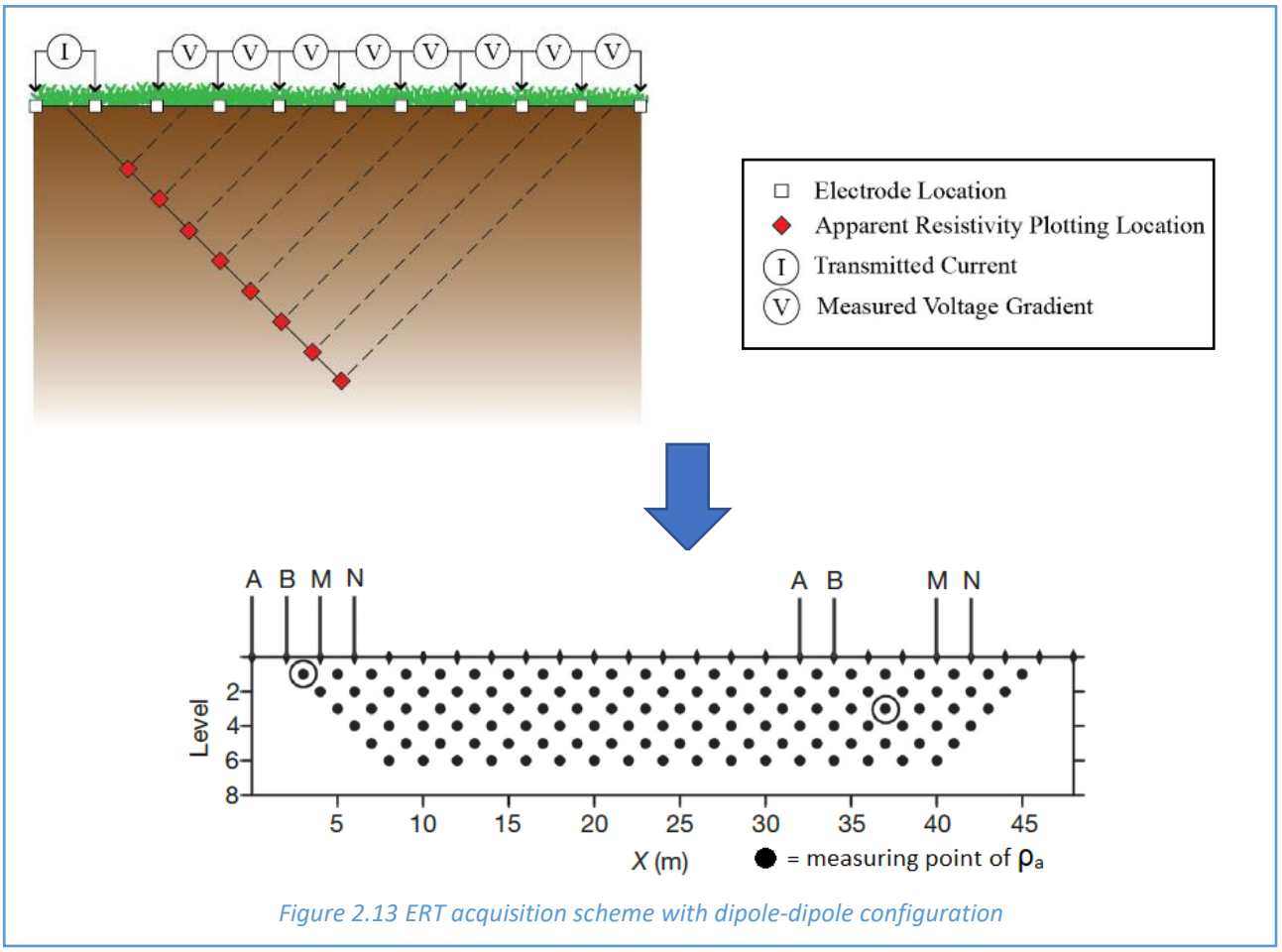

Figure 2.13 ERT acquisition scheme with dipole-dipole configuration

Data from 2D imaging surveys are normally presented as a pseudosection of apparent resistivity. It is important to note that the pseudosection does not reveal the resistivity structure of the subsoil, the inversion process is always necessary, but it is simply a means of displaying data and observing any anomalies. Obviously, as you can see in Figure 2.14, measurements acquired on the same line with different kind of arrays will provide different pseudsections of apparent resistivity.

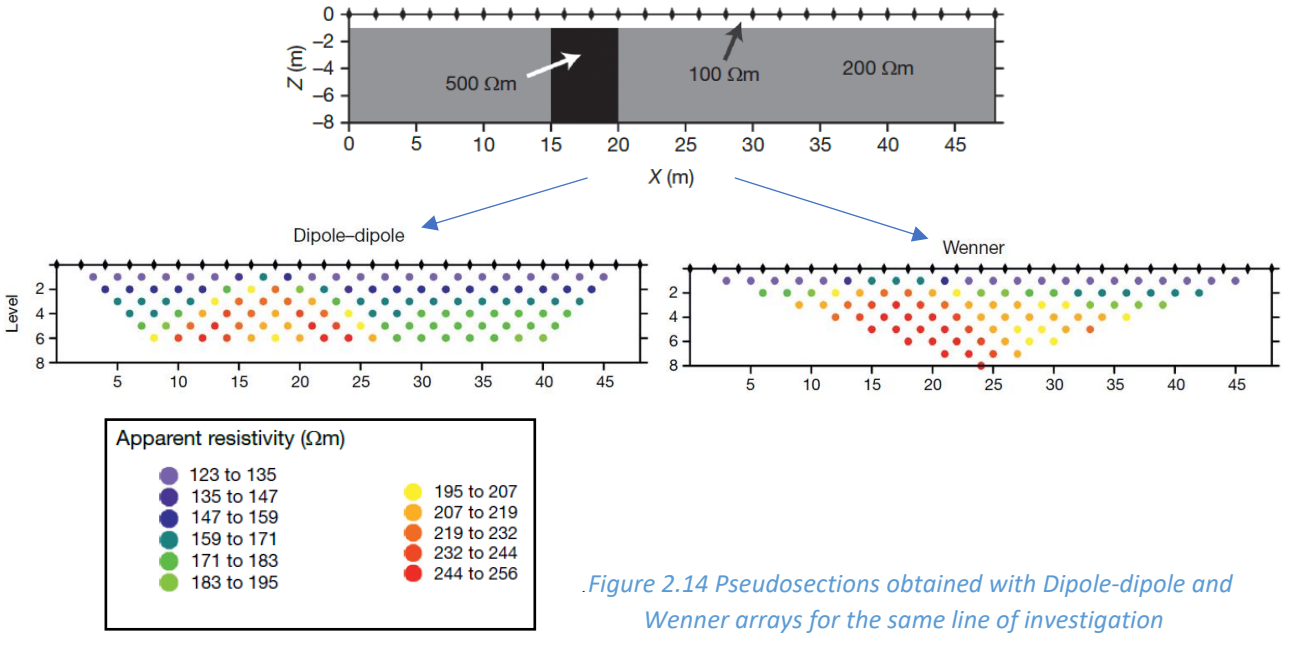

Figure 2.14 Pseudosections obtained with Dipole-dipole and Wenner arrays for the same line of investigation

As already discussed, the choice of quadrapole configuration will depend mainly on the target of the investigation. For instance, if the goal of the survey is to delineate lateral variability, then a Dipole–dipole configuration may be suitable. Instead, if the target is to delineate vertical variability, then a Wenner configuration is advisable. Since the acquisition time for a line last on average a few tens of minutes, depending on the number of measurements and also on the type of instrument being used, it would be preferable to take measurements with both the configurations and use both the inverted sections to better understand the real structure of the subsoil. Furthermore, in Figure 2.14 we can see that, in pseudosections, the ordinate axis is not expressed in meters but simply as levels. Also the conversion from levels to depth will be obtained during the inversiom process phase. Eventually, the depth of each measurement can be estimated by the analysis of Roy and Apparao (1971), already described in this chapter. The maximum investigation depth, obtained at the center of the line, can be estimated with a rule of thumb: z_{max} = 1/5 L, where L is the length of the acquisition line. Since the number of electrodes that the instruments can control is limited, the length L of the line will also be limited according to the number of electrodes available. To increase L, it is possible to enhance the spacing between the electrodes but, as we will see soon, the resolution of the investigation will also decrease. In some situations it may be also necessary to extend laterally the maximum investigation depth. To achieve this, it is possible to use the roll-along method: the electrode line is moved laterally and new measurements are taken. Figure 2.15 can be used to better understand this last procedure:

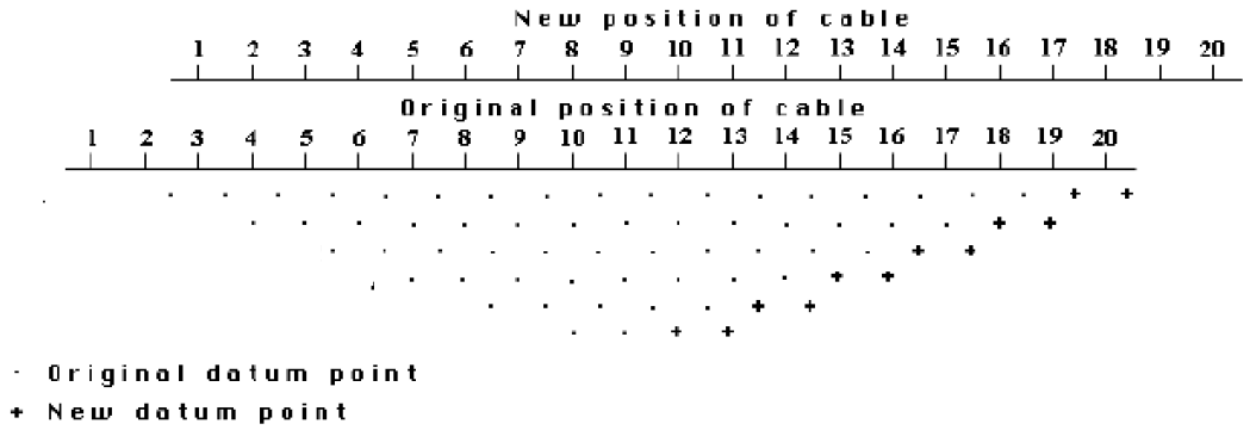

Figure 2.15 Scheme of the roll along method to extend laterally the survey area

It should be emphasized that, as we will see in the main investigation of the thesis in chapter 3, the depth of the investigation can be limited by the subsoil structure. Very conductive surface layers can lead to a short-circuit of the system and prevent reliable measurements at a greater depth. Despite all this, as already discussed, the resolution of the investigation depends mainly on the distance between one electrode and the next one, lower is the spacing and higher is the resolution. We can use the rule of tumb of the Figure 2.15 to define the resolution of the investigation:

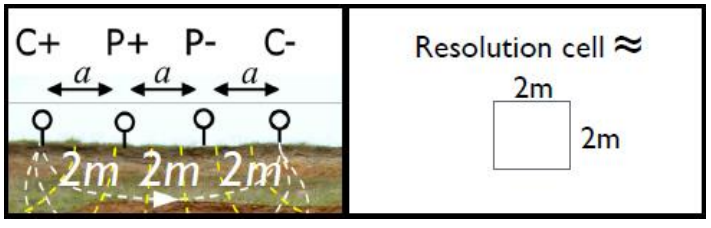

Figure 2.16 Connection between resolution and spacing

However, it must be taken in account that this rule is valid mainly in superficial levels. As previously seen, when the geometric factor increases, and so the depth of the survey, the measurement error increases and therefore the resolution inevitably decreases. Note that, as for the choice of the geometry of the quadripole, the length L of the line and the spacing of the electrodes also depends on the target of the investigation. With non-invasive investigations from the surface we need to choose whether to perform deep but not very resolutive survey or very resolute but not particularly deep investigations. For instance, very long lines can be used to find the depth of the rock substrate in seismic micro-zonation investigations whereas, lines with spacing in the order of centimeters (defined as micro-electrical tomography), can be used to study the interactions between roots and soil at small scales. Nevertheless, to increase the resolution in the deeper levels or to overcome any short-circuit problems related to conductive surface layers, borehole surveys can be used.

Nowadays, multielectrode instruments coupled with the recent computational developments, allow us to achieve surface electrode array configurations for 3D imaging. Given the required number of quadrupole configurations, the number of electrodes available and data collection time can be significant constraints. Therefore, such surveys are often limited to relatively small-scale investigations, as MICRO-ERT. For larger scale investigations, where the required depth is higher, quasi 3D imaging is easily achievable by the use of multiple 2D imaging transects (Cassiani et al., 2006; Dahlin and Loke, 1997). Measurements can be made along a series of parallel lines and, once the data of each row have been processed, we can create a pseudo-3D image with three-dimensional interpolators. Figure 2.17 shows a schematic example of ERT 3D acquisition:

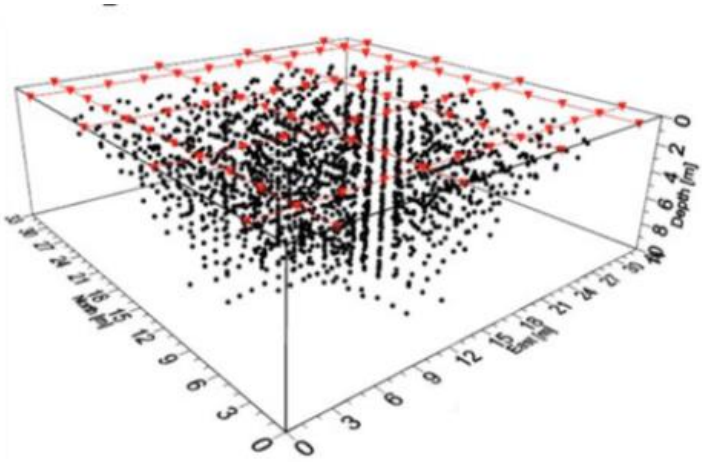

Figure 2.17 Example of ERT 3D acquisition

2.2.2 Borehole-Based Imaging

As previously added, to increase resolution to greater depths or to overcome the problem of very conductive surface layers that could short-circuit the system, measurements can be made by means of boreholes. The optimal contact between the electrodes and the ground must be guaranteed. This can be accomplished, for example, by using stainless steel ring electrodes mounted on the outside of a PVC tube that is lowered down the well by percussion and held in firm contact with the borehole wall (Cassiani et al., 2015). Alternatively, the borehole can be backfilled with mud or moist sand after the electrode string is deployed. However, the boreholes used for ERT investigations are usually partially filled with water, either naturally if below the water table or artificially if measurements are made in the unsaturated zone (to provide the contact between electrodes and

rock), therefore is necessary to use watertight cables. In the saturated zone, open (uncased) boreholes can also be used with particular arrays of electrodes that have been manufactured for this purpose, some with isolation packers to minimize current flow along the borehole water column. Studies have demonstrated the possible effect of short-circuiting of current up/down the water column and the impact of such effects on resultant images (serious artifacts), particularly for large resistivity contrasts between the rock formation and borehole fluid or for large borehole diameters. Despite this, the borehole effect is rarely considered in ERT investigations even if the effect of channeling can be accounted in any data modeling by incorporating measurements of borehole water electrical conductivity and borehole geometry (e.g. Doetsch et al., 2010; Nimmer et al., 2008; Osiensky et al., 2004). Nevertheless, being the electrodes inserted into the ground, the equipotential surfaces are no longer those of hemispheres but become those of spheres concentric to the energizing electrode and the equation 2.4 must be rewritten as: $V = \frac{i*\rho}{4\pi r}$. Therefore, if the current source electrode A is placed at depth $z_A > 0$ and the voltage is measured with electrode M, directly above or below A, we find that:

$$(2.12)\quad V(M,A) = \frac{i*\rho}{4\pi}\left[\frac{1}{|z_A - z_M|} + \frac{1}{z_A + z_M}\right]$$

The same procedure is applied for V (B, M) V (A, N) and V (B, N), consequently the geometric factor K of the equation 2.8 becomes:

$$(2.13)\quad K = 4\pi\left[\left(\frac{1}{|z_A - z_M|} + \frac{1}{z_A + z_M}\right) - \left(\frac{1}{|z_B - z_M|} + \frac{1}{z_B + z_M}\right) - \left(\frac{1}{|z_A - z_N|} + \frac{1}{z_A + z_N}\right) + \left(\frac{1}{|z_B - z_N|} + \frac{1}{z_B + z_N}\right)\right]^{-1}$$

and finally, equation 2.9 can be applied to determine the apparent resistivity. As we can see in Figure 2.18, electrodes in boreholes may be utilized in different ways, using a single borehole or two:

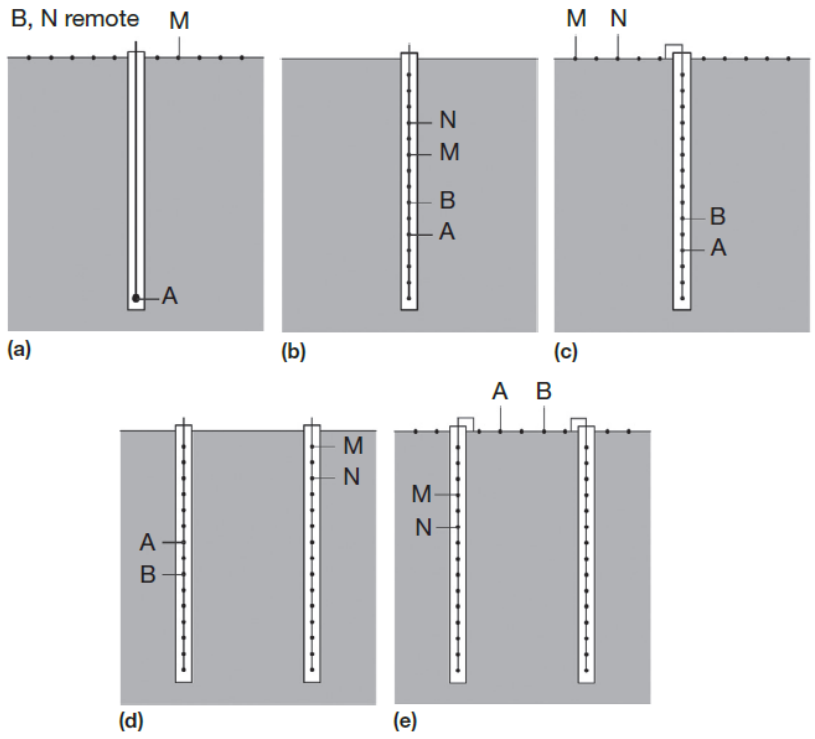

Figure 2.18 Scheme of possible uses of boreholes for electrical imaging: (a) the mise-à-la -masse, (b) single borehole, (c) borehole-to-surface, (d) cross borehole, and (e) cross borehole with surface electrodes

The mise-à-la-masse (Figure 2.18.a) is a common borehole-based approach used in mineral exploration. In such a survey, one of the current-carrying electrodes is installed in a borehole at depth, while the other current electrode is installed on the surface at a significant distance from the borehole. Potential measurements are then made at several sites on the surface, relative to a remote potential electrode. The measurements may be compared to modeled voltages for a homogenous resistivity. In mineral exploration, such measurements can help to delineate electrically conductive ore bodies. However, single-borehole electrode arrays supplemented with surface electrodes (Figure 2.18.a/c) may present the problem of poor signal-to-noise, especially with deep electrode placement and short dipole spacing. Nevertheless, borehole-to-surface surveys could be advantageous when used with varying surface azimuthal arrays (measurements are taken with different orientations of the surface electrodes line) in order to assess anisotropy in fractured environments or in hydrological studies to identify the migration of an electrically conductive tracer injected in the well (e.g. Osiensky, 1997). Instead, using measurements from electrodes placed in two boreholes (Figure 2.18.d), sometimes supplemented by surface electrodes (Figure 2.18.e), provide an image of the resistivity between the boreholes. Using borehole-deployed electrodes, a very large number of measurement schemes are possible. In Figure 5.10, two examples of bipole-bipole schemes are shown (we use the term bipole-bipole to differentiate from the conventional surface dipole-dipole array). In the AM-BN scheme shown in Figure 2.19.a, current is injected between the two boreholes and a potential difference is measured between the boreholes. In the AB-MN scheme of Figure 2.19.b, current is injected between electrodes in the same borehole, and the potential difference is measured between electrodes in the other borehole. The AM-BN scheme has good signal-to-noise characteristics, in comparison to AB-MN, because of the dipole length. Regardless of the dipole configuration, the sensitivity pattern of the measurements will depend on the spacing of the boreholes, ideally the spacing between boreholes should be less than half the shortest length of an electrode array in any of the boreholes. High sensitivity will exist close to the boreholes and will be low mid-way between the boreholes (Binley & Kemna, 2005).

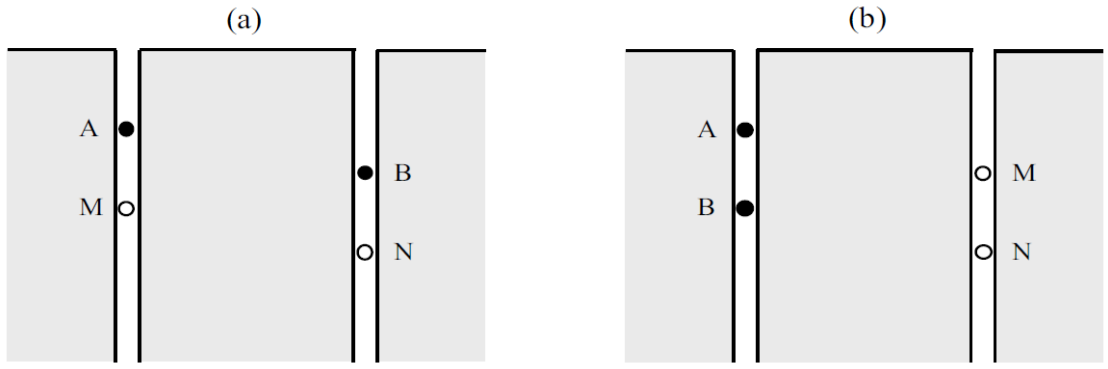

Figure 2.19 Example of bipole-bipole measurement configuration for cross-borehole resistivity imaging; (a) is AM-BN scheme and (b) is AB-MN scheme

The main advantages of cross-borehole imaging compared to surface imaging are that: high resolution at depth is possible and investigations can be made without the need for surface access (for example, surveys under buildings are possible). The disadvantages are that: boreholes are required (this implies higher economic and time budget); data sensitivity is constrained to the region between the boreholes; data acquisition may require more sophisticated instrumentation (for example watertight cables and not conventional electrodes); noise levels may be much higher than

those using surface electrodes, due to a weaker electrical contact (contact resistance problem); and data processing is more complex (Binley & Kemna, 2005). Regardless of its disadvantages, cross-borehole surveys are applied to a wide range of hydrogeophysical problems, including vadose zone studies (e.g. Binley et al., 2002; French et al., 2002), characterizing the transport of tracers in the subsurface (e.g. Slater et al., 2000; Kemna et al., 2002), monitoring remediation technologies (e.g. Ramirez et al., 1993; Schima et al., 1996) and monitoring leakage from underground storage tanks (e.g. Ramirez et al., 1996). Furthermore, borehole-based imaging concepts have also been adopted for mine/tunnel investigations. For instance, Van Schoor and Binley (2010) showed how tunnel-to tunnel imaging can be used to detect potholes in a South African platinum mine.

2.2.3 Time Lapse Based Imaging

All the geoelectric techniques covered till now can be used to monitoring time-dependent subsurface processes, through changes in resistivity over time. In simple words, the same electrodes line is measured several times with the same configuration. This kind of investigation are defined as ERT time-lapse and are typically carried out with controlled irrigation experiments. In fact, particularly interesting are, in this context, the time-lapse resistivity changes that can be linked, primarily, to changes in soil moisture content. In order to enhance the changes from one-time frame to the next, a ratio inversion approach is advisable to use. For each quadripole the data to be inverted at each time step are constructed from the ratio of resistances of that same quadripole in the current time step ($R_{t)}$ and in the reference initial time step (R_0):

$$R_{ratio} = \frac{R_t}{R_0} \times 100\ \% \qquad (2.14.a)$$

Ratio inversion is a powerful approach to highlight subtle time-lapse variations of electrical conductivity that would be otherwise overwhelmed by error differences in subsequent absolute resistivity images (Daily et al., 1992). The results are consequently given in terms of resistivity ratios with respect to the initial reference state. Therefore, after the inversion process, only the results of the first measurement will be plotted in terms of absolute resistivity, the sections obtained from the subsequent measurements will be plotted in terms of percentage variations of resistivity with respect to the first measurement. Furthermore, in order to relate the variations in resistivity of the medium with the changes in water saturation, Archie's law (1942) can be used:

$$\sigma_b = a*\sigma_w*\phi^m*S_w^n \qquad (2.14.b)$$

Where σ_b = subsoil conducibility, σ_w = pore water conducibility, ϕ = porosity, S_w = water saturation, a ≈ 0.5-1.5 (depending on tortuosity, grain size, clay content, etc), n≈2 and m ≈ 1.2-2.3 (cementation factor); these values can be calibrated preferably with laboratory tests or characteristic literature values can be used according to the investigated subsoil. The use of Archie's law is particularly beneficial given its functional form that allows computing saturation ratios directly from resistivity ratios. However, soil resistivity depends on soil moisture as much as on pore water resistivity. A mixture of the two dependencies has been clearly observed on the field in many studies (e.g. Winship et al., 2006; Cassiani et al., 2006; Ursino et al., 2014), particularly when abundant fresh water is poured in a system where pore-old water has had the time to equilibrate its salinity with the existing soil mineralogy. In this situation resistivity variation can also be explained by piston flow, the irrigated fresh water pushes deeper the old pore water.

2.3 Collection and Verification of Field Data

Modern multielectrode instruments require input files listing which quadripoles to collect. It is highly advisable to collect repeat measurements with the same quadripole and to take reciprocal measurements, which together allow to determine the quality of the data (variance and standard deviation). This information is necessary during the inversion process, to define a satisfactory misfit between the model prediction and the measured data. In fact, over-fitting in data inversion leads to "noisy" images and artifacts.

However, before starting the measurement, several control procedures are required. At first, is necessary to check that all the electrodes of the array are correctly connected to the instrument and the contact resistances between the electrodes and the ground are not too high. Negative apparent resistivity often highlight problems with contact resistance, although most modern instruments provide estimates of contact resistance prior to a survey and reduction of the contact resistance is relatively easy to achieve in ground surface surveys by the addition of small quantities of saline fluid around the electrodes. Generally, contact resistance cut-offs of 50 kΩ for borehole data and 20 kΩ for surface data are used. It is also important to take in account the receiver voltage levels for a given measurement: high geometric factors, combined with low input voltage, can lead to voltages that are close to instrument resolution. Measurements below 0.1 mV are generally discarded. Natural self-potentials also need to be accounted, particularly if they are not stable over time. Although most modern instruments incorporate appropriate filters to reduce such effects (Binley, 2015). As already specified in chapter 2.2, to avoid polarization of the electrodes, an alternating power source must be utilized. A switched square wave, as shown in Figure 2.4, is the most common current waveform and it is generally applied at frequencies of about 0.5 to 5 Hz. Pulse duration varies from 250 ms to several seconds, obviously lower pulse duration results in shorter data acquisition time. Pulses on the order of 250 ms may be acceptable in conductive, low-clay media; in the presence of clays and induced polarization, however, longer durations may be required to achieve equilibrium voltages. The length of the pulse duration can be varied, and surveys repeated, to determine the minimum duration necessary to achieve good data (Lewis & Johnson). Finally, it is important to remember that, before or after the measurements, the position of all the electrodes must be recorded (for example via GPS), especially if the topography is irregular. In fact, the position of each electrode is an important input parameter in all the inversion codes.

The quality of DC resistivity measurements can be defined through a couple of processes: stacking and reciprocal measurements. The former requires that the same quadripole should be measured several times, the results are finally averaged: $\rho_a = \sum_1^n \rho(n)$. For some multielectrode instruments it is possible to choose the number of stacks for each quadripole (e.g. MAE X612EM +), instead other instruments (e.g. Syscal Pro) require a percentage difference threshold (e.g. 5%) between two consecutive measures and, once this threshold is reached, the stacking will be stopped. Although collection of repeat measurements increases duration of the surveys, this extra time is well worthwhile. Stacking is used to improve the signal-to-noise ratio because random noise is averaged out. In addition, the standard deviation of the repeat measurements provides a means to quantify error and define data weights for inversion. An alternative measure of data quality is reciprocity (Parasnis, 1988). A reciprocal measurement involves swapping current and voltage electrode pairs. In other words, electrodes A-B are swapped with electrodes M-N such that K remains the same. Theoretically, the reciprocal measurement should yield the same apparent resistivity as the original

measurement. However, this doesn't happen and the standard deviation of reciprocal measurements is termed "reciprocal error," which provides a measure of instrument error. In general, reciprocal errors are larger than stacking errors, and it is commonly thought that reciprocal measurements provide a better assessment of data quality in DC surveys (Slater & Binley, 2006; Slater et al., 2000). Collection of reciprocal measurements tends to be even slower relative to collection of stacked measurements. In fact, reciprocal measurement double the duration of the survey as the switch between electrodes can take on the order of a second for modern systems, whereas a repeat measurement requires no switching and takes on the order of 50 to 500 ms depending on the pulse duration. However, reciprocal measurements should not be collected immediately after their associated measurements, as polarization of the electrodes may affect the resultant measurement. Such effects generally dissipate in a few seconds (Lewis & Johnson).

The results of the stacking process are automatically provided by the multielectrode instruments. In fact, the measurement shown for each quadripole in the output file, as you can see in Figure 2.20, is the average apparent resistivity obtained by applying the stacking process.

A	B	M	N	r (O*m)	var	M (ms)	PS (mV)	V (mV)	I (mA)
1	6	2	7	95.12	0.06	0	-54.6	1223.95	51.06
1	6	7	12	107.52	0.11	0	13.88	-661.98	51.06
1	6	12	17	90.99	3.65	0	-6.16	-35.01	51.06
1	6	17	22	132.99	0.62	0	-15.07	-14.62	51.06
1	6	22	27	164.2	0.56	0	-6.92	-7.64	51.06
1	6	27	32	171.17	5.56	0	33.54	-4.11	51.06
1	6	32	37	184.15	0.57	0	3.16	-2.58	51.06
1	6	37	42	175.62	11.21	0	-18.03	-1.56	51.06
1	6	42	47	109.62	13	0	-108.03	-0.66	51.06
1	6	47	4	86.06	1.18	0	134.71	114.72	51.06
1	6	3	8	79.6	0.11	0	-72.83	338.88	51.06
1	6	8	13	79.26	0.09	0	7.23	-191.71	51.06
1	6	13	18	98.01	5.02	0	-2.69	-27.89	51.06
1	6	18	23	138.48	0.84	0	12.57	-12.54	51.06
1	6	23	28	168.14	0.52	0	9.14	-6.77	51.06
1	6	28	33	178.22	4.41	0	97.31	-3.81	51.06
1	6	33	38	174.61	6.65	0	-80.62	-2.22	51.06
1	6	38	43	172.48	10.18	0	-21.83	-1.41	51.06
1	6	43	48	86.77	18.83	0	-99.48	-0.48	51.06
1	6	48	5	106.96	0.28	0	139.72	649.74	51.06
1	6	4	9	86.73	1.84	0	-43.25	29.37	51.06
1	6	9	14	74.7	0.1	0	-1.46	-97.29	51.06
1	6	14	19	105.3	6.65	0	10.54	-22.86	51.06

Figure 2.20 Example of an output file (incomplete) provided by multielectrode instruments

In Figure 2.20 we can see a typical output file (not complete because the measurements are generally several hundreds or even thousands) provided by a multielectrode instrument. The first four columns indicate the electrodes used for the measurement, the fifth column is the average apparent resistivity, the sixth column is the variance of the quadripole (as we seen, each quadripole is measured several times so we can define variance and thus the standard deviation), the seventh column is the Chargeability (it does not concern DC resistivity surveys), the last three columns are respectively the natural self-potentials, the potential difference and the intensity of the current.

Instead, the reciprocal measurements need to be checked by appropriate codes, as Iris2profiler (Cassiani). In these codes we must define the acceptable difference threshold between the reciprocal measurements (e.g. 5%) and provide an input file correctly ordered, for instance

Iris2profiler accepts files like the one in Figure 2.20. After the running, the codes will provide a new file that will not contain the quadripoles with differences in reciprocal measurements greater than the indicated threshold. This file will be used for the inversion process. Note that, the acceptable threshold depends on the quality of the acquired data. In environments with high contact resistances, for example permafrost or unsaturated gravel, the quality of the data is typically low and applying a threshold too low could lead to lose almost all the measured dataset. In this situation it is necessary to consider a higher error threshold (e.g. 10%).

To demonstrate the importance of the stacking procedure, a real example is shown. Taking advantage with an archaeological investigation in Padua, aimed to determinate the location of the foundations of the ancient Roman theater in Piazza Prato della Valle (Pavoni, 2018), a comparison of the dataset quality has been performed, measuring the same line, with the same instrument (MAE X612EM +), using at first 3 stacks and then 6 stacks. In Figure 2.21 is possible to appreciate the place (a) and the line of investigation (b):

2.21 (a) Prato della Valle (Padua, Italiy) and (b) the investigation line

The control of reciprocal measurements has been applied to both the datasets, with a threshold of 5%. As we can see in Figure 2.22, the number of saved quadripoles, after checking the reciprocals measurements with Iris2profiler (Cassiani), is much greater with a stack of 6. Thus, increasing the number of stacks increases the confidence of the investigation as the number of data considered during the inversion process will be greater as the knowledge of the noise level.

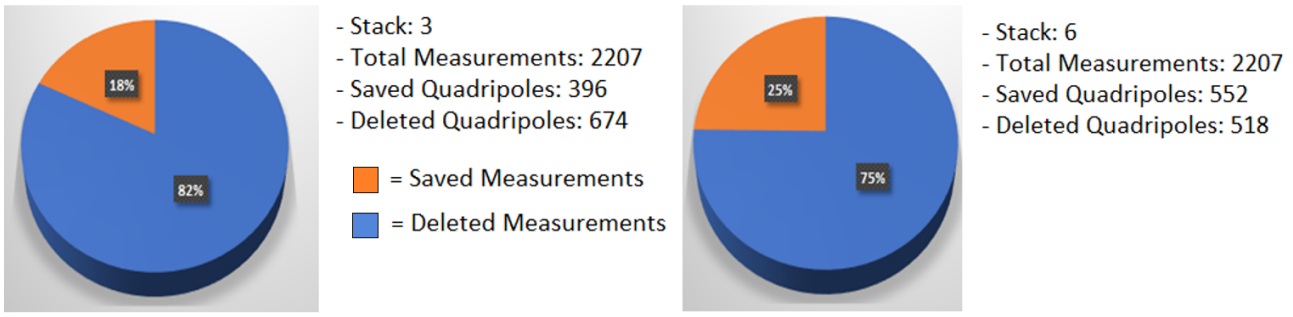

Figure 2.22 Comparison between final data obtained with different numbers of stack on the same line of investigation

The importance of reciprocal measurements and their check will be demonstrated in chapter 2.5.

2.4 Multielectrode Instrument

Nowadays, geoelectric surveys are developed through multielectrode instruments. The main components of a multielectrode instrument are:

- a computerized control unit that manages the activation of electrodes;
- a series of batteries (internal and/or external) that power the instrument and with which a potential difference ΔV is applied to the electrodes A-B;
- an ammeter that measures the intensity i of the electric current at the electrodes A-B;
- a voltmeter that measures the potential difference ΔV that arise between electrodes M-N.

Obviously, to realize a surface survey, other accessories are required:

- electrodes, multicore cables and connector cables for the electrodes;
- tape measure, to check the distance between electrodes, and hammer to plant them;
- to correctly know the position (x, y, z) of electrodes it is advisable to use differential GPS, specially, if the topography is irregular.

Figure 2.23 shows an example of multielectrode instrument and other components necessary to realize a surface survey, the most common one. The multielectrode instrument shown in figure is the MAE X612EM +, owned by the Department of Geosciences of the University of Padua (Italy).

Figure 2.23 MAE X612EM+ and other components needed to realize a surface survey

Currently on market there are several multielectrode instruments, each of which has particular technical features that define its price. If we consider the MAE X612EM+, its main feature is the very high speed of carrying out the surveys. It can simultaneously perform the potential measurements between any two of the connected electrodes, except the torque A-B used for the current input. In simple words, in a configuration with N electrodes, the instrument has N-2 acquisition channels. Up to 96 electrodes can be connected to the instrument simultaneously and the stack number can be set. The instrument is also equipped with an integrated computer, which allows to see, in real time, the recorded data and the pseudosection. Finally, important feature that is worth to be mention, is the ability to set time intervals for which the instrument automatically measures the line, useful for time-lapse investigations. Another multielectrode instrument is the Syscal Pro, also owned by the Department of Geosciences of the University of Padua and shown in Figure 2.24.a during the survey in Piazza Prato della Valle – Padova, Italy (Pavoni, 2018).

Figure 2.24.a The Syscal Pro multielectrode instrument

The instrument is characterized by ten measuring channels so the investigation time is much longer than those carried out with the MAE X612EM+. Furthermore, the Syscal Pro doesn't have an integrated computer but is necessary to connect it with an external laptop in order to be able to see the recorded data and the pseudosection in real time. However, the instrument allows to connect 120 electrodes simultaneously and, as regards the stacking process, before starting the measurements, it is necessary to define a percentage threshold of difference between two successive measurements of the same quadripole (e.g. 5%). During the investigation the Syscal Pro performs at least three measurements on the same quadripole and stops only when the indicated threshold is reached. Finally, the most important feature of the Syscal Pro is the much better electronics than the MAE X612EM+, which guarantees a higher quality of measurements. The last feature is particularly important and is what determines a much higher purchase price for the Syscal Pro. To underline the importance of the electronics, another real example is reported. In the same Prato della Valle survey of Chapter 2.3 (Figure 2.21), the same line was also measured with the Syscal Pro. The dataset obtained with the Syscal Pro has been checked also with the code Iris2profiler (Cassiani), always considering an error threshold of 5%. As shown in Figure 2.24.b, if we compare this result with the best obtained with the MAE X612EM+, stack 6), the saved quadripoles have almost doubled. Thus, the Syscal Pro presents a much greater confidence in the measurements due to a decidedly more advanced voltmeter, which could justify a price three times higher, despite the handicap of having significantly higher acquisition times and the impossibility to have a real-time preview of the pseudosection on a monitor without an external laptop.

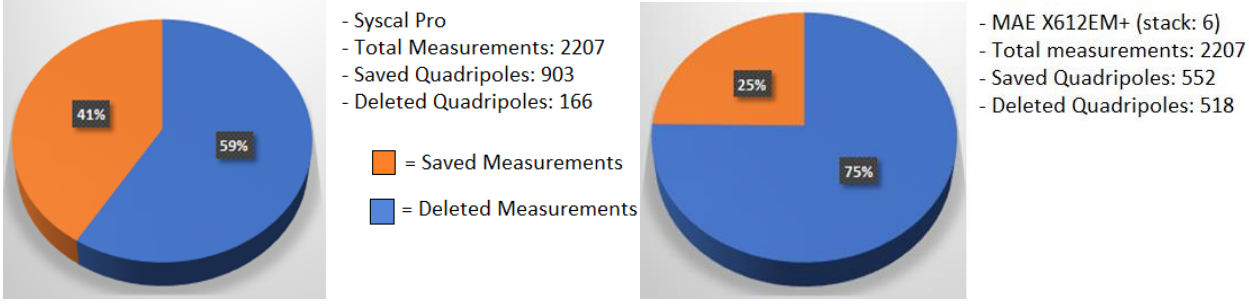

Figure 2.24.b Comparison between final data obtained with MAE X612EM+ (stack 6) and Syscal Pro

It should be noted that, these multi-electrode instruments, not only these two just described, can also be used for borehole surveys or investigations over water (e.g. lakes). However, in these cases waterproof cables and special electrode arrays are required. Finally, it is important to underline the robustness of these multi-electrode instruments which can work in extreme environmental conditions, from -20 °C to 80 °C.

2.5 Modeling and data inversion

As introduced in the earlier chapters, measured apparent resistivity values do not provide directly a model of the subsoil geoelectrical properties. To reach real resistivity models is necessary to use appropriate inverse modeling tools. A variety of public domain and commercially available inversion codes are in use within the geophysical community.

The inversion process is possible only if we know the physics that rules the phenomenon under consideration, the propagation of the current lines. Given a subsoil model, with certain layer thicknesses and relative values of resistivity, we must be able to calculate the apparent resistivity measurements that would be obtained by performing any of the investigations described in the previous chapters. This process defines the so called “forward problem” or “forward modeling”.

The flow of a direct current in a conducting medium is described in the form of a partial differential equation. The equation is obtained through two basic principles: the conservation of the electric charge and the validity of Ohm's law. If we consider a representative infinitesimal volume of a homogeneous and isotropic medium, called "representative elementary volume" or REV, shown in Figure 2.25, since we work with a direct current (steady state), there is no accumulation of charges nowhere, thus the incoming current flow is equal to the outgoing flow.

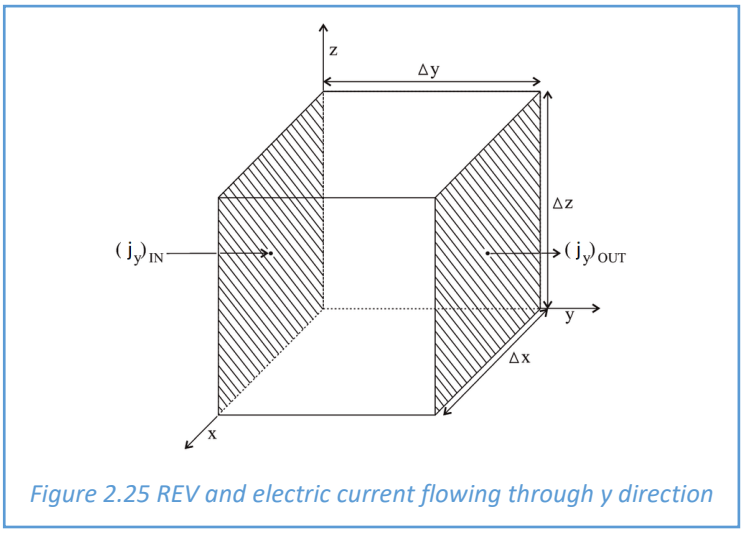

Figure 2.25 REV and electric current flowing through y direction

If we consider Figure 2.25, the current flow which enters in the REV along the y direction is:

$$j_y dxdy \quad (2.15)$$

while the output current flow is:

$$j_y dxdy + \frac{\partial}{\partial y}\left(j_y\right)dxdydz \quad (2.16)$$

The total flow along the y direction is the difference between equation 2.15 and 2.16:

$$(2.17) \quad -\frac{\partial}{\partial y}\left(j_y\right) dxdydz$$

The same procedure can be applied for x and z direction, thus the total current flow through the REV will be:

$$(2.18) \quad -\left[\frac{\partial}{\partial x}(j_x) + \frac{\partial}{\partial y}\left(j_y\right) + \frac{\partial}{\partial z}(j_z)\right] dxdydz$$

As we already discussed, in a steady state condition the incoming current flow is equal to the outgoing flow, so equation (2.18) is equal to zero:

$$(2.19) \quad \left[\frac{\partial}{\partial x}(j_x) + \frac{\partial}{\partial y}\left(j_y\right) + \frac{\partial}{\partial z}(j_z)\right] = \nabla \cdot j = 0$$

Therefore, the conservation of the charge implies that the divergence of the current flow is zero. Now, if we apply the third Ohm's law (equation 2.3) to equation 2.19, we will find the differential equation that describes the direct current flow in a non-homogeneous and anisotropic 3D medium:

$$(2.20) \quad \frac{\partial}{\partial x}(\sigma_x \frac{\partial V}{\partial x}) + \frac{\partial}{\partial y}(\sigma_y \frac{\partial V}{\partial y}) + \frac{\partial}{\partial z}(\sigma_z \frac{\partial V}{\partial z}) = 0$$

For an isotropic medium ($\sigma_x=\sigma_y=\sigma_z=\sigma$) equation 2.20 can be written as:

$$(2.21) \quad \frac{\partial}{\partial x}\left(\sigma \frac{\partial V}{\partial x}\right) + \frac{\partial}{\partial y}\left(\sigma \frac{\partial V}{\partial y}\right) + \frac{\partial}{\partial z}\left(\sigma \frac{\partial V}{\partial z}\right) = \nabla \cdot (\sigma \nabla V) = 0$$

and, if the medium is homogeneous and isotropic, we will find the Laplace equation:

$$(2.22) \quad \sigma\left[\frac{\partial^2 V}{\partial x^2} + \frac{\partial^2 V}{\partial y^2} + \frac{\partial^2 V}{\partial z^2}\right] = \nabla^2 V = 0$$

Now, if we consider an isotropic medium and an electrical current point source at the origin with strength i, the distribution of the electric potential is defined by the Poisson equation:

$$(2.23) \quad \frac{\partial}{\partial x}\left(\sigma \frac{\partial V}{\partial x}\right) + \frac{\partial}{\partial y}\left(\sigma \frac{\partial V}{\partial y}\right) + \frac{\partial}{\partial z}\left(\sigma \frac{\partial V}{\partial z}\right) = \nabla \cdot (\sigma \nabla V) = -i\delta(x)\delta(y)\delta(z)$$

Usually, these boundary conditions, at the ground surface and other infinite boundaries, are applied:

$$(2.24) \quad \sigma \frac{\partial V}{\partial n} + \beta V = 0 \qquad \text{where n is the outward normal}$$

where β defines the type of boundary condition: $\beta = 0$ entails no flux boundary (Neumann) and $\beta \neq 0$ implies mixed boundary with potential-dependent flow (Cauchy). Note that, at the ground surface a no flux boundary is always applied. Nevertheless, analytic solutions for the equations 2.23 are not typically available and numerical approximations of the solutions must be used. These are realized through grid-based methods, commonly finite difference or finite element. The use of finite difference or finite element allows us to transform partial differential equations, which are applied to every geometrical point of a continuum (infinite amount of points), into a system of finite amount of linear equations, formulated for a limited amount of grid points, which can be solved through numerical iteration techniques. Obviously, the system of equations can only be solved when the

number of linearly independent equations in the system is equal to the number of nodes (Gerya, 2010). The potential field (voltages for a given current injection) is computed only at node points, which are connected to each other to form a mesh of cells/elements. Smaller is the distance between the nodes and smaller is the difference between a hypothetical analytical solution and the numerical solution. Note that, as V is defined only at the nodes, each electrode must coincide with a node of the discretization grid. The logical steps to apply finite difference or finite element are:

- creating a numerical mesh, replacing an infinite amount of geometrical points of the continuum with a finite amount of grid points;
- defining physical properties to each cell/element of the grid (conductivity/resistivity);
- applying partial differential equations (including boundary condition) to the grid points and substituting them with linear equations expressed via finite difference or finite element;
- solving iteratively (e.g. Jacobi iteration or Gauss–Seidel iteration) the system of linear equations and obtaining unknown values of V for all the grid points.

In Figure 2.26 we can see a simple example of 2D numerical mesh:

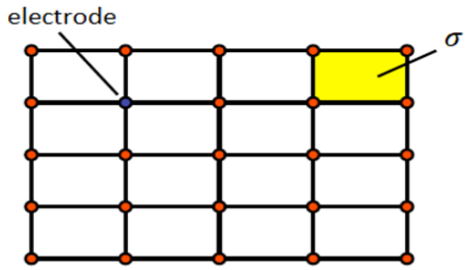

Figure 2.26 Example of 2D numerical mesh

Finite differences are linear mathematical expressions which are used to represent derivatives to a certain degree of accuracy. As we can see in equations 2.25 and 2.26 of Figure 2.27, the partial derivative (infinitesimal difference) is replaced with a measurable finite difference between the points (nodes) of the discretization grid (Anderson, 1992):

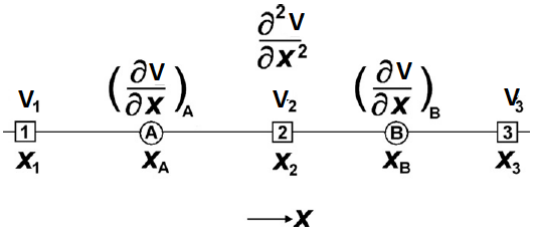

$$(2.25)\quad \left(\frac{\partial V}{\partial x}\right)_A \approx \frac{V_2 - V_1}{x_2 - x_1} \;;\; \left(\frac{\partial V}{\partial x}\right)_B \approx \frac{V_3 - V_2}{x_3 - x_2}$$

$$(2.26)\quad \frac{\partial^2 V}{\partial x^2} \approx \frac{\left(\frac{\partial V}{\partial x}\right)_B - \left(\frac{\partial V}{\partial x}\right)_A}{x_B - x_A}$$

Figure 2.27 Example of discretization with finite difference method along x direction

Smaller is the distance Δx between the points of the grid, the more accurate is the computed solution but also increase the amount of equations to solve and thus the cost of numerical solution. Obviously, in a 2D model the same procedure must be applied along the z direction and even y direction for a 3D model. For instance, considering a 2D model, the finite difference approximation for the Laplace equation 2.22 is shown in equation 2.27 of Figure 2.28:

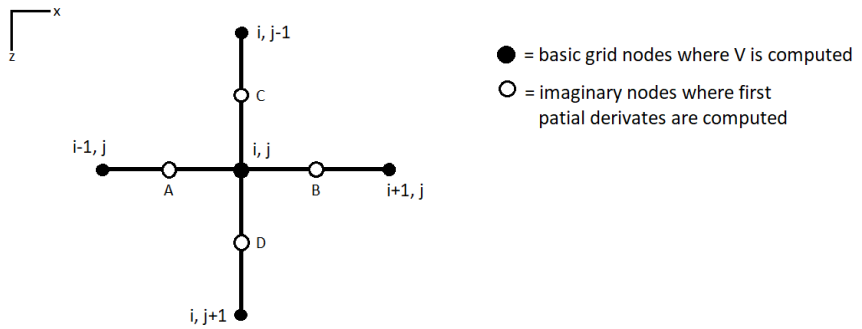

$$(2.27) \quad \left[\left(\frac{V_{i+1,j}-2V_{i,j}+V_{i-1,j}}{\Delta x^2}\right)+\left(\frac{V_{i,j+1}-2V_{i,j}+V_{i,j-1}}{\Delta z^2}\right)\right]=0$$

Figure 2.28 The finite difference approximation for the Laplace equation 2.22

Equation 2.27, shown in Figure 2.28, can be applied to all the nodes of the grid, in this way a system of algebraic equations is created, which can be solved iteratively. Therefore, we are able to find the value of V in each node of the grid. With iterative methods, the successive approximations of the solution to the mathematical problem examined are calculated with the previous approximations. For instance, if we consider Jacobi's iterative scheme, with a uniform grid (Δx=Δz), the iterative pattern is (k is the iteration moment):

$$(2.28) \quad V_{i,j}^{k+1} = \frac{V_{i+1,j}^{k}+V_{i-1,j}^{k}+V_{i,j+1}^{k}+V_{i,j-1}^{k}}{4}$$

Note that, to start the iterative cycle we must define initial values of V in each node and the iteration process continues until the difference between two successive approximations, R (the residual), reaches a sufficiently low threshold (convergence criterion):

$$(2.29) \quad R = V_{i,j}^{k+1} - V_{i,j}^{k}$$

In the finite difference method, the grid can be uniform (equal distance between nodal points) or non-uniform, but points need to be orthogonal (structured quadrilateral mesh with cells). Instead, the finite element method allows us to create unstructured grids where the points of the grid don't need to be orthogonal, making easier to create complex shapes domains (Anderson, 1992). This is very helpful when the topography is not flat and, for this reason, the finite element method tends to be more used in the inversion codes. In Figure 2.29 we can see an example that show how unstructured mesh (b) allows to reproduce complex shape domains more effectively than structured meshes (a).

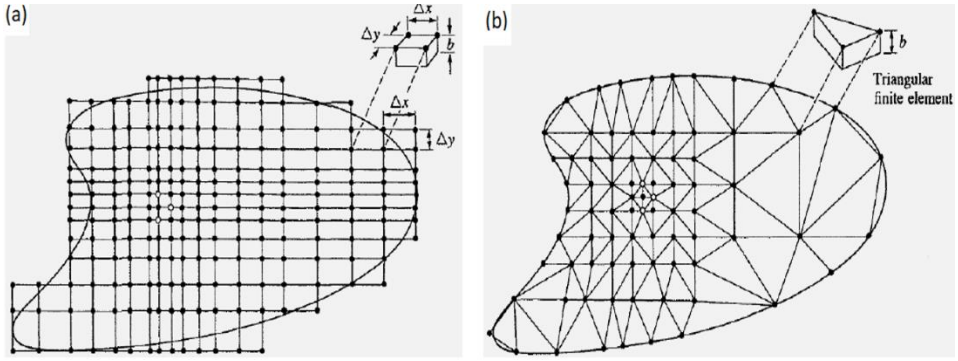

Figure 2.29 Example of (a)structured mesh and (b)unstructured mesh

The finite element method is another technique for solving partial differential equations. The first step of the finite element method involves choosing an element-type which defines where and how the discretization is carried out. The simplest element for one dimensional problem is a 2-node element, as shown in Figure 2.30.a. We can use more nodes per element which will have the effect of increasing accuracy of the solution but also increasing the amount of equations to be solved and thus the cost of numerical solution. The second step of the finite element method involves approximating the continuous variable V in terms of nodal variables V_i using simple functions N, called shape functions. If we focus on one element which, in our example, contains 2 nodes and we assume that the electrical potential varies linearly between the two nodes, we find that:

$$(2.30) \quad V \approx N_1 V_1 + N_2 V_2$$

or using matrix notion:

$$(2.31) \quad V \approx [N_1 \quad N_2] \begin{bmatrix} V_1 \\ V_2 \end{bmatrix} = NV$$

In equations 2.30 and 2.31, V is the continuous variable which we are approximating within any given element in terms of the potential at the two nodes V_1 and V_2. Since we made the choice that potential varies linearly between two nodes, we are using the following shape functions:

$$(2.32) \quad N_1 = 1 - \frac{x}{L} \quad ; \quad N_2 = \frac{x}{L}$$

In equations 2.32, L is the length of the element and, as you we can see in Figure 2.30.b, x is the spatial variable which varies from 0 at node 1 to L at node 2.

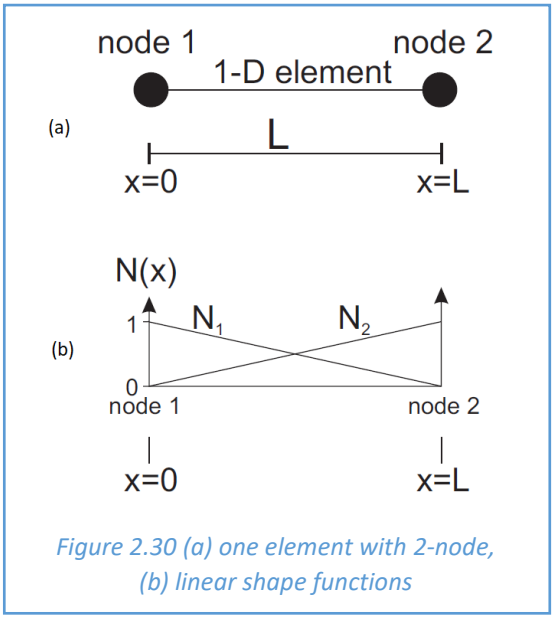

Figure 2.30 (a) one element with 2-node, (b) linear shape functions

Important properties of the shape functions are:

- $N_1 = 1$ at node 1 while $N_1 = 0$ at node 2;
- $N_2 = 0$ at node 1 while $N_2 = 1$ at node 2;
- $N_1+N_2 = 1$ (over the entire element);
- the functions only connect nodes of the related element.

Note that, the shape functions are simply interpolating functions, they are used to interpolate the solution over a finite element. The choice of the shape functions is directly related to the choice of the element type (Schmalholz & Kaus, 2008). Despite this, the next step of the finite element method is to substitute equation 2.31 into the governing differential equation. For instance, if we consider the Laplace equation 2.22, we find that:

$$\frac{\partial^2}{\partial x^2}\left(\begin{bmatrix} N_1 & N_2 \end{bmatrix}\begin{bmatrix} V_1 \\ V_2 \end{bmatrix}\right) = R \tag{2.33}$$

R (the residual) is a measure of the error introduced during discretization. Note that the original partial differential equation has now been replaced by an equation in the discretized (nodal) variables V_1 and V_2. Thus, we now have one equation for two unknowns, which obviously cannot be solved. The problem now reduces to finding values for V_1 and V_2 such that the residual is minimized (ideally R is zero). However, to do this we have to generate a system of equations where the number of equations equals the number of unknowns. In the finite element method, the unknown coefficients V_i are determined by requiring that the integral of the weighted residual is zero on an element basis. To achieve this step practically, we must multiply (or "weight") the residual in equation 2.33 by a set of weighting functions (each in turn), integrate over the element and equate to zero. Many methods can be used (e.g. collocation, subdomain, least squares, Galerkin, etc), the difference between which depends on the choice of the weighting functions. For instance, with the Galerkin method the weighting functions are chosen to be identical to the shape functions N, thus for the equation 2.33 we obtain:

$$\int_0^L \begin{bmatrix} N_1 \\ N_2 \end{bmatrix}\frac{\partial^2}{\partial x^2}\left(\begin{bmatrix} N_1 & N_2 \end{bmatrix}\begin{bmatrix} V_1 \\ V_2 \end{bmatrix}\right) dx = \begin{bmatrix} 0 \\ 0 \end{bmatrix} \tag{2.34}$$

If the shape functions are linear, as in our example, double differentiation of these functions would cause them to vanish. This problem is resolved by applying Green's theorem (integration by parts):

$$\int N_i \frac{\partial^2 N_j}{\partial x^2} dx = -\int \frac{\partial N_i}{\partial x}\frac{\partial N_j}{\partial x} dx + \textit{boundary terms} \tag{2.35}$$

The boundary terms are typically ignored. If we apply equation 2.35 to equation 2.34, we will find:

$$-\int_0^L \begin{bmatrix} \frac{\partial N_1}{\partial x}\frac{\partial N_1}{\partial x} & \frac{\partial N_1}{\partial x}\frac{\partial N_2}{\partial x} \\ \frac{\partial N_2}{\partial x}\frac{\partial N_1}{\partial x} & \frac{\partial N_2}{\partial x}\frac{\partial N_2}{\partial x} \end{bmatrix} dx \begin{bmatrix} V_1 \\ V_2 \end{bmatrix} = \begin{bmatrix} 0 \\ 0 \end{bmatrix} \tag{2.36}$$

Therefore, now we have two equations for the two unknowns V_1 and V_2. By evaluating the integrals (using N_i defined in equation 2.32), equation 2.36 becomes:

$$\begin{bmatrix} \frac{1}{L} & -\frac{1}{L} \\ -\frac{1}{L} & \frac{1}{L} \end{bmatrix}\begin{bmatrix} V_1 \\ V_2 \end{bmatrix} = \begin{bmatrix} 0 \\ 0 \end{bmatrix} \tag{2.37}$$

Equation 2.37 can be simplified using matrix notation:

$$SMV = 0 \tag{2.38}$$

Where SM and V are:

$$(2.39)\quad SM = \begin{bmatrix} \frac{1}{L} & -\frac{1}{L} \\ -\frac{1}{L} & \frac{1}{L} \end{bmatrix} = \begin{bmatrix} SM_{11} & SM_{12} \\ SM_{21} & SM_{22} \end{bmatrix}$$

$$(2.40)\quad V = \begin{bmatrix} V_1 \\ V_2 \end{bmatrix}$$

The matrix SM is referred to as the element stiffness matrix and V is the unknown element vector. Note that, at this point we have carried out the discretization only for a single element, whereas we generally want to divide the domain into many elements so we can obtain a more accurate solution. Thus, we can consider a one-dimensional mesh consisting of 4 elements, as shown in Figure 2.31:

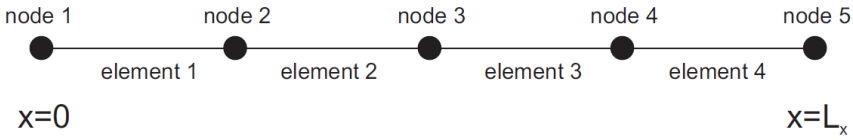

Figure 2.31 Example of one-dimensional mesh with 4 elements and 5 nodes

In this situation, instead of having just 2 unknowns we have 5, which are related to the five nodes of the mesh. In this case, we can generate a global matrix equation by summing node-by-node the matrix equation derived for a single element (equation 2.38), as we can see in Figure 2.41. Note that, whereas node 1 contains a contribution only from element 1, node 2 has contributions from both elements 1 and 2. Performing this process, using the notation introduced above, and assuming that each element matrix is the same, leads to:

$$(2.41)\quad \begin{bmatrix} SM_{11} & SM_{12} & 0 & 0 & 0 \\ SM_{21} & SM_{22}+SM_{11} & SM_{12} & 0 & 0 \\ 0 & SM_{21} & SM_{22}+SM_{11} & SM_{12} & 0 \\ 0 & 0 & SM_{21} & SM_{22}+SM_{11} & SM_{12} \\ 0 & 0 & 0 & SM_{21} & SM_{22} \end{bmatrix} \begin{bmatrix} V_1 \\ V_2 \\ V_3 \\ V_4 \\ V_5 \end{bmatrix} = \begin{bmatrix} 0 \\ 0 \\ 0 \\ 0 \\ 0 \end{bmatrix}$$

which, using matrix notation, becomes:

$$(2.42)\quad SM_G V = 0$$

the subscript G indicates that the matrices and vectors refer to the entire 'global' problem and not simply to a single element. Note that, a system of 5 equation has been created, which can be iteratively solved to find V in each node (Schmalholz & Kaus, 2008). Obviously, this was a very simple example, meshes for real problems are 2D (or even 3D), the number of nodes ranges from several hundred to thousands and thus also the number of equations. Furthermore, we can't apply the Laplace equation 2.22 but we need to discretize the Poisson equation 2.23.

It is important to specify that finite element methods do not necessarily provide greater accuracy than finite difference methods. Finite difference method have the advantage of being simpler to implement and can be computationally more efficient for specific problems, particularly in terms of computer storage, whereas the key advantages of finite element method is the ability to geometrically represent arbitrary structures and mesh refinement in unstructured meshes (Binley,

2015). As previously introduced, with finite element method the grid nodes don't need to be orthogonal and this allows us to build both structured and unstructured grids. In 2D models, the elements of the grid can be quadrilateral or, more typically, triangular and, if the investigated domain is isotropic, each element should be built in such a way that the ratio between the maximum and minimum size of the element are close to the unit (Anderson, 1992). Note that, if the nodes are placed only at the vertices of the elements, linear interpolation functions can be used. Moreover, if element size changes are foreseen, this must be done gradually through transition areas (the same goes for finite difference cells). In Figure 2.32 are shown examples of quadrilateral structured mesh (a), quadrilateral unstructured mesh (b) and triangular unstructured mesh (c):

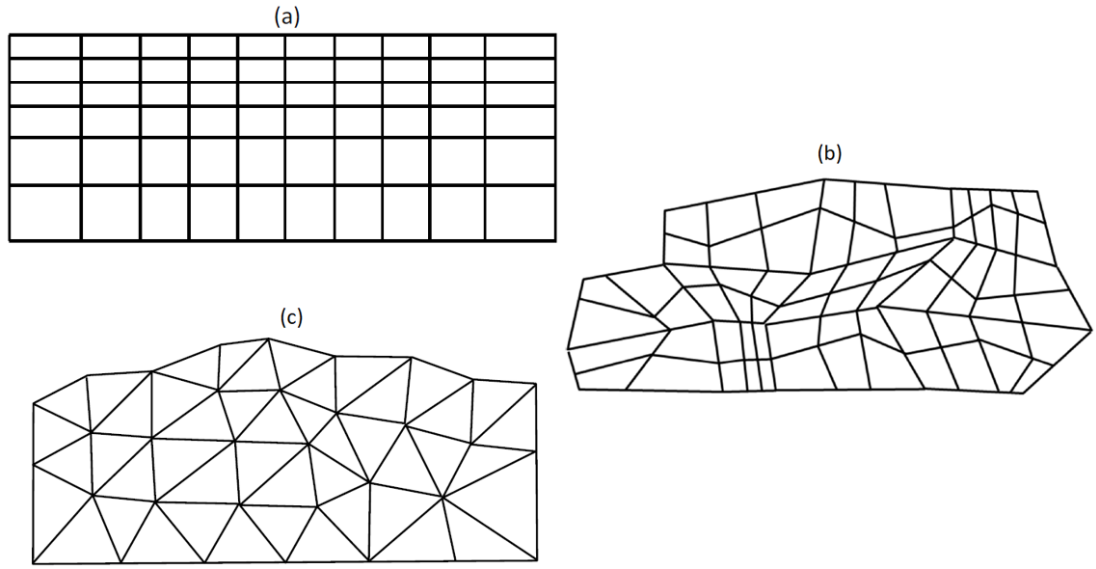

Figure 2.32 Examples of (a) quadrilateral structured mesh, (b) quadrilateral unstructured mesh and (c) triangular unstructured mesh

The triangular unstructured meshes are preferred due to the full flexibility in mapping the geometry of the problem, which is particularly useful when the topography is not flat. Obviously, this implies the use of the finite element method. An example is shown in next Figure 2.33:

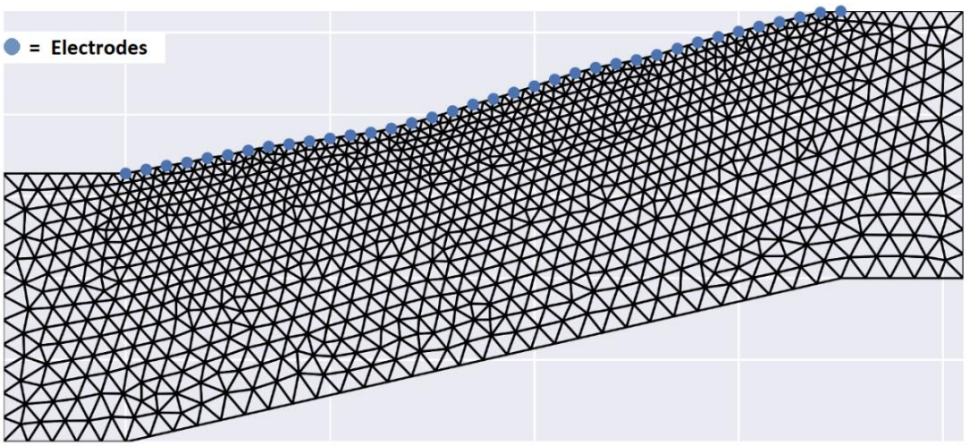

Figure 2.33 Example of an unstructured triangular mesh with variable topography

Regardless by the mesh type (structured or unstructured) and numerical method (finite difference or finite element), the mesh should clearly cover the survey area laterally and the expected depth of investigation. However, given that injected current will transfer further horizontally and

vertically, the mesh should extend sufficiently in order to account for this. As we can see in Figure 2.33, there is no need to retain a fine discretisation in these 'infinite' boundary regions. It is good practice to let the elements gradually increase in size laterally and vertically outside the region of investigation, so that the number of equations applied to the mesh decreases and therefore also the cost of the numerical solution. Figure 2.34 illustrates an example of zone discretisation for a surface electrode array, DOI is the depth of investigation and zone A is the region of interest. Elements should be finely discretised especially near the electrodes, as we can see in Figure 2.33. Zone B has the same discretisation as A and is included to ensure good accuracy of the forward calculations; this zone typically extends two or three time the electrode spacing. If we apply only no flux boundaries, zone C typically extends ~5L (L is the length of the longest current dipole). Instead, if we apply mix boundaries, zone C can be much less extensive, as we can see in Figure 2.33. Discretisation should gradually get coarser in Zone C, moving away from the region of investigation (Binley, 2019).

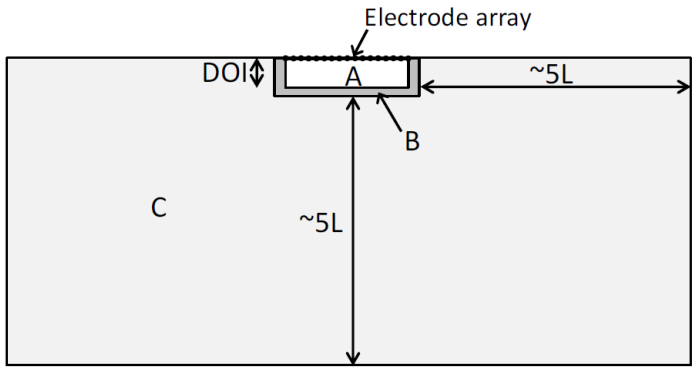

Figure 2.34 Example of zone discretisation for a surface electrode array

The similar concepts are applied to meshes of cross-borehole surveys. As discussed in chapter 2.2, this kind of investigation has the advantage of increasing the resolution in the depth area between the two holes. In this area, therefore, the discretization of the elements must be particularly dense, as shown for example in Figure 2.35:

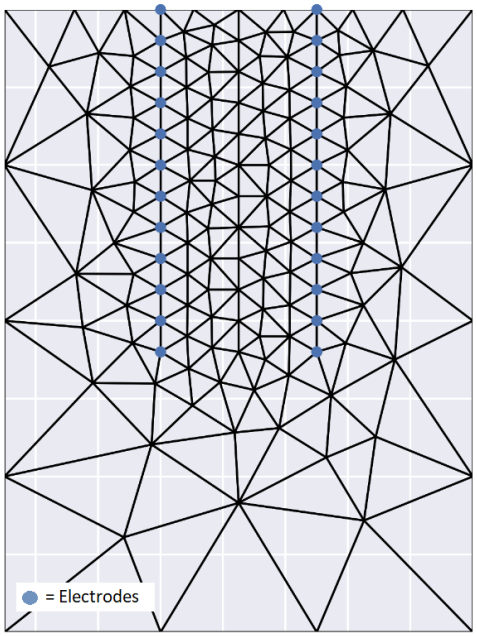

Figure 2.35 Example of a triangular mesh for a cross-borehole survey

At this point, starting from a known subsoil structure (thicknesses and relative conductivity of the layers) and a line of electrodes, we can discretize the investigated domain with a mesh and numerically calculate, by applying Poisson's equation 2.23 and relative boundaries, the potentials that will arise at all the electrodes of the line if we apply a potential difference ΔV to two energizing electrodes A-B, promoting the circulation of electric current i. Therefore, we are able of calculating the potential differences for any pair of potentiometric electrodes M-N of the line and consequently we can determine the apparent resistivities with the equation 2.9. In simple words, it is possible to simulate synthetic data for different survey geometries and to create the related pseudosections. As previously introduced, this process is called “forward problem” or “forward modeling” and we can see an example in Figure 2.36:

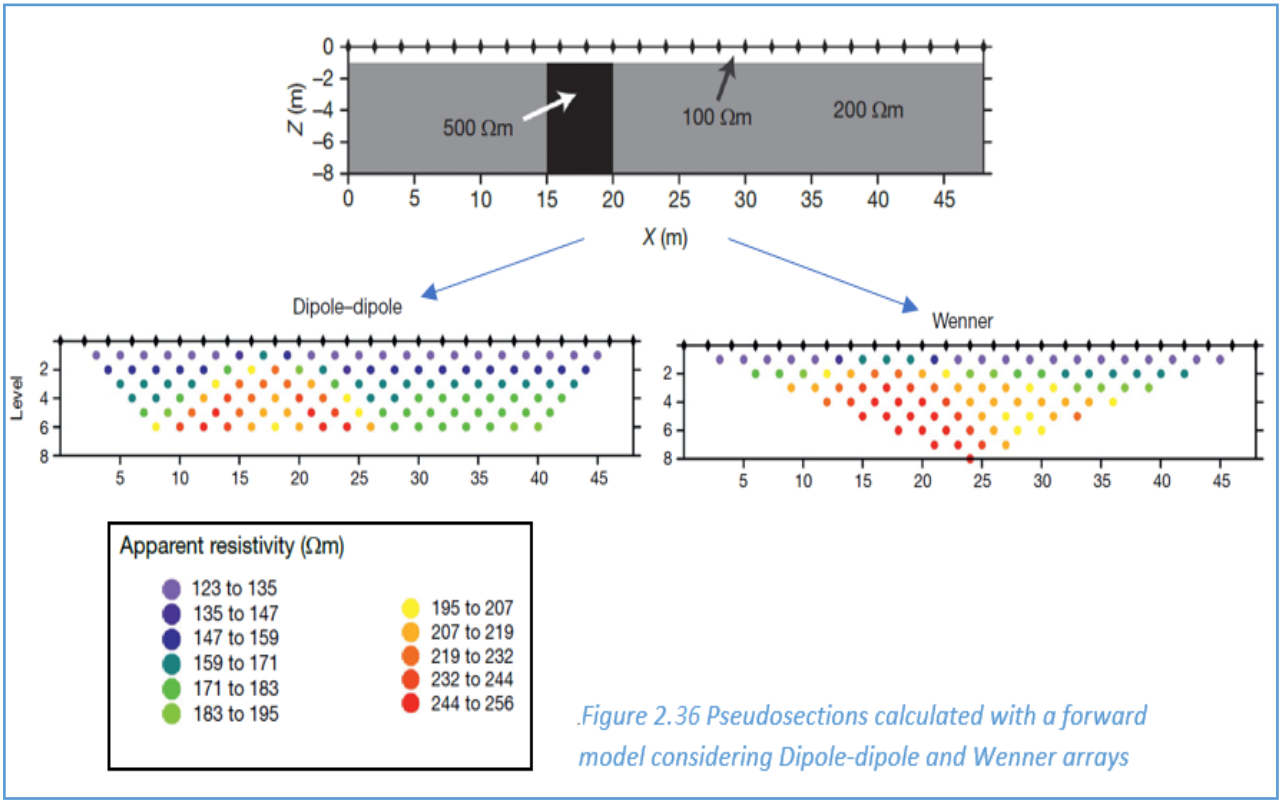

Figure 2.36 Pseudosections calculated with a forward model considering Dipole-dipole and Wenner arrays

In inversion codes, forward models are used within an optimization framework to calculate predicted data for comparison with observed data. Given a set of measurements (observed data), the distribution of electrical properties is sought that explains the observations to an acceptable degree. As already discussed, for resistivity surveys data will be in the form of apparent resistivities, and the model will be parameterized in terms of resistivity or conductivity. Unfortunately, there is no unique solution to the inverse problem. As all geophysical techniques, electrical methods bear a certain degree of inherent non-uniqueness, due to fact that a variety of different subsoils models can produce the same response (observed data). However, by systematically restricting the model search in the inversion process, for instance by claiming predefined model characteristics, a “unique” solution with practical relevance can be obtained. This is usually accomplished by formulating the inverse problem as a regularized optimization problem, which involves minimization of an objective function comprising both data misfit (measured vs modeled) and a penalty term accounting for deviations from the desired model attributes (Binley & Kemna, 2005).

To formulate the inverse problem, the considered distribution of electrical properties is discretized into a set of parameters defining a model vector m. While for a 1D resistivity problem, m is given by a set of resistivities and related layer thicknesses, for 2D or 3D models, m correspond to the resistivities of the individual elements or cells of the mesh used in the forward modeling.

$$(2.43) \quad m_j = ln\rho_j \quad (j = 1, \dots, M)$$

In equation 2.43 the logarithm accounts for the large possible range in earth conductivity. Analogously, the given set of measured apparent resistivities is assembled in a data vector d:

$$(2.44) \quad d_i = ln\rho_i \quad (i = 1, \dots, N)$$

Again, log-transformed data are normally used on account of the wide range in observed apparent resistivities for arbitrary electrode configurations. At this point, the inverse problem involves finding a model m which, using the forward mapping according to equations 2.23, reproduces data d to the specified level of uncertainty. Most geoelectrical inverse models used today are based on a least-squares fit between data and model parameters. We can express the data-model misfit as:

$$(2.45) \quad \Phi_d = (d - F(m))^T W_d^T W_d (d - F(m))$$

where F(m) is the set of equivalent apparent resistivities that forward model estimated with parameter set m and W_d is a data weight matrix, which, if we consider the uncorrelated measurement error case and ignore forward model errors, is a diagonal matrix with entries equal to the inverse of standard deviation ε_i of each measurement (standard deviation of each quadripole is defined through the stacking process): $W_d = \text{diag}(1/\varepsilon_1, \dots, 1/\varepsilon_N)$. Applying such weights permits the differential weighting of poor and good data, according to their reliability. However, in numerous applications of geoelectrical inversion, such a criterion is not adopted and often the user displays an equivalent uniform data error, defined with the reciprocity check, that the final model represents (Binley, 2015). Attempts have been made to minimize Φ_d in equation 2.45 using a variety of automated curve matching procedures (e.g., Barker, 1992; Zohdy, 1989). However, many of these proved to be susceptible to slow convergence (or even divergence) of the solution. It was Occam's method (after Occam's razor) proposed by Constable et al. (1987) that offered a breakthrough in geoelectrical inverse modeling and is fundamental for most of the inverse solutions today. The method searches for the smoothest model (set of parameters) that is consistent with the measured data and utilizes spatial regularization (Tikhonov & Arsenin, 1977) to enforce the smoothing, which also helps ensure a stable and unique solution. Regularizing the minimization problem can be achieved by adding a model penalty term:

$$(2.46) \quad \Phi_m = m^T R m$$

where R is a roughness matrix that describes a spatial connectedness of the parameter call values. For example, if we consider three parameters m_1, m_2, and m_3 in a 1D arrangement, R is written as shown in Figure 2.37:

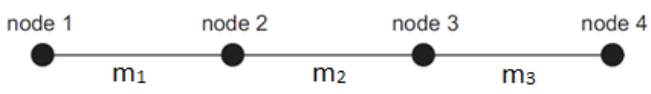

$$(2.47) \quad R = \begin{bmatrix} 1 & -1 & 0 \\ -1 & 2 & -1 \\ 0 & -1 & 1 \end{bmatrix}$$

Figure 2.37 Example of roughness matrix R for three parameters (m_1, m_2, and m_3) in a 1D arrangement

Therefore, we wish to seek the minimum of the equation:

$$\Phi_{total} = \Phi_d + \alpha\Phi_m \quad (2.48)$$

where α is a scalar that controls the emphasis of the smoothing. In an Occam's solution, we seek to satisfy the minimization of equation 2.48, subject to the largest value of α. The process is achieved by utilizing the Gauss–Newton approach, which results in the iterative solution of:

$$(J^T W_d^T J + \alpha R)\Delta m = J^T W_d^T (d - F(m_k))\alpha R m_k \quad (2.49)$$

$$m_{k+1} = m_k + \Delta m \quad (2.50)$$

Where m_k is the parameter set at iteration k, Δm is the parameter update at iteration k and J is the Jacobian (or sensitivity) matrix, given by:

$$J_{i,j} = \frac{\partial d_i}{\partial m_j} \quad (2.51)$$

Typically, it is preferable to adjust the scalar α through the iterative steps, initially starting with a large value and reducing the value until convergence has been reached (Binley, 2015). Furthermore, note that the penalty function in equation 2.46 can be expressed in terms of a difference relative to a reference model m_{ref}:

$$\Phi_m = (m - m_{ref})^T R(m - m_{ref}) \quad (2.52)$$

This is very useful in time-lapse investigations, in fact LaBrecque and Yang (2001) used m_{ref} as the baseline resistivity model (prior to any change) and then they adopted the following modification to equation 2.49:

$$(J^T W_d^T J + \alpha R)\Delta m = J^T W_d^T [(d - d_{ref})(F(m_i) - F(m_{ref})]\alpha R(m_i - m_{ref}) \quad (2.53)$$

where d_{ref} is the baseline data vector. This approach, which effectively focuses on removing the effect of systematic errors, has proved effective in many numbers of time-lapse imaging studies (e.g. Doetsch et al., 2012; LaBrecque et al., 2004).

Therefore, starting from the dataset measured in the field, we can process the dataset with an inversion code which, through the iterative process shown in this chapter, will minimize the equation 2.49. Being an iterative process, it is necessary to provide initial resistivity values in the cells/elements of the mesh with which the iterative cycle can start; typically a uniform resistivity is assigned in all cells/elements of 100 Ω*m. Note that, simpler inversion programs (e.g. Profiler, Binley) automatically generate the discretization mesh by indicating the position (x, y, z) of the electrodes, while more advanced inversion codes (e.g. R2, Binley or CRTomo, Kemna & Weigand) require an input mesh file where nodes and elements need to be specified. To create a mesh, we can use open-source programs such as GMSH (Geuzaine & Remacle, 2009). Nevertheless, all the inversion codes will provide an output file where the coordinates of many points and the relative resistivity values are shown (e.g. Figure 2.38.a); the number of points depend on the discretization of the mesh. The output file can be used to create a resistivity section using programs for data analysis and visualization, such as Surfer (Golden Software) or ParaView. These programs allow us to interpolate the data of the output file and thus to create a resistivity section. Note that, the interpolation technique (e.g. Kriging or Natural Neighbor) is irrelevant because the available data are usually so numerous that the result is the same regardless of the interpolation technique.

However, commercial inversion codes typically provide directly the resistivity section. It should be emphasized that the quality of the inversion is the same as for open source codes, the only advantage is the direct graphic return after the inversion. Figure 2.38.a highlights an example (obviously incomplete) of an output file provided by an open-source inversion code, R2 (Binley), which works with the finite element method, by processing the dataset of the survey obtained in Prato della Valle (Figure 2.21 chapter 2.3) with the Syscal Pro (after reciprocal measurements check – Figure 2.24). The result of the graphic interpolation (resistivity section) performed with Surfer, is shown in Figure 2.39.b:

(a)

x	z	resistivity	log(resistivity)
0.30551E+02	-0.51007E+01	0.16281E+03	0.22117E+01
0.15326E+02	-0.11573E+01	0.89648E+02	0.19525E+01
0.44611E+02	-0.29317E+01	0.46167E+02	0.16643E+01
0.25030E+01	-0.40557E+01	0.67867E+02	0.18317E+01
0.97237E+01	-0.15177E+01	0.73290E+02	0.18650E+01
0.39059E+02	-0.34270E+01	0.74482E+02	0.18721E+01
0.24670E+01	-0.47363E+01	0.74981E+02	0.18749E+01
0.43801E+02	-0.90213E+01	0.36573E+02	0.15632E+01
0.32933E+00	-0.44730E+01	0.67224E+02	0.18275E+01
0.29377E+02	-0.55993E+01	0.19570E+03	0.22916E+01
0.27514E+02	-0.89000E+00	0.11697E+03	0.20681E+01
0.21514E+02	-0.89000E+00	0.75095E+02	0.18756E+01
0.45604E+02	-0.20373E+01	0.70898E+02	0.18506E+01
0.39013E+02	-0.88667E+00	0.11026E+03	0.20424E+01
0.19677E+02	-0.72787E+01	0.32357E+03	0.25100E+01
0.25678E+02	-0.72783E+01	0.29364E+03	0.24678E+01
0.29432E+02	-0.59650E+01	0.21473E+03	0.23319E+01
0.13582E+02	-0.42267E+00	0.12096E+03	0.20826E+01
0.45470E+02	-0.21997E+01	0.65444E+02	0.18159E+01
0.34707E+02	-0.68230E+01	0.20165E+03	0.23046E+01
0.29440E+02	-0.36693E+01	0.81319E+02	0.19102E+01
0.23425E+02	-0.36627E+01	0.11030E+03	0.20426E+01
0.17425E+02	-0.36633E+01	0.11270E+03	0.20519E+01

(b)

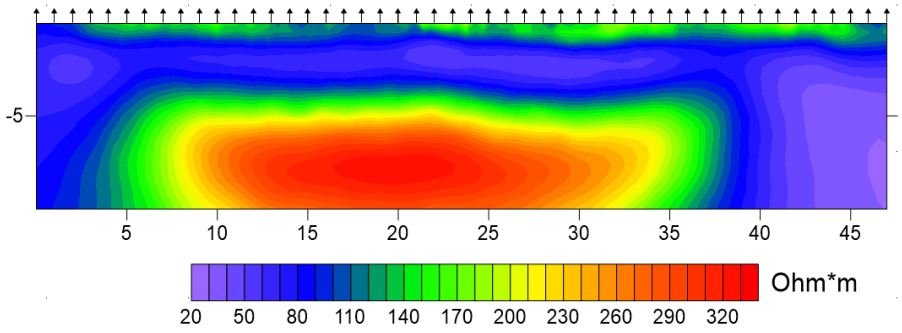

Figure 2.38 (a) Example of an output file obtained after the inversion process with R2 and (b) the resistivity section created with Surfer (dataset of Prato della Valle survey – Chapter 2.3)

From Figure 2.38.a we can see that in the output file the resistivities are also reported with a logarithmic scale (fourth column). This is very useful when the resistivity variations in the medium are very small. If we create a section by interpolating the log resistivity data, we can appreciate

much better the small variations of resistivity in the subsoil, for instance in time-lapse investigations aimed to monitoring variations of humidity in the subsoil. Furthermore, it should be noted that the section returned by Surfer (Figure 2.38.b) is not totally correct and needs to be modified. Resistivity has been interpolated in points where we don't have measurements. As we can see in the pseudosections of Figure 2.13 and 2.14, the depth of investigation along the line of investigation is not constant, it is maximum in the central area and decreases towards the lateral ends. In most 2-D surface imaging applications a trapezium boundary is constructed, following a similar pattern to that shown in the pseudosections of Figure 2.13 and 2.14. However, variation in resistivity will impact on the spatial sensitivity and such linear boundaries may be inappropriate. Furthermore, for more complex geometric arrangements (e.g., borehole-based imaging or 3-D imaging), such simplistic approaches are inadequate. Therefore, the spatial resolution of the inversion process should be assessed prior to any construction of section boundaries and interpretation of results (Binley, 2015). Generally, model resolution is a complicated function of numerous factors, including electrode layout, measurement scheme, data signal-to noise ratio, and resistivity distribution, as well as parameterization and regularization used in the inversion (Binley & Kemna, 2005). According to inverse theory (Menke, 1989), the model resolution matrix (R^M) can be computed, for the equation 2.53, by applying the following report:

$$(2.54) \quad R^M = (J^T W_d^T W_d J + \alpha R)^{-1} (J^T W_d^T W_d J)$$

where the Jacobian J has been computed based on the final (inverted) parameter set and the regularization scalar α is the value at the end of the inversion. R^M can be also defined as:

$$(2.55) \quad m = R^M m_{true}$$

where m is the vector of parameters obtained by the inversion and m_{true} is the vector of true (unknown) parameters. Thus, the ideal structure of R^M is the identity matrix, since this implies a perfect mapping of true and inverted parameter vectors. Any deviation from the identity matrix reveals the lack of sensitivity of the parameter values to the measured data, coupled with the effect of smoothing and other regularization (Binley, 2015). Since the actual calculation of R in large-scale inverse problems is cumbersome, alternative approaches, based on a simple accumulated sensitivity map, have been adopted (Park & Van, 1991; Kemna, 2000):

$$(2.56) \quad S_j = (J^T W_d^T W_d J)_{jj}$$

Equation 2.56 is a computationally inexpensive alternative for image appraisal. One value of S (the diagonal of $[J^T W^T W J]$) is stored for each element/cell of the mesh. High values of S indicate high sensitivity and low values indicate poor sensitivity. Obviously, resolution is supposed to be low in model regions where sensitivity of the measurements is poor (S shows low values) and the correspondingly regularization is more influential (Binley & Kemna, 2005). Many inversion codes provide an output file containing the sensitivity values for the points where the resistivity has been defined. Even these values can be interpolated with Surfer and thus a sensitivity map can be obtained, typically plotted with a log scale. This image can be used to define, more correctly, the boundaries of the resistivity section and to interpret, more reliably, the inversion results. Considering the example of Figure 2.38, in the following Figure 2.39 we can see (a) the sensitivity output file (obviously incomplete) and (b) the sensitivity map (log scale), created with Surfer by interpolating all the data of the sensitivity output file.

(a)

x	z	s	log(s)
0.30551E+02	-0.51007E+01	0.26180E-01	-0.15820E+01
0.15326E+02	-0.11573E+01	0.41511E+00	-0.38183E+00
0.44611E+02	-0.29317E+01	0.16390E-01	-0.17854E+01
0.25030E+01	-0.40557E+01	0.17294E-01	-0.17621E+01
0.97237E+01	-0.15177E+01	0.33931E+00	-0.46940E+00
0.39059E+02	-0.34270E+01	0.15807E+00	-0.80114E+00
0.24670E+01	-0.47363E+01	0.65141E-02	-0.21861E+01
0.43801E+02	-0.90213E+01	0.18733E-02	-0.27274E+01
0.32933E+00	-0.44730E+01	0.43090E-02	-0.23656E+01
0.29377E+02	-0.55993E+01	0.16662E-01	-0.17783E+01
0.27514E+02	-0.89000E+00	0.38840E+01	0.58928E+00
0.21514E+02	-0.89000E+00	0.53129E+00	-0.27467E+00
0.45604E+02	-0.20373E+01	0.39143E-01	-0.14073E+01
0.39013E+02	-0.88667E+00	0.10683E+01	0.28677E-01
0.19677E+02	-0.72787E+01	0.12055E-01	-0.19188E+01
0.25678E+02	-0.72783E+01	0.11887E-01	-0.19249E+01
0.29432E+02	-0.59650E+01	0.16729E-01	-0.17765E+01
0.13582E+02	-0.42267E+00	0.14457E+01	0.16009E+00
0.45470E+02	-0.21997E+01	0.34874E-01	-0.14575E+01

(b)

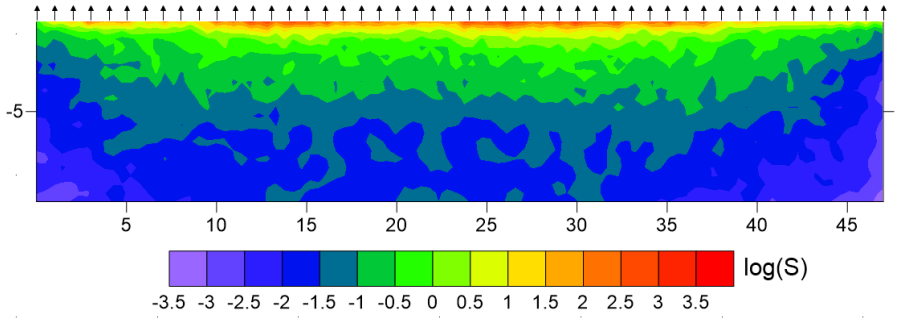

Figure 2.39 (a) Example of sensitivity output file and (b) sensitivity map for the data in Figure 2.38.a

As expected, the sensitivity is maximum at the surface near the electrodes, while decreases with the depth and towards the lateral limits where there are no measurements. Therefore, Figure 2.39.b can be used to trace the lateral and vertical boundaries of the section, as shown in Figure 2.40:

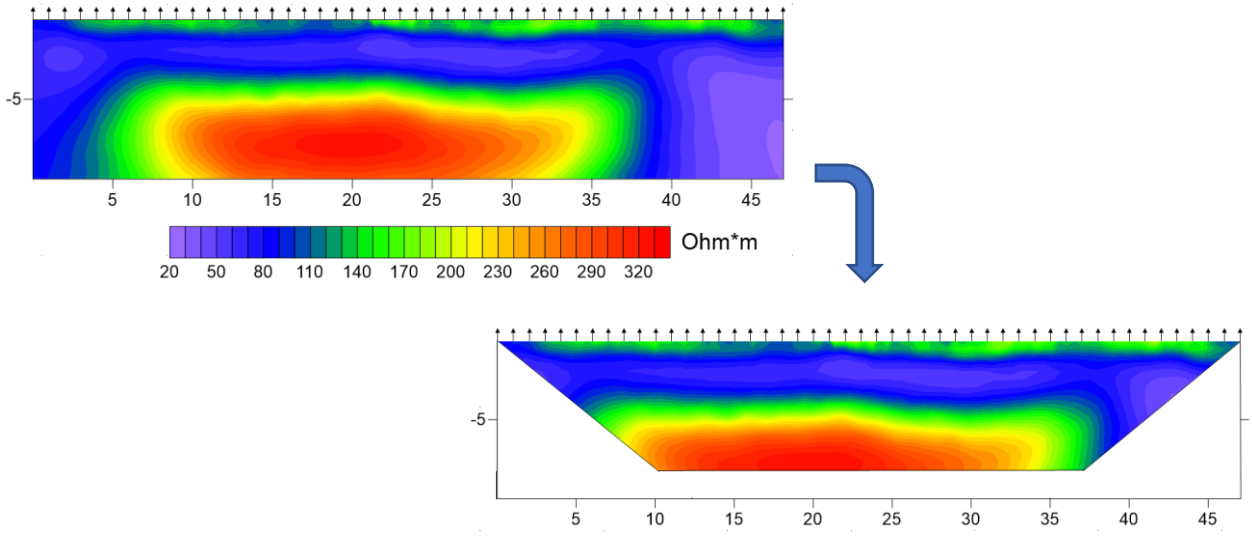

Figure 2.40 Final resistivity section for the survey of Prato della Valle (Figure 2.21.b)

The interpretation of the resistivity section in Figure 2.40 is not particularly complicated, since the investigation was carried out in loose soil (low resistivity) and the target of the investigation were the remains of the ancient Roman theater (rock walls). Therefore, the area with hight resistivity that appears at a depth of about 5 meters can be safely associated with this structure. Note that, prior knowledges of the survey site are very important (e.g. characteristics about the environment of the investigation and features of the target), either for the choice of the geophysical technique itself but also in the data processing and interpretation of the results. We cannot use DC methods if is foreseen that materials in the investigated subsoil don't have resistivity contrasts. Furthermore, we must be sure to be able to create a suitable electrode line (length and spacing) to detect the target of the investigation. If the investigation environment is positive for the DC resistivity method, after its achievement, with the most suitable configuration (Wenner, Dipole-dipole, Schlumberger, etc.) depending on the target, even during the processing phase it is possible to use prior knowledges of the survey site. For instance, anisotropy of the spatial regularization can be easily achieved by simple modification to the roughness matrix R, in equation 2.46. This allows us to enhance smoothing in one or more direction based on a priori information. To better understand the importance of the prior knowledges of the survey site, we can consider Figure 2.41 and Figure 2.42.

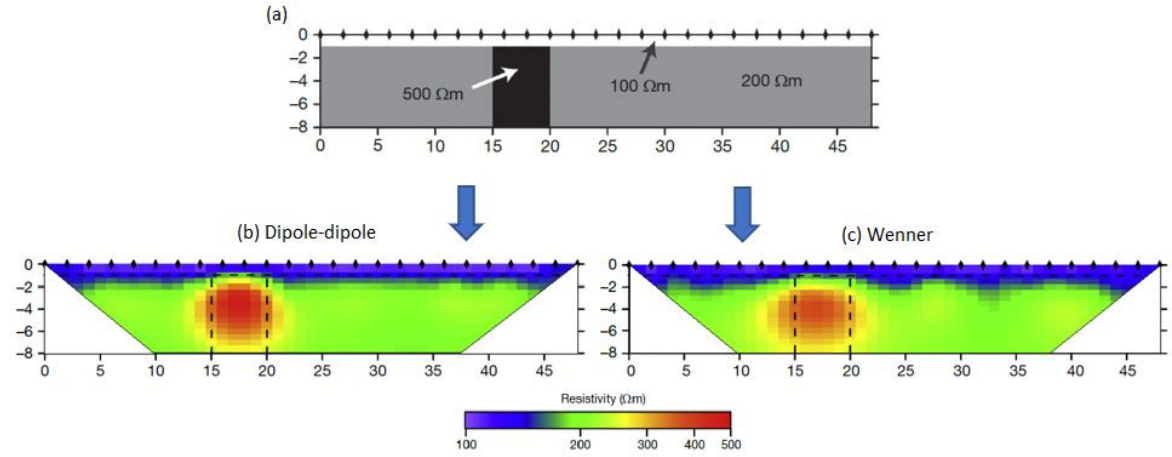

Figure 2.41 (a) Resistivity structure model; inverted models with isotropic regularization for Dipole–dipole (b) and Wenner (c); the dashed lines show the boundaries of the true model

Starting from the subsoil structure shown in Figure 2.41.a, we can assume that the same line of electrodes has been measured with both Dipole–dipole and Wenner configurations. If we consider the inverted models with isotropic regularization (Figure 2.41.b/c) and if the survey target is the less conductive vertical object, the resistivity section obtained with a Dipole-dipole array is, as expected, definitely preferable instead that obtained with Wenner configuration. As previusly discussed, with some codes as R2 (Binley) and CRTomo (Kemna), prior information of the subsoil structure can be used even during the processing phase. If we still consider Figure 2.41.a, Dipole-dipole data can be inverted with enhanced regularization in the horizontal and in the vertical direction:

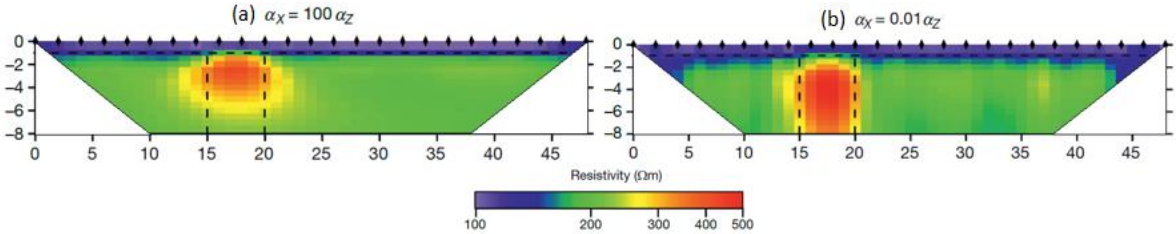

Figure 2.42.a Dipole-dipole inverted models: (a) enhanced horizontal smoothing (b) enhanced vertical smoothing

As we can see in Figure 2.42.a, if the data are inverted with enhanced regularization in the vertical direction (b), the less conductive structure can be outlined more precisely. On the other hand, if we enhance the horizontal smoothing (a), we can define much better the horizontal stratigraphy. An excellent compromise is to realize both the inversion models, in this way is possible to make easier the interpretation of the investigated subsoil, as the structures are rarely well known as in this example. Instead, in situations where the position of the objects in the subsoil are perfectly known, with some codes as R2 (Binley), the spatial regularization can be modified by removing the smoothing at such locations. Considering again the subsoil structure in Figure 2.41.a, if this time we assume that we know perfectly the position of the less conductive vertical object, we can invert the Dipole–dipole data as in Figure 2.41.b, except for a minor modification to the roughness matrix that removes smoothing along the boundary of the object. Note that, we need to know exactly which elements/cells of the mesh make up the less conductive structure because they need to be defined in the input file of the inversion. Nevertheless, smoothing still exists across parameter elements/cells within and outside this boundary. Figure 2.42 shows the result of this inversion:

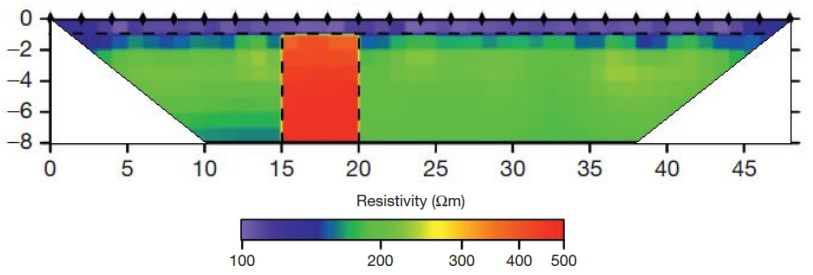

Figure 2.42.b Resistivity section if a disconnection in regularization is applied at the boundaries of the high resistive object

In Figure 2.42.b we can appreciate that this resistivity section is the best of those obtained so far with the various inversion processes, demonstrating how effective such a priori (correct) information can be. For instance, Slater and Binley (2006) took this approach in their study of geoelectrical imaging of permeable reactive barriers, where the engineered structure boundaries were perfectly known. Also, Doetsch et al. (2012b) adopted a similar strategy, in this case using ground-penetrating radar data to provide a priori information about lithologic boundaries, that we assumed to have electrical property contrasts.

It should be underlined that, in all the examples considered so far, we haven't considered what is a satisfactory misfit between the model prediction and the measured data. This will depend on the error level in the measured data, traditionally assessed using repeatability and reciprocity checks, which should be used to define W_d in equation 2.45. Despite measurements of reciprocity provide a better quantification of noise level and are preferred for calculation of weights for inversion, it require double the normal set of measurements, consequently twice the time, and for this reason, despite its significance, several surveys are conducted without such checks. Therefore, many users often fail to recognize the significance of data error in any investigation, even if over-fitting in data inversion can lead to "noisy" images and artifacts. To highlight the importance of the noise level, let's consider again the subsoil structure in Figure 2.41.a and assume that data measured with the Dipole-dipole array has an error level of 5%. Note that, we can easily simulate this by taking the forward model of the subsoil, shown in Figure 2.36, and by perturbing the calculated set of apparent resistivities with an uncorrelated Gaussian noise of 5%. If this is our starting dataset and we realize

the inversion process, assuming three different error values of the data to define W_d, one correct (5%) and two wrong (2% and 10%), the results, as we can see in Figure 2.43, are very interesting.

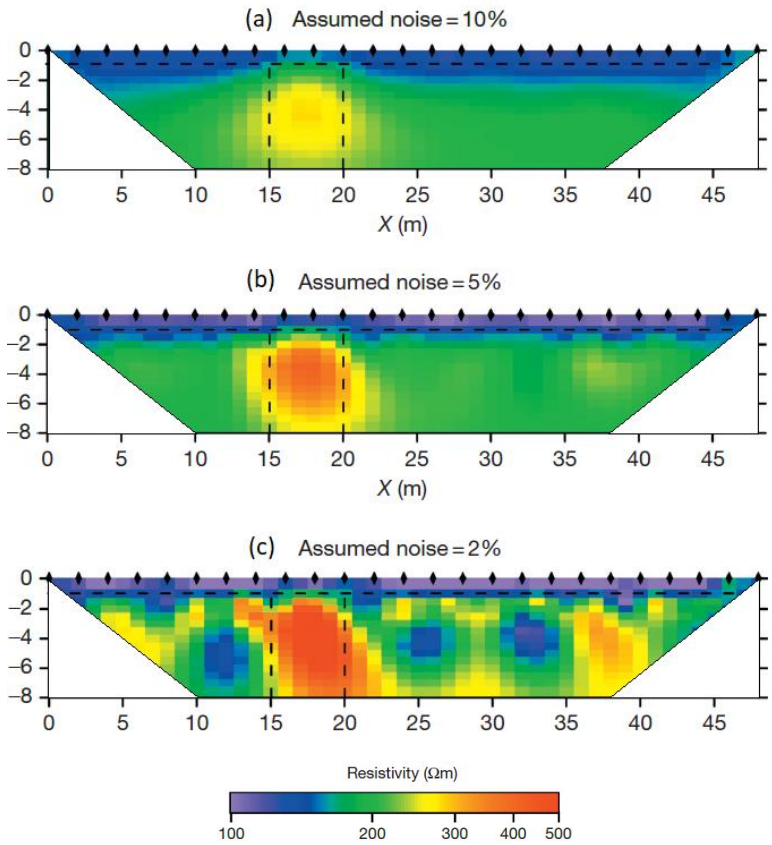

Figure 2.43 Effect of noise on inverted model: (a) 10%, (b) 5% (correct level) and (c) 2%

In Figure 2.43.b is clear that, if we implement the inversion process with the correct noise level (5%), the model is reasonably recovered. Instead, if we underestimate the error level and assume a lower value (2%), then the final model reveals high variability due to the 'overfitting' (Figure 2.43.c). At last, if we use a higher noise level (10%) than the true level (5%), then the model is poor because not all the information in the data is recovered by the inversion. These examples demonstrate the importance of assessing correct error levels and accounting for such error levels in the inversion process. Failure to do so could result in either failure to exploit all the information in the data or incorrect interpretation of the subsurface geoelectrical structure. Note that, in order to estimate the quality of the data as correct as possible, it is necessary to execute as many stacks as possible and, above all, to realize the reciprocity checks. Nevertheless, repeatability and reciprocity checks may not necessarily account for all measurement errors, and as instruments and measurement practice improve, modelling errors may dominate the uncertainty in the final model (Binley, 2015).

3. FORWARD MODELLING

In hydrogeological investigations, the knowledge of the various hydrogeological unit thicknesses is an essential information for the realization of correct numerical models of groundwater flow. In this context, ERT techniques can be applied to extend further into the space punctual information of corings. However, with the ERT surface surveys, it is very complex to precisely define the thickness of the layers. As discussed in chapter 2.2, current lines coming from the surface propagate preferentially in the more conductive layer and this can induce problems defining aquiclude clay layers. Furthermore, as discussed in chapter 2.5, the inversion codes search for the smoothest model (set of parameters) that is consistent with the measured data. Therefore, the sharp resistivity contrasts, such as between a conductive clay layer and the other resistive deposits, will not be represented correctly and the clay layer can result with a much greater thickness than the real one. All this makes difficult the interpretation of the section below the conductive layers, particularly to fix correctly its real thickness. In this chapter, we will deal with this kind of problem and, through the uses of direct models, we will explore the possible strategies to face this situation. Initially, it will be highlighted the effect on ERT surface surveys to insert different thicknesses of conductive clay layers in a subsoil model with greater resistivities. Subsequently, the same subsoil models will be studied with the ERT cross-borehole technique, to verify if this can improve the inversion results. Finally, the ERT technique will be assessed to detect discontinuities of the clay layer due, for instance, to the presence of paleochannels. This is an important issue in environmental investigations as discontinuities of the impermeable clay layer could be preferential infiltration paths for contaminants coming from the surface and which can thus reach the aquifer.

3.1 The Procedure

The following software have been used to carry out the simulations: GMSH (Geuzaine & Remacle, 2013), R2 (Binley, 2019) and Surfer (Golden Software). The first one has been used to create the discretization mesh, with triangular elements, for the various subsoil models investigated. The program allows us to divide the domain into different areas and we can assign to each area a resistivity value with R2. The latter has been used to calculate numerically, with the finite element method and through a direct modelling operation, the apparent resistivities and resistances that would be measured with a defined electrodes configuration, considering the subsoil model that we created. In simple words, the program returns as output the synthetic dataset that would be theoretically measured in the field. These synthetic datasets have been used, again through R2, to realize an inverse modelling process, to switch the apparent resistivities/resistances to new punctual resistivity data. Finally, the resistivity and sensitivity sections, which will be shown in the chapter, have been created with Surfer. To better understand the proceedings, we can consider the subsoil model of Figure 3.1:

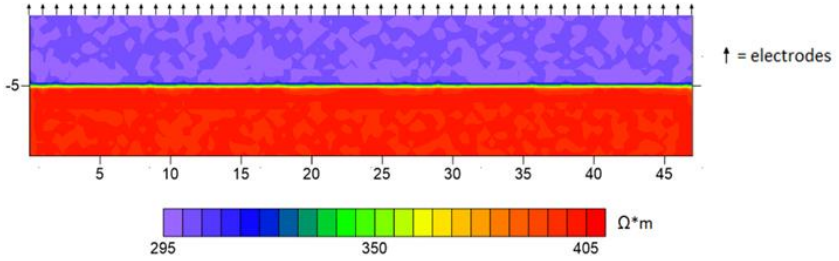

Figure 3.1 Subsoil model and a line of 48 electrodes with 1 m spacing

After creating the discretization mesh with GMSH, we must indicate the elements that make up each layer, in fact this is a necessary input data for the direct modelling procedure performed with R2. Furthermore, the position of each electrode and the acquisition scheme (Dipole-dipole, Wenner, etc.) that we intend to simulate must be provided. Starting from this information, the program can calculate the measurements of apparent resistivity and resistance for each quadripole. If we consider Figure 3.1 and we assume to realize an ERT survey with 48 electrodes, 1 m of spacing and a Wenner configuration, R2 will provide us an output file as shown in Figure 3.2:

```
360
1    2    3    1    4    0.4726780743E+02    296.99239
2    3    4    2    5    0.4775608841E+02    300.06035
3    4    5    3    6    0.4727034176E+02    297.00832
4    5    6    4    7    0.4740666692E+02    297.86487
5    6    7    5    8    0.4737771531E+02    297.68296
6    7    8    6    9    0.4746305374E+02    298.21916
7    8    9    7    10   0.4742908162E+02    298.00571
8    9    10   8    11   0.4744831593E+02    298.12656
9    10   11   9    12   0.4772461324E+02    299.86259
10   11   12   10   13   0.4726594320E+02    296.98068
...
```

Figure 3.2 Output file (incomplete) obtained performing a direct modelling operation with R2 for the subsoil model shown in Figure 3.1

In Figure 3.2 the first line shows the total number of measurements, while, from the second line onwards, the first column represents the measurement number, the next four columns respectively the electrodes M-N-A-B and the last two columns the resistance (Ω) and the apparent resistivity (Ω*m) calculated. Note that, these are the information obtained with an ERT survey performed in the field with a multielectrode instrument. Therefore, it is possible to use this file to simulate an inverse modelling procedure and to obtain back new values of resistivity, distributed punctually within the investigated domain. The procedure can be realized again with R2 and this time the program will provide us an output as shown in Figure 3.3:

```
        x              z              ρ            log(ρ)
0.44139E+02   -0.63533E+01   0.34027E+03   0.25318E+01
0.26214E+02   -0.63587E+01   0.35889E+03   0.25550E+01
0.24599E+02   -0.93760E+01   0.39094E+03   0.25921E+01
0.35790E+01   -0.93657E+01   0.36306E+03   0.25600E+01
0.13399E+02   -0.93720E+01   0.38205E+03   0.25821E+01
0.33595E+02   -0.57223E+01   0.33997E+03   0.25314E+01
0.18405E+02   -0.57223E+01   0.34616E+03   0.25393E+01
0.35905E+02   -0.57223E+01   0.33793E+03   0.25288E+01
0.41716E+02   -0.52013E+01   0.32973E+03   0.25182E+01
0.38240E+02   -0.51897E+01   0.32927E+03   0.25175E+01
0.31260E+02   -0.51897E+01   0.33481E+03   0.25248E+01
0.27784E+02   -0.52013E+01   0.33914E+03   0.25304E+01
0.20740E+02   -0.51897E+01   0.34014E+03   0.25317E+01
...
```

Figure 3.3 Output file (incomplete) obtained performing an inverse modelling procedure with R2 using the input file shown in Figure 3.2

In Figure 3.3, the first two columns are the spatial coordinates of the measurements, and the last two the calculated resistivities. As discussed in chapter 2.5, in addition to this file, the program also returns a file containing information about the sensitivity of each measurement. Therefore, both the files obtained can be used to create resistivity and sensitivity sections, using the software Surfer. In Figure 3.4 we can appreciate the resistivity and sensitivity sections obtained for the dataset shown in Figure 3.3:

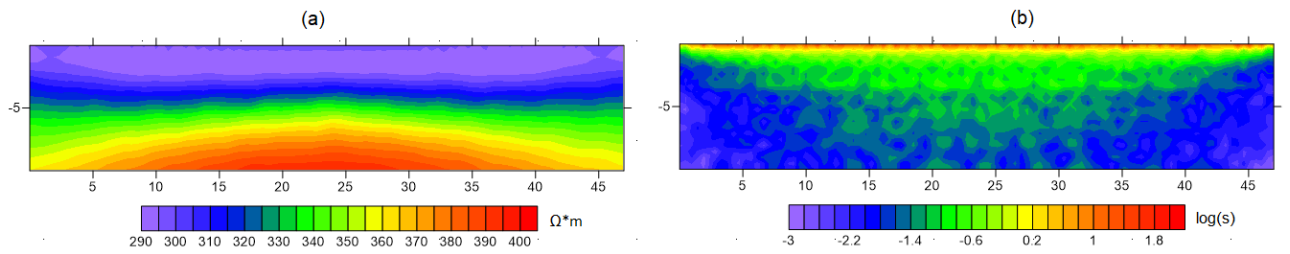

Figure 3.4 (a) Resistivity and (b) sensitivity sections obtained for dataset shown in Figure 3.3

As discussed in chapter 2, Figure 3.4 confirms the high potential of the Wenner configuration to highlight horizontal discontinuities of resistivity in the subsoil. Obviously, the same procedure can also be performed with the Dipole-dipole array. The operation has been done for three different dipole skip: 1 (no skip), 3 and 6. The dipole skip represents the number of electrodes that separate the dipoles of the measurements, for example in Figure 3.5 is shown an input file with a skip of 3:

```
777
1     6     10    1     5
2     7     11    1     5
3     8     12    1     5
4     9     13    1     5
5     10    14    1     5
6     11    15    1     5
7     12    16    1     5
8     13    17    1     5
9     14    18    1     5
10    15    19    1     5
...
```

Figure 3.5 Example of measurement input file for Dipole-dipole configuration with skip 3

In Figure 3.5, the first line represents the total number of measurements while, from the second row onwards, the first column is the number of the measurement, the second and third columns are the electrodes M-N and the last two columns are the electrodes A-B. Lower is the skip and higher is the resolution of the investigation but lower is the penetration. To confirm this, we can check Figure 3.6, which contains the resistivity and sensitivity sections obtained for the subsoil model in Figure 3.1, using at first a skip of 1 (Figure 3.6a/b) and afterward a skip of 6 (Figure 3.6.c/d):

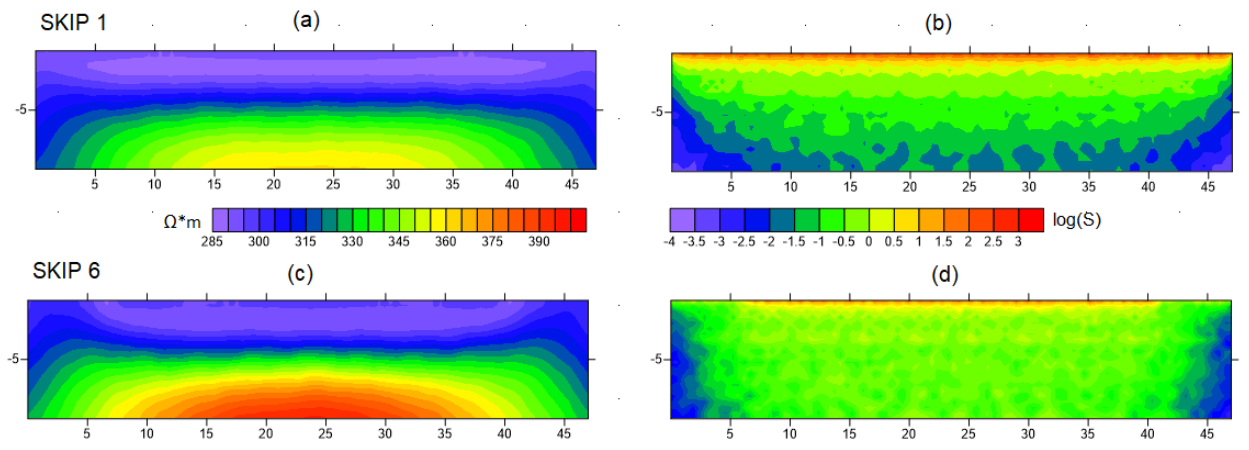

Figure 3.6 (a) Resistivity and (b) sensitivity sections obtained with a Dipole-dipole configuration skip 1 for the subsoil model and electrodes line shown in Figure 3.1. (c) Resistivity and (d) sensitivity section obtained using a skip of 6

In Figure 3.6.a. is clear that, with this type of electrodes configuration, the measurements performed with a skip of 1 do not guarantee sufficient penetration to measure accurately the resistivity of the second resistive layer (400 Ω*m), as demonstrated also by the sensitivity section of the Figure 3.6.c. Instead, by increasing the skip number to 6, the investigation ensures greater penetration (Figure 3.6.d) which allows us to define the resistivity of the second layer in a more correct way (Figure 3.6.b).

3.2 Presence of a Continuous Clay Layer

3.2.1 Surface-Based Imaging

If a conductive layer of clay (20 Ω*m) of approximately 2 meters thick is added to the subsoil model of Figure 3.1 about 5 m deep, we will obtain different result using the same procedure seen in chapter 3.1. Figures 3.7 shows the resistivity and sensitivity sections, as before considering a line of 48 electrodes with 1 meter spacing, obtained for the subsoil model of Figure 3.7.a:

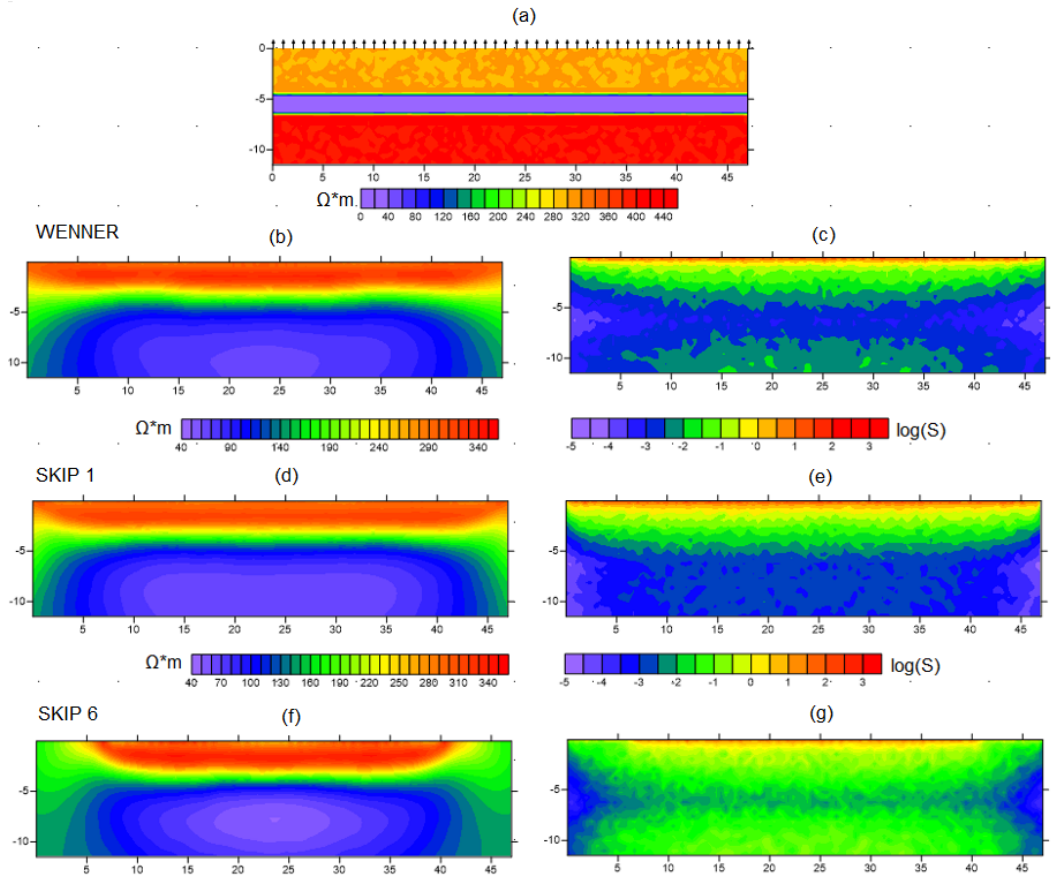

Figure 3.7 (a) Subsoil model, (b) resistivity and (c) sensitivity sections obtained with Wenner array. (d) Resistivity and (e) sensitivity section obtained with Dipole-dipole array skip 1. (f) Resistivity and (g) sensitivity sections obtained with skip 6

By comparing the resistivity sections of the model without the clay layer (Figure 3.4/6) and those with the clay layer (Figure 3.7), it is clear the effect that the latter shows: the deeper resistive layer is not detected in the resistivity sections because the thickness of the clay layer seems to be much greater than the real one. To be noted, all that even if the spacing of the electrodes, which determines the resolution (as we seen in chapter 2.2), is less than the thickness of the clay layer. Furthermore, in Figure 3.8 we can appreciate that, even if the thickness of the clay layer is halved

(Figure 3.8.a) the problem remains and the deeper resistive layer is still not resolved. However, if the clay layer has decreased to a few decimetres (Figure 3.8.h), using the Dipole-dipole array with a skip of 6 (Figure 3.8.l), the deeper resistive layer become partially visible in the resistivity section (Figure 3.8.m) even though it is still impossible to correctly define the real thickness of the clay layer.

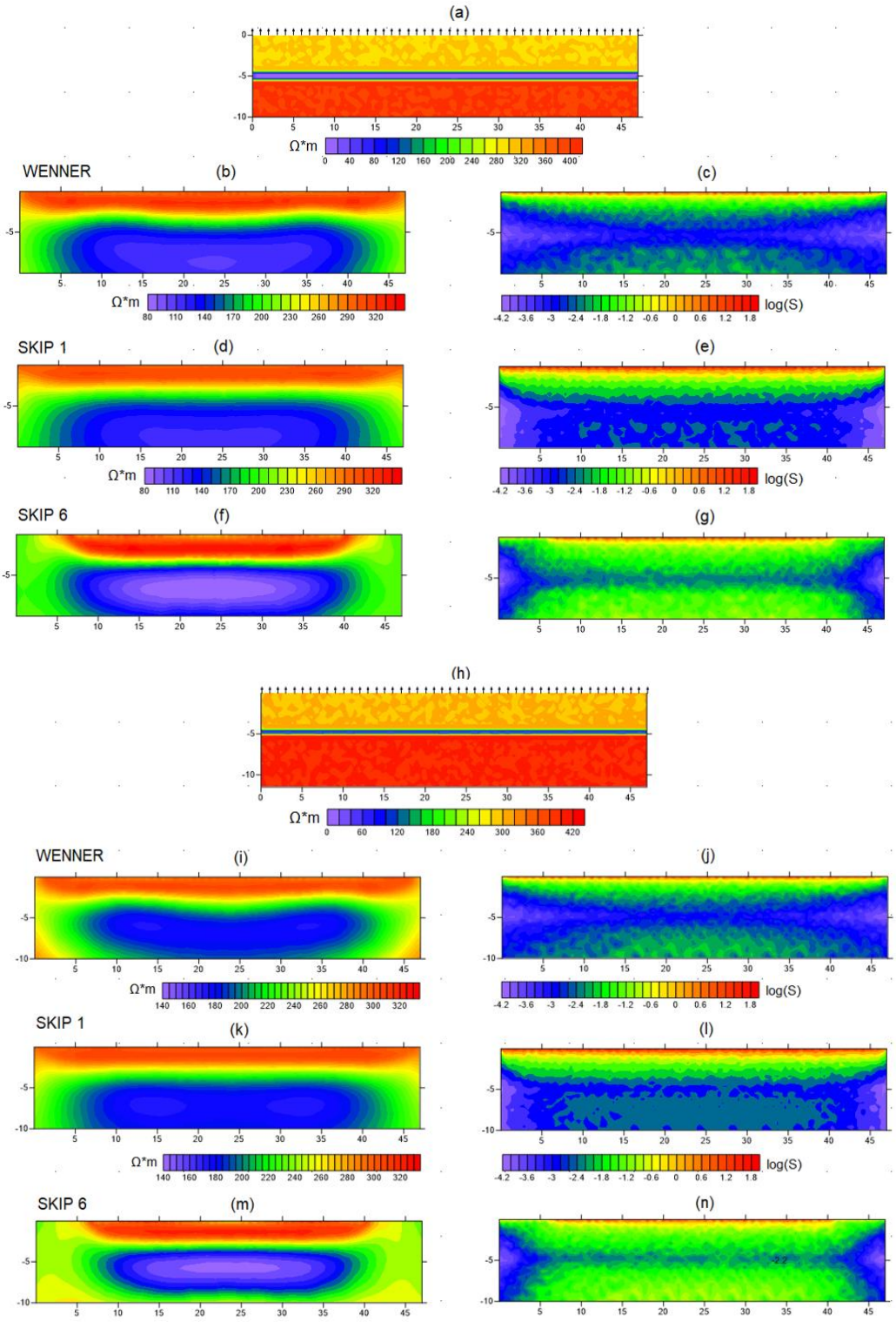

Figure 3.8 (a) Subsoil model with 0.8 m clay layer, (b) resistivity and (c) sensitivity sections obtained with Wenner array, (d) resistivity and (e) sensitivity section obtained with Dipole-dipole array skip 1, (f) resistivity and (g) sensitivity sections with Dipole-dipole array skip 6. (h) Subsoil model with 0,4 m clay layer, (i) resistivity and (j) sensitivity sections obtained with Wenner array, (k) resistivity and (l) sensitivity section with Dipole-dipole array skip 1, (m) resistivity and (n) sensitivity sections obtained with skip 6

Practically speaking, in Figures 3.7/8 we can see the consequences of the short-circuit phenomenon and the excessive smoothing performed by the inversion code: the thickness of the clay layer seems to be much greater than the real one and the deeper resistive layer is hidden. The Wenner and Dipole-dipole low skip arrays are more susceptible to this problem, while using a Dipole-dipole configuration with higher skip the situation seems slightly to improve (Figure 3.8.m), even though the real thickness of the clay layer remains always indefinable. However, it can be noted that by increasing the number of skips the investigation is deeper but also seems to be shrunk laterally. In fact, if we focus on the resistivity section of Figure 3.8.m is clear that the first resistive layer (300 Ω*m) does not develop laterally over the whole section, but only between 5 and 40 meters. A solution to overcome this problem is to use, in the same survey, several skips. This will ensure greater sensitivity at the ends of the line as well as high penetration. Obviously, this will make the acquisition time much longer, also considering that it is always advisable to get reciprocal measurement. An example of what has just been discussed is shown in Figure 3.9, for the subsoil model of Figure 3.8.h, the measurements have been realized with different skips together: 1, 3 and 6. The number of measurements using only a skip of 6 is 561 (without counting the reciprocal measures), while using three different skip together the number of measurements has become 2376 (without counting the reciprocal measures). However, it should be noted that the first resistive layer is clearly visible over the whole section and the high penetration is still guaranteed.

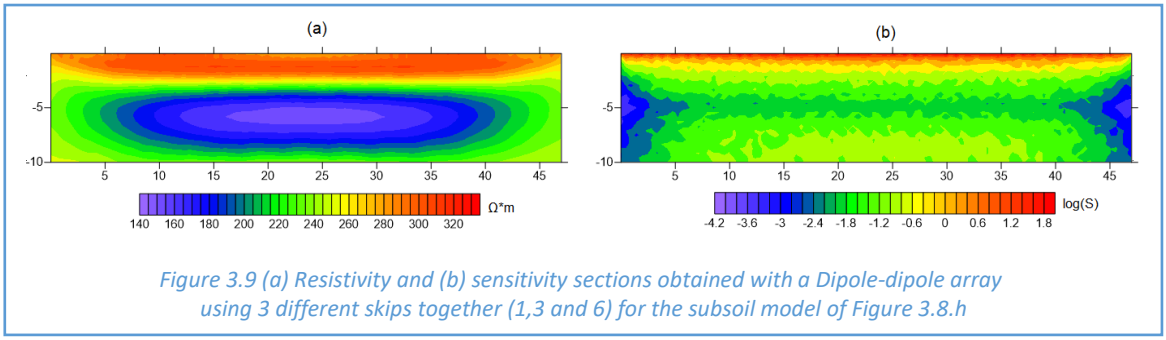

Figure 3.9 (a) Resistivity and (b) sensitivity sections obtained with a Dipole-dipole array using 3 different skips together (1,3 and 6) for the subsoil model of Figure 3.8.h

Note that, up to this point the various subsoil models have been investigated only considering a line of 48 electrodes with a spacing of 1 meter. Therefore, now we can consider the effects detected by changing the length of the electrodes line or/and the spacing, to check if it is possible to improve the quality of the resistivity section, considering the subsoil model of Figure 3.8.a (thickness of the clay layer slightly less than 1 meter). At first, we defined a new line of 48 meters but with 25 electrodes spaced 2 meters from each other, as shown in Figure 3.10.a:

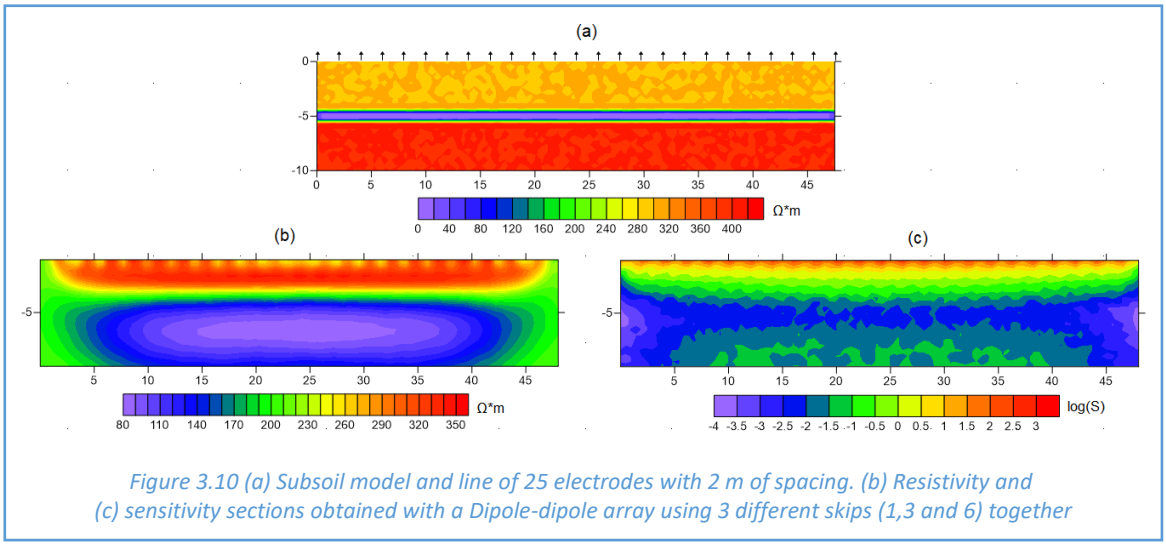

Figure 3.10 (a) Subsoil model and line of 25 electrodes with 2 m of spacing. (b) Resistivity and (c) sensitivity sections obtained with a Dipole-dipole array using 3 different skips (1,3 and 6) together

From Figure 3.10.b is clear that by keeping to use a 48-meter line but with an electrode spacing of 2 meters, the deeper resistive layer is still not visible in the resistivity section and the clay layer appears with a much greater thickness than the real one, even using a skip of 6. As we can see in Figure 3.11, the problem still exists even using 96 electrodes spaced 0.5 meters from each other.

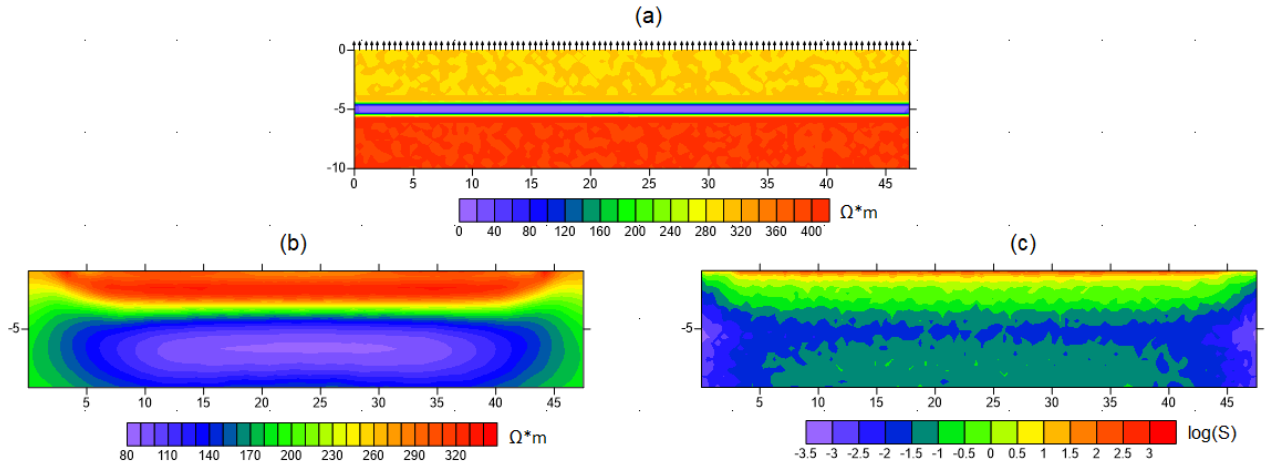

Figure 3.11 (a) Subsoil model and line of 96 electrodes with 0.5 m of spacing.
(b) Resistivity and (c) sensitivity sections obtained with a Dipole-dipole array skip 6

Apparently, regardless of spacing, if we use a 48-meters line of electrodes, the clay layer at about 5 meters deep does not allow us to reach a correct interpretation of the resistivity section. If we increase the length of the electrodes line the investigation depth obviously increases. Figure 3.12 shows the resistivity and sensitivity sections obtained using a 70-meters line of electrodes, spaced 1.5 meters (Figure 3.12.a) and 0.75 meters (Figure 3.12.b) using a Dipole-dipole array skip 1.

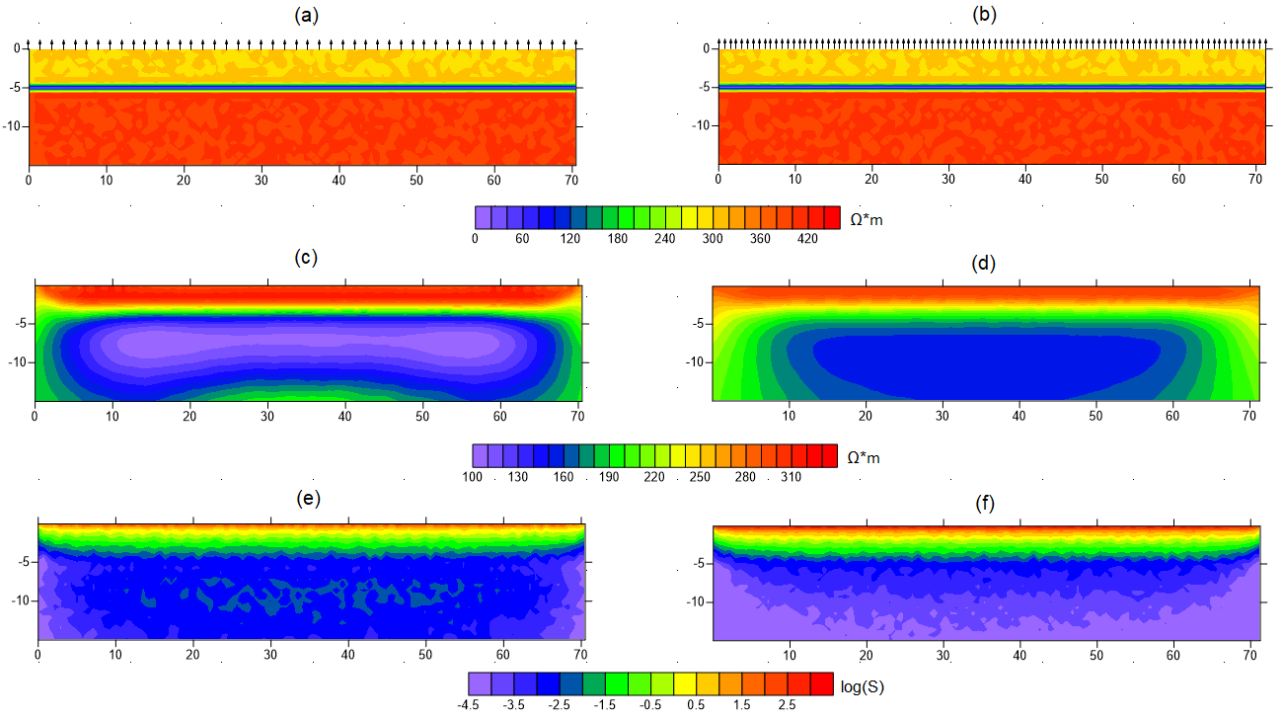

Figure 3.12 Subsoil model with 70-meters line of (a) 48 electrodes (1.5 m spacing) and (b) 96 electrodes (0.75 m spacing).
(c) Resistivity and (e) sensitivity sections obtained with a Dipole-dipole array skip 1 for subsoil model and electrodes line (a).
(d) Resistivity and (f) sensitivity sections obtained with a Dipole-dipole array skip 1 for subsoil model and electrodes line (b)

From Figure 3.12 we can appreciate that, even increasing the length of the electrodes line, the Dipole-dipole array with skip 1 (no skip) does not guarantee enough penetration to detect the deeper resistive layer. Furthermore, by comparing the two resistivity sections (Figure 3.12.c/d), it seems that, using a configuration with no skip and a minor spacing of the electrodes, we still have the problems previously observed. In fact, the sensitivity section of the line with less spacing (Figure 3.12.f) shows a much lower value in-depth than that with greater spacing (Figure 3.12.e). Instead, the Dipole-dipole array with skip 6, regardless of the spacing, guarantees enough penetration (check Figure 3.13.c/d) to detect the deeper resistive layer but, as shown in Figure 3.13.a/b, it is not possible to correctly define the thickness of the conductive clay layer and thus the deeper resistive layer's boundaries.

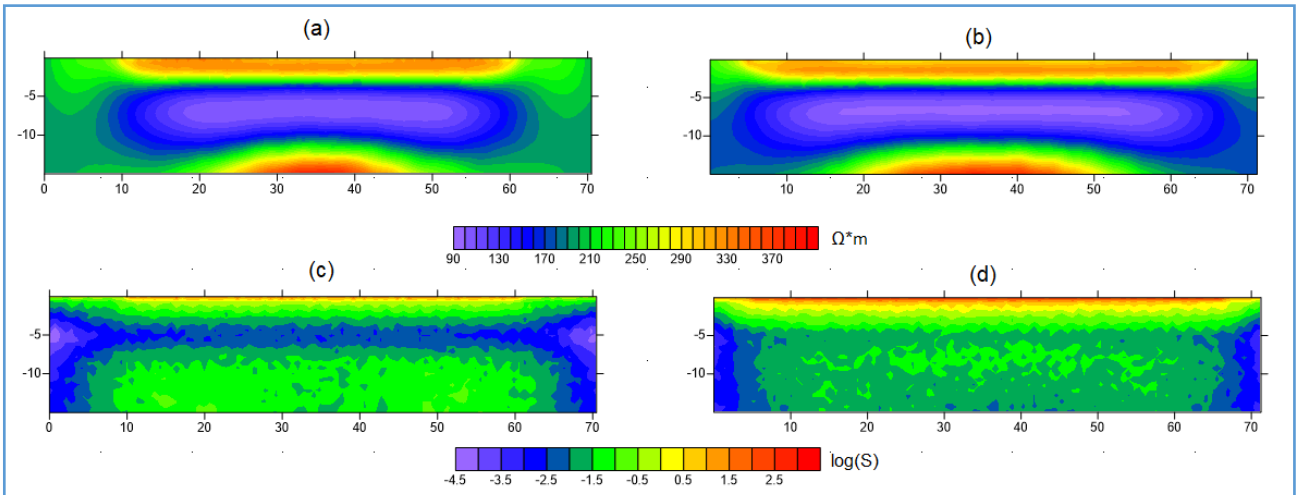

Figure 3.13 (a) Resistivity and (c) sensitivity sections for subsoil model and electrodes line in Figure 3.12.a obtained with Dipole-dipole array with skip 6. (b) Resistivity and (d) sensitivity sections for subsoil model and electrode line in Figure 3.12.b obtained with Dipole-dipole array with skip 6

As early discussed, larger skip tends to shrink laterally the validity of the resistivity section but, if we compare Figures 3.12.a/b, is clear that the phenomenon is reduced in the section of the electrodes line with less spacing. Instead, the Wenner array, regardless of the spacing, does not guarantee a better result than that obtained with the Dipole-dipole skip 6. In fact, if we check Figure 3.14, it is evident that, although we can presume the presence of the deeper resistive layer, the thickness of the clay layer seems to be even more emphasized than in the sections of Figure 3.13.a/b. Note that, there is not a substantial difference using 1.5 m spacing (Figure 3.14.a/c) or 0.75 m (Figure 3.14.b/d).

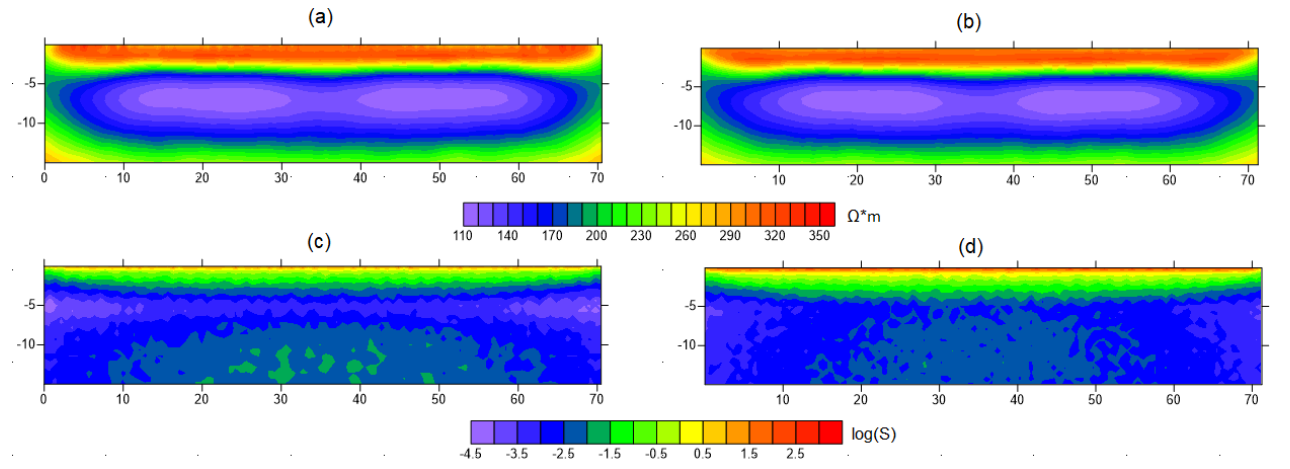

Figur3.14 (a) Resistivity and (c) sensitivity section for subsoil model and electrodes line in Figure 3.12.a obtained with Wenner array. (b) Resistivity and (d) sensitivity sections for subsoil model and electrode line in Figure 3.12.b obtained with Wenner array

If we increase the length of the electrodes line to 94 meters, the investigation deepens but the problems in the resistivity sections are not overcome. As we can see in Figure 3.15.c, in the resistivity section obtained with a Dipole-dipole array skip 1 and 2-meter spacing of the electrodes (Figure 3.15.a), the deeper resistive layer is clearly visible but its roof seems to be at a much greater depth than the real one, due to the apparent much greater thickness of the clay layer. On the other hand, by using a 96-electrodes line with 1 m of spacing (Figure 3.15.b), skip 1 does not guarantee enough penetration to detect the deeper resistive layer and the thickness of the clay layer seems to be even greater (Figure 3.15.d). This seems to confirm the assumption introduced previously, according to which a minor spacing of the electrodes seems to be more problematic for this kind of investigations if we use a no skip configuration. In fact, the same results have been obtained also with models where the clay layer has a thickness of 0.5 m and 2 m (not reported in the thesis).

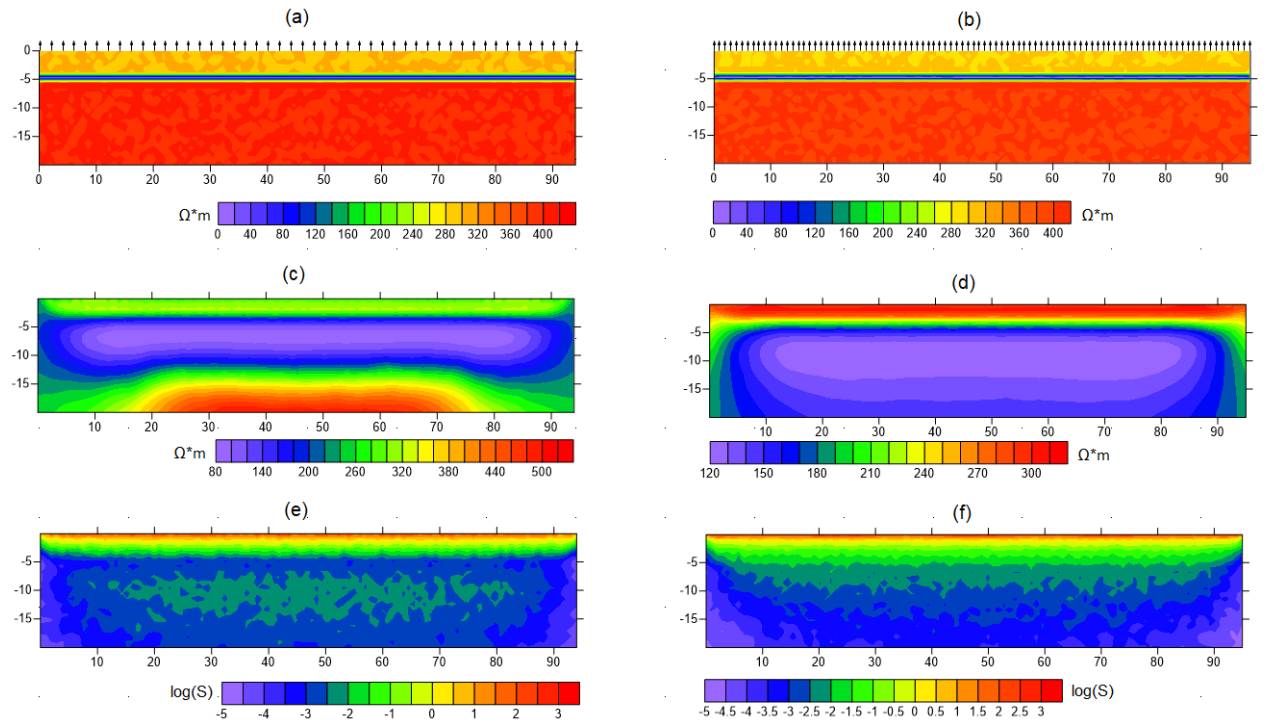

Figure 3.15 Subsoil model with 94-meters line of (a) 48 electrodes (2 m spacing) and (b) 96 electrodes (1 m spacing). (c) Resistivity and (e) sensitivity sections obtained with a Dipole-dipole array skip 1 for subsoil model and electrodes line (a). (d) Resistivity and (f) sensitivity sections obtained with a Dipole-dipole array skip 1 for subsoil model and electrodes line (b)

Also with the Wenner configuration it is possible to appreciate the deeper resistive layer, this time regardless of the spacing of the electrodes, but the thickness of the clay layer is still indefinable and the deeper resistive layer's roof depth is much greater than the real one. In Figure 3.16 are shown the resistivity and sensitivity sections obtained with the Wenner array using the 96-electrodes line with 1 m spacing (practically the same sections as those obtained with the 48-electrodes line):

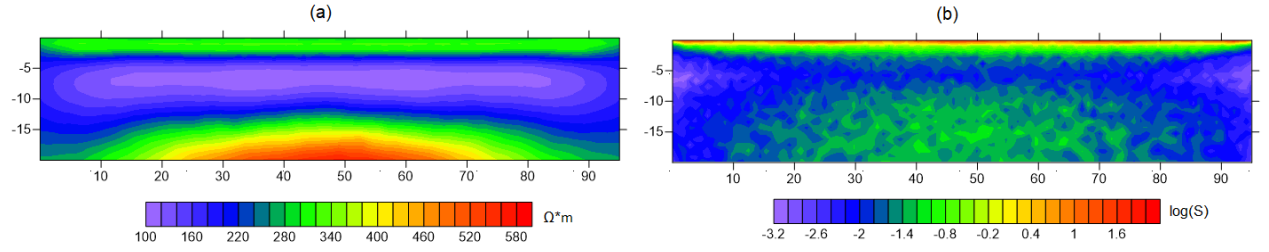

Figure 3.16 (a) Resistivity and (b) sensitivity sections obtained with Wenner array for subsoil model of Figure 3.15.b

Increasing the skip number of the Dipole-dipole array does not improve much the quality of the resistivity section. As we can see in Figure 3.18, regardless of the spacing of the electrodes, even if we use a higher skip of 3 or 6, the thickness of the clay layer still seems to be much greater than the real one and consequently, the deeper resistive layer's roof depth still appear at a greater depth.

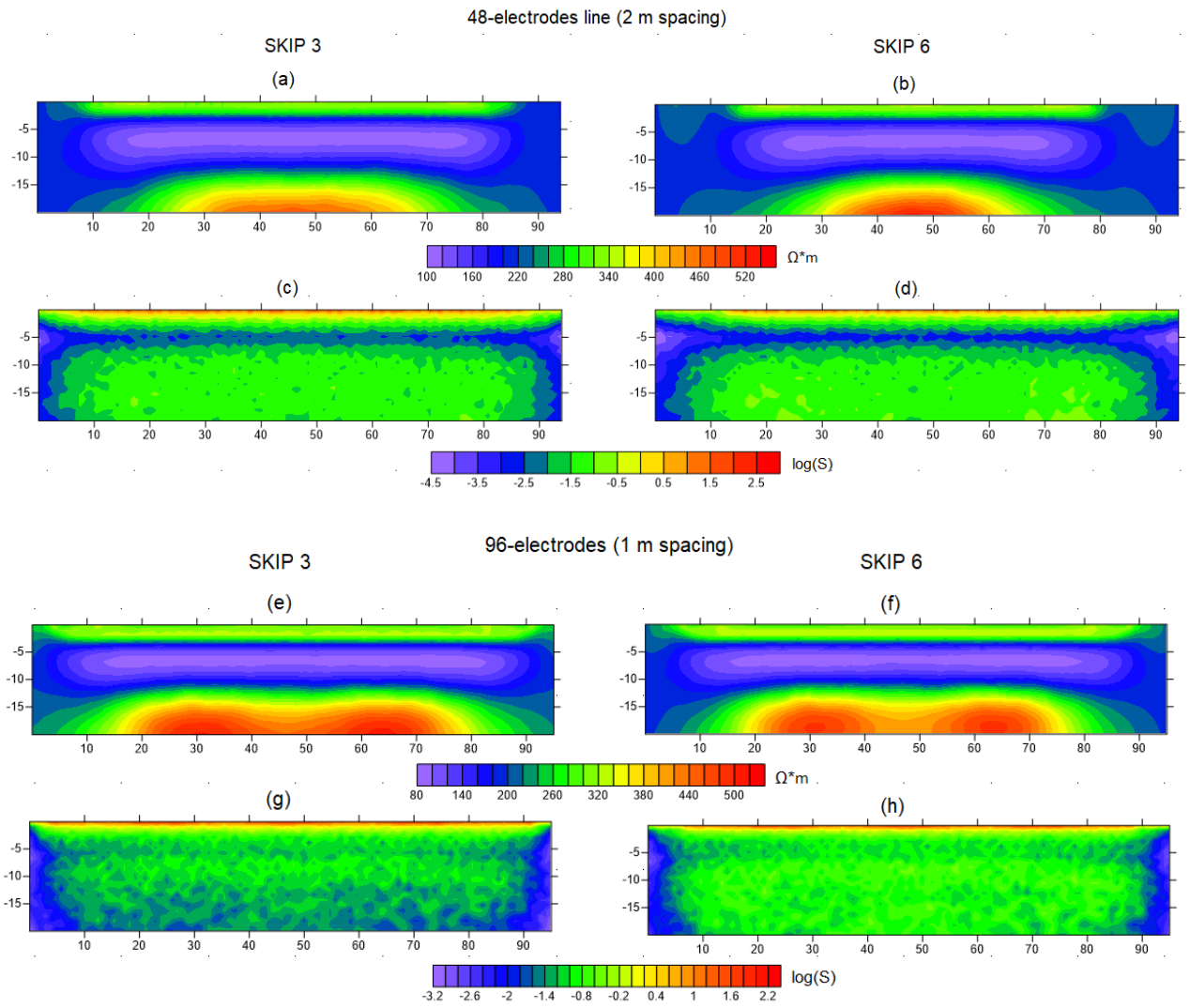

Figure 3.18 (a) Resistivity and (c) sensitivity sections for subsoil model in Figure 3.15.a using Dipole-dipole array skip 3. (b) Resistivity and (d) sensitivity sections for subsoil model in Figure 3.15.a using Dipole-dipole array skip 6. (e) Resistivity and (g) sensitivity sections for subsoil model in Figure 3.15.b using Dipole-dipole array skip 3. (f) Resistivity and (h) sensitivity sections for subsoil model in Figure 3.15.b using Dipole-dipole array skip 6

Therefore, at this point is clear that the problems of short-circuit and excessive smoothing performed by the inversion code can develop independently of the electrodes line's length and spacing. Despite this, increasing the length of the electrode line and/or the number of skips allows us to deepen the investigation and to see the third layer in the resistivity section, even if its top seems to be at a much greater depth than the real one. Note that, all the latest simulations have been performed using the same subsoil model with a clay layer of few decimeters thick. The same operations have been also achieved using a clay layer which thickness is 3 times greater (about 2 meters) and the results obtained are very similar to those shown so far. This further complicates the problems seen in this chapter, in fact with an ERT surface investigation we are not able to define the clay layer thickness correctly. To confirm the latter concept we can check Figure 3.19, which shows the comparisons between the resistivity sections obtained for two different subsoil model,

one with a clay layer of few decimeters thick while the other about 2 meters, always considering the same electrodes line and a Dipole-dipole array with three different skip (1, 3 and 6) together.

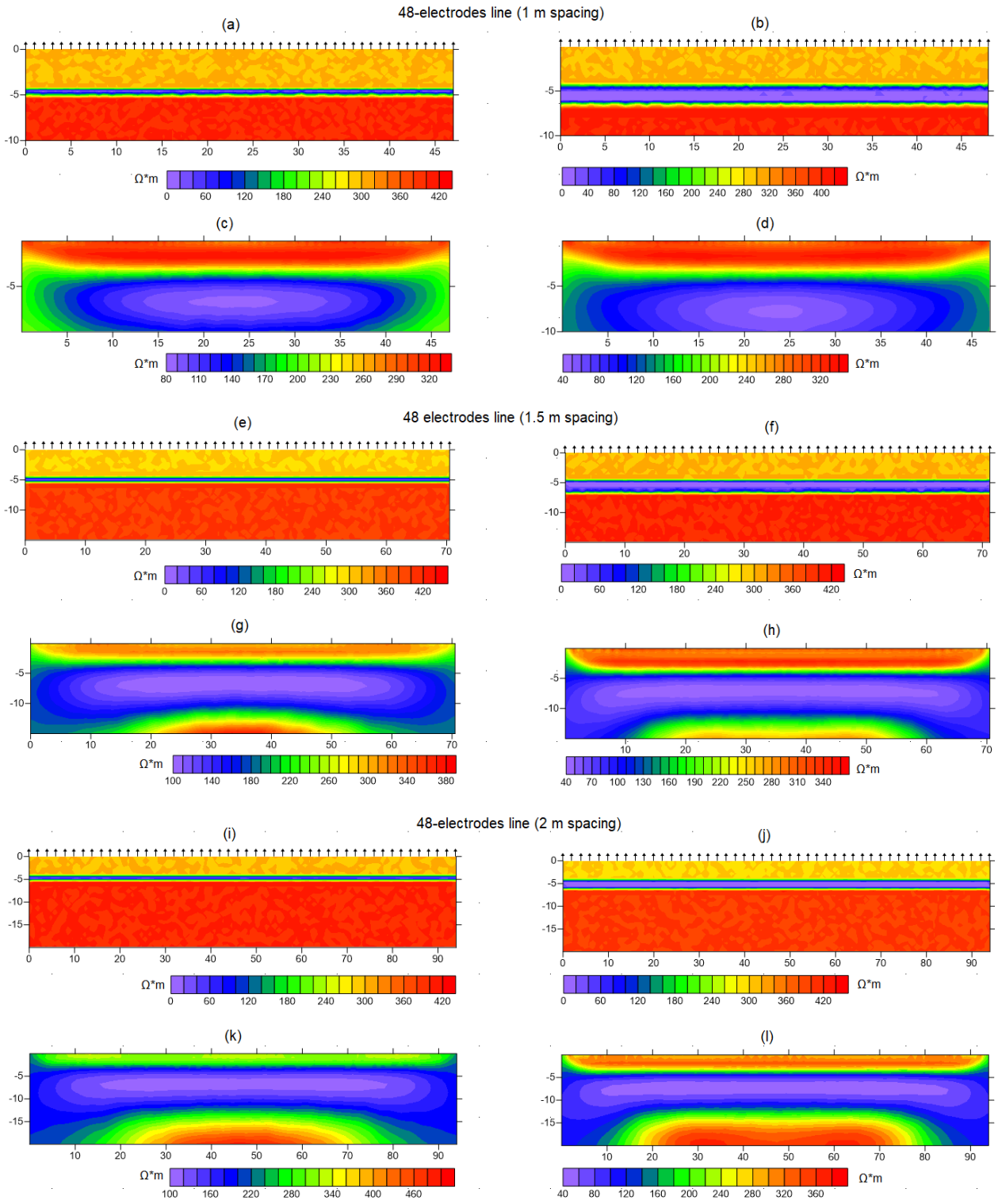

Figure 3.19 (a, b) Subsoil models and 48-electrodes line 1 meter spaced. (c, d) Resistivity sections obtained for (a, b) using a Dipole-dipole array skip 1,3 and 6 together. (e, f) Subsoil models and 48-electrodes line 1.5 meter spaced. (g, h) Resistivity sections obtained for (e, f) using a Dipole-dipole array skip 1,3 and 6 together. (i, j) Subsoil models and 48-electrodes line 2 meter spaced. (k, l) Resistivity sections obtained for (i, j) using a Dipole-dipole array skip 1,3 and 6 together

From Figure 3.19 is clear that the resistivity sections obtained with the two models are very similar to each other. This implies that, if the thickness of the conductive clay layer is not known a priori, it is practically impossible to define its real thickness only from the resistivity sections. The same comparison procedure has been also realized with lines of 96 electrodes with variable spacing (0.5, 0.75 and 1 m) and even in this case all the resistivity sections obtained for the two subsoil models, with any configuration (Wenner and Dipole-dipole), are very similar to each other. For example, in Figure 3.20 is shown the comparison between the resistivity sections obtained for the two models using a Dipole-dipole array skip 6:

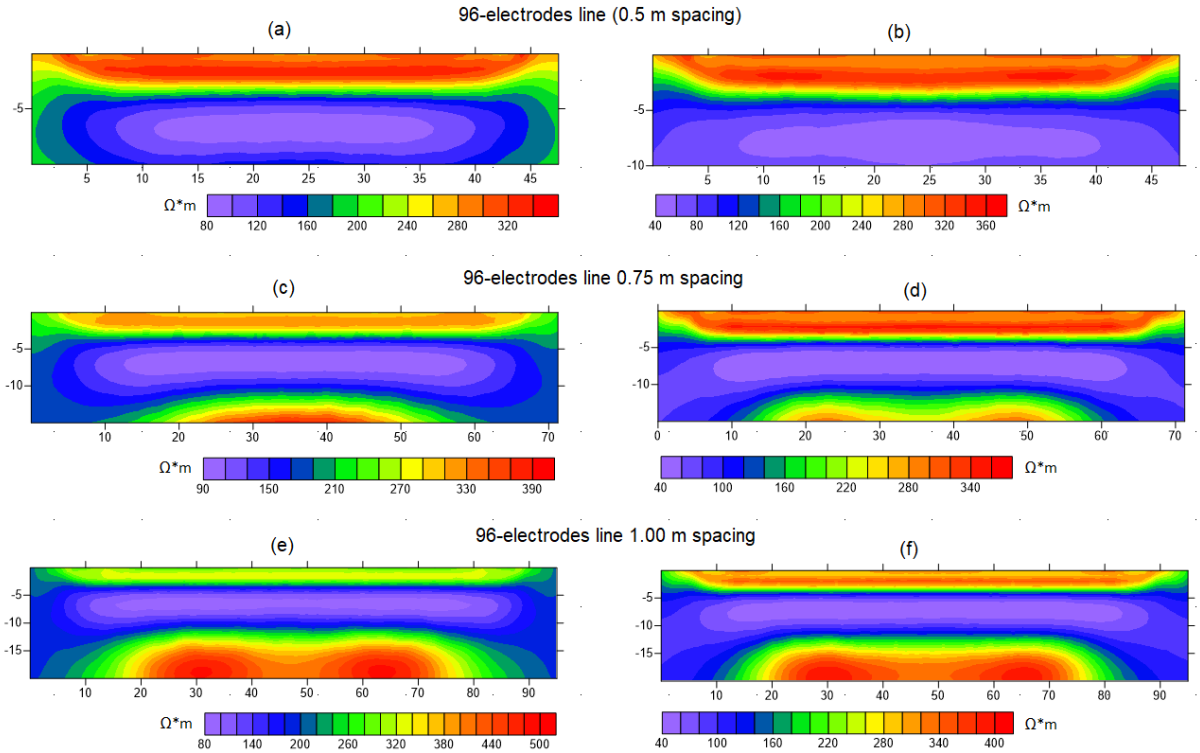

Figure 3.20 (a) Resistivity section obtained for subsoil model in Figure 3.19.a. (b) Resistivity section obtained for subsoil model in Figure 3.19.b. (c) Resistivity section obtained for subsoil model in Figure 3.19.e. (d) Resistivity section obtained for subsoil model in Figure 3.19.f. (e) Resistivity section obtained for subsoil model in Figure 3.19.i. (f) Resistivity section obtained for subsoil model in Figure 3.19.j. Using 96-electrodes line and Dipole-dipole array skip 6 for each case

Furthermore, we must emphasize that by increasing the depth of the clay layer, the investigation is even more complicated. In fact, to be able to see the deeper layer in the resistivity section, it will be necessary to use longer electrodes lines and/or higher skips than those used in the examples discussed in this chapter. For instance, if we double the depth of the clay layer, as shown in Figure 3.21, from the resistivity sections obtained using a 48-electrodes line of 96 meters and a skip of 6 (Figure 3.22), it is clear that it is not possible to define the deeper resistive layer. To do this, it will be necessary to lengthen the electrode line or further increase the skip number.

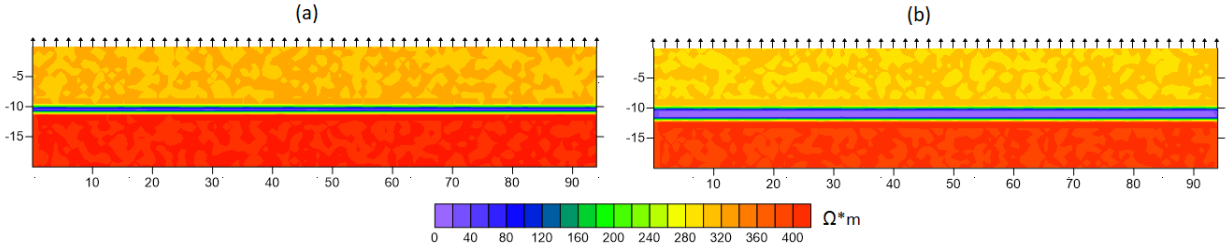

Figure 3.21 Subsoil models with clay layer of (a) a few decimeters and (b) about 2 meters; 48-electrodes line (2 m spacing)

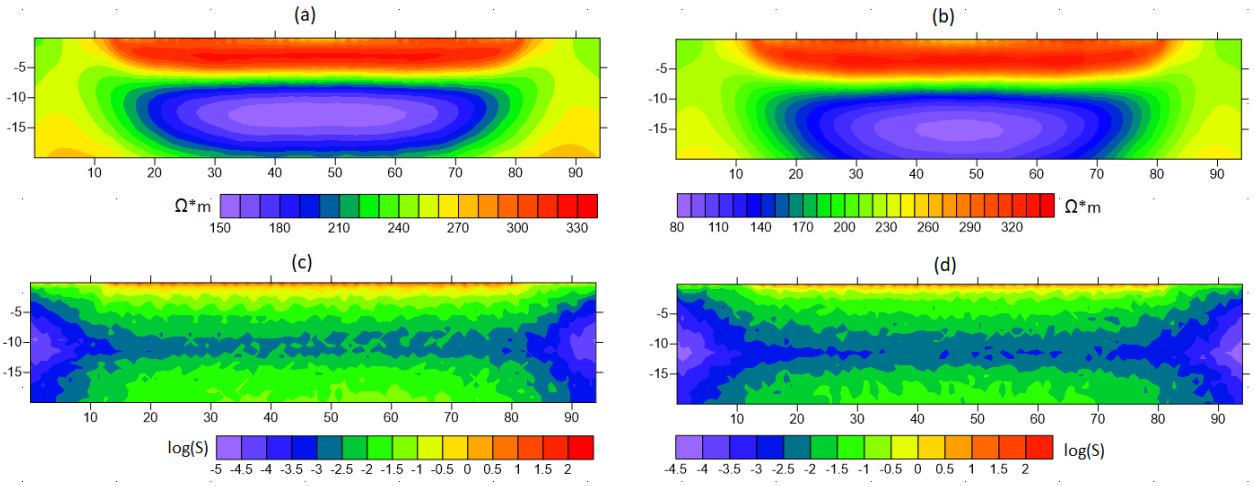

Figure 3.22 (a) Resistivity and (c) sensitivity sections for subsoil model in Figure 3.21.a.
(b) Resistivity and (d) sensitivity sections for subsoil model in Figure 3.21.b

Finally, we must specify that all the resistivity sections in this chapter have been realized using a normal isotropic regularisation. In fact, even if we achieve the inverse processing with an enhanced horizontal smoothing, the resistivity sections that we obtain still show all the problems seen in this chapter. For instance, we can see Figure 3.23 where is shown the comparison between the resistivity sections obtained, for the subsoil model of Figure 3.15.b, using a regular smoothing (Figure 3.23.a) and an enhanced horizontal smoothing (Figure 3.23.b).

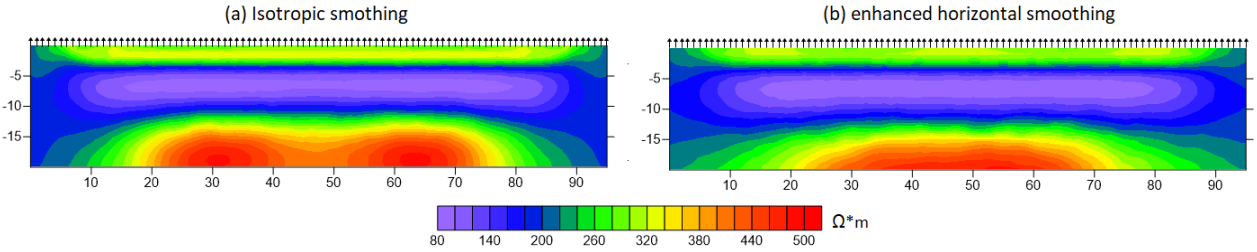

Figure 3.23 (a) Resistivity section obtained for the subsoil model in Figure 3.15.b using a normal isotropic regularisation.
(b) Resistivity section obtained for the subsoil model in Figure 3.15.b using an enhanced horizontal smoothing. Both with skip 6

To conclude, from the analysis carried out in this chapter is clear that, with a subsoil model containing a conductive layer (natural as clay or even anthropic), ERT surface surveys do not guarantee a high capacity to define the real structure of the subsoil. In fact, below the clay layer the interpretation of the resistivity section is very complicated since the thickness of the conductive layer seems to be much greater than the real one. For the same length of the electrodes line, we have seen that the problem is mostly emphasized by using a low skip number (Dipole-dipole array) and, despite its high vertical sensitivity, by the Wenner configuration. Furthermore, as the depth of the clay layer increases, the situation becomes even more complicated. In fact, it will be necessary to use higher skip number and/or longer electrode lines to be able to define the layers below the conductive one but, as we discussed in chapter 2.4, the number of electrodes that a multielectrode instrument can control is limited and the investigation sites often do not allow to realize very long electrodes line. Finally, although the thicknesses of the conductive clay layer can be very different, the resistivity sections are highly similar to each other, making the interpretation of this kind of subsoils even more complicated.

3.2.2 Cross Borehole Based Imaging

In this chapter we will explore the potentiality of ERT cross borehole surveys applied to the study of subsoil structures with conductive layers, such as those described in the previous chapter. We will analyze the consequences of placing a conductive layer between two more resistive layers, considering different electrodes spacing and distances between holes. In all the surveys an AB-MN configuration, as shown in Figure 3.24, has been simulated.

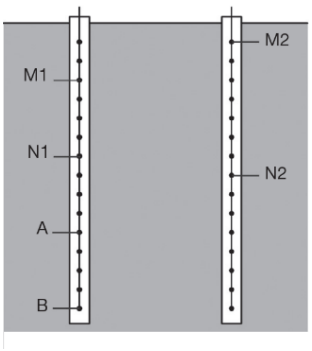

Figure 3.24 AB-MN cross borehole configurations

At first, we can consider a layer with 300 Ω*m of resistivity superimposed to another with 400 Ω*m. In Figure 3.25 is shown the subsoil model with three different cross borehole configurations and the relative resistivity sections obtained using an AB-MN acquisition scheme with skip 1:

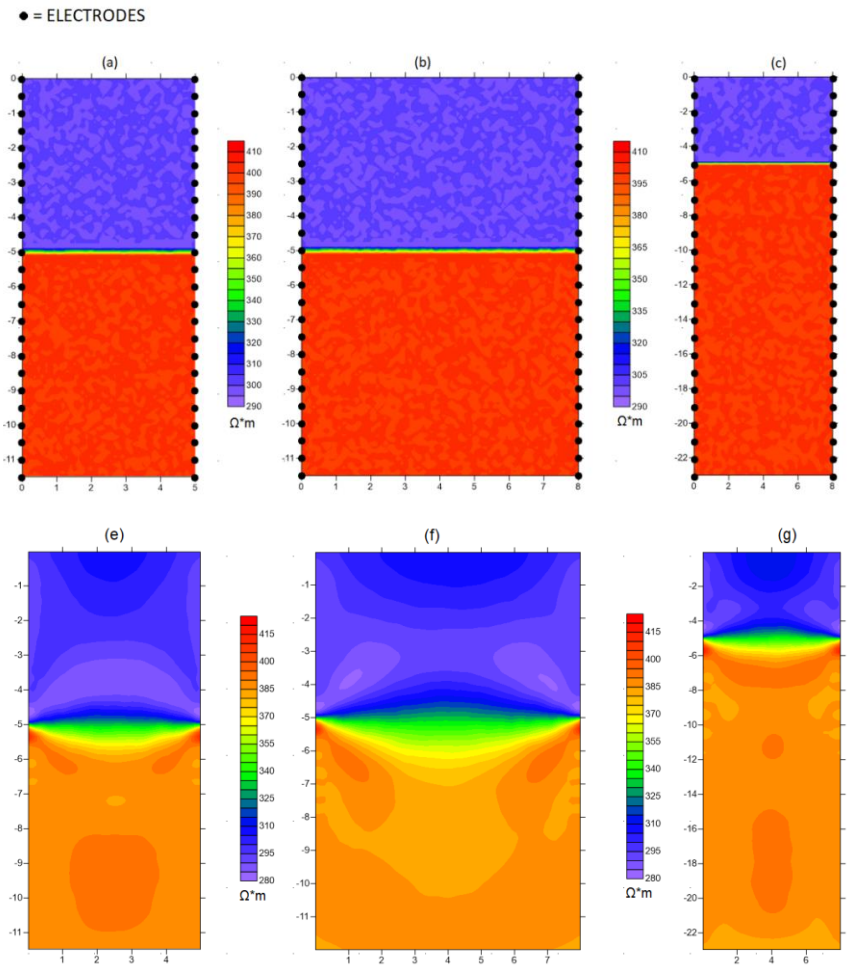

Figure 3.25 (a, b, c) Subsoil model; (a) electrodes spaced 0.5 m and holes 5 m; (b) electrodes spaced 0.5 m and holes 8 m; (c) electrodes spaced 1 m and holes 8 m. (e, f, g) Resistivity sections obtained for (a, b, c)

From the resistivity sections of Figure 3.25 we can appreciate that, with the ERT cross borehole technique, we are able to define more precisely the second layer's top depth respect to the resistivity sections obtained from the surface (Figure 3.4.a and Figure 3.6.a/c). This is due to the fact that the sensitivity of the ERT investigation is maximum near the electrodes, which in this case are inserted in the subsoil and therefore in direct contact with the discontinuity. As we can see in the sensitivity sections of Figure 3.26, the sensitivity decreases moving away from the electrodes and is minimal at half the distance between the two holes. As discussed in chapter 2.2, the distance between the two holes should not be greater than half the length of the line of electrodes in a hole. In fact, from figure 3.26.b is evident that, in the section obtained with the two holes separated 8 m from each other and with electrodes spaced 0.5 m (the length of electrodes line in each hole is 11.5 m), the sensitivity at half the distance between the two holes is much lower than that of the section obtained with holes separated 8 m from each other but with electrodes spaced 1 m (the length of electrodes line in each hole is 23 m – Figure 3.26.c) or that obtained with holes separated 5 m from each other and with electrodes spaced still 0.5 m (Figure 3.26.a).

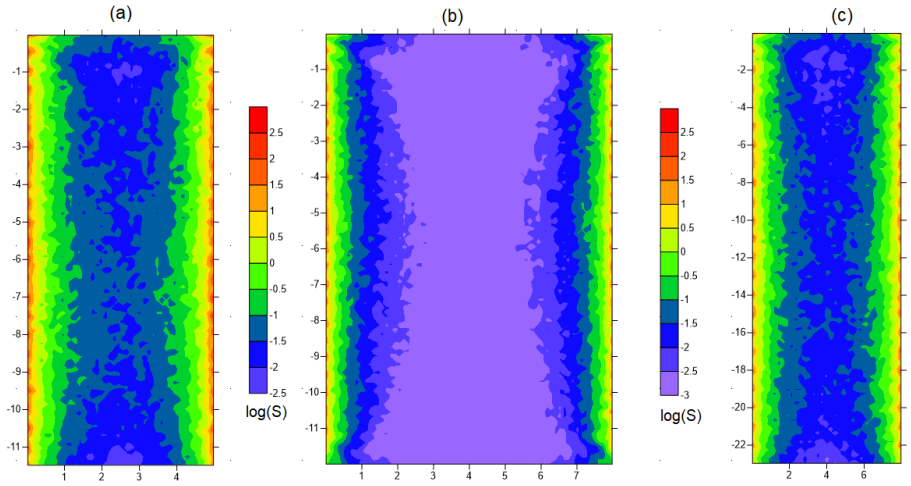

Figure 3.26 (a, b, c) Sensitivity of resistivity sections in Figure 3.25.e/f/g

By placing a conductive clay layer of a few decimeters in this subsoil model (Figure 3.27), as done in the previous chapter, and simulating again the cross-borehole surveys (AB-MN skip 1), we obtained very interesting results that can help to overcome the problems found in the surface investigations.

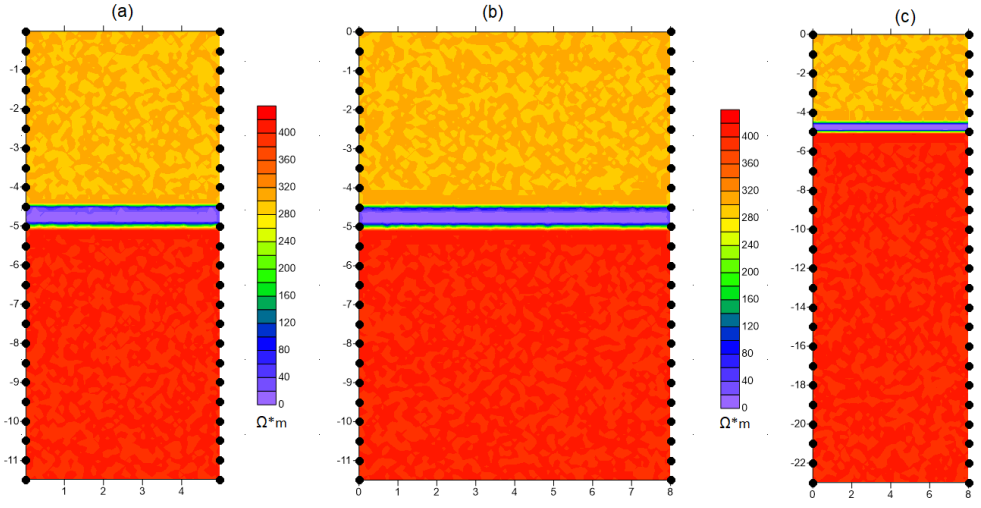

Figure 3.27 (a, b, c) Subsoil model; (a) electrodes spaced 0.5 m and holes separated 5 m; (b) electrodes spaced 0.5 m and holes 8 m; (c) electrodes spaced 1 m and holes separated 8 m

As we can see in Figure 3.28, the conductive clay layer and its thickness can be clearly defined from the resistivity sections, also by using an electrode spacing greater than the thickness of the clay layer itself (Figure 3.28.c). Furthermore, as we can appreciate from the sensitivity sections (Figure 3.28.e/f/g), the values along the conductive layer are maximum and this guarantees a good confidence in the obtained result. Note that, this is opposite to that we have obtained with the surface surveys where the sensitivity assumes very low values along the conductive layer (check the sensitivity sections of the previous chapter). As previously discussed, all this can be explained by the fact that the electrodes are placed in the holes and thus in direct contact with the conductive layer.

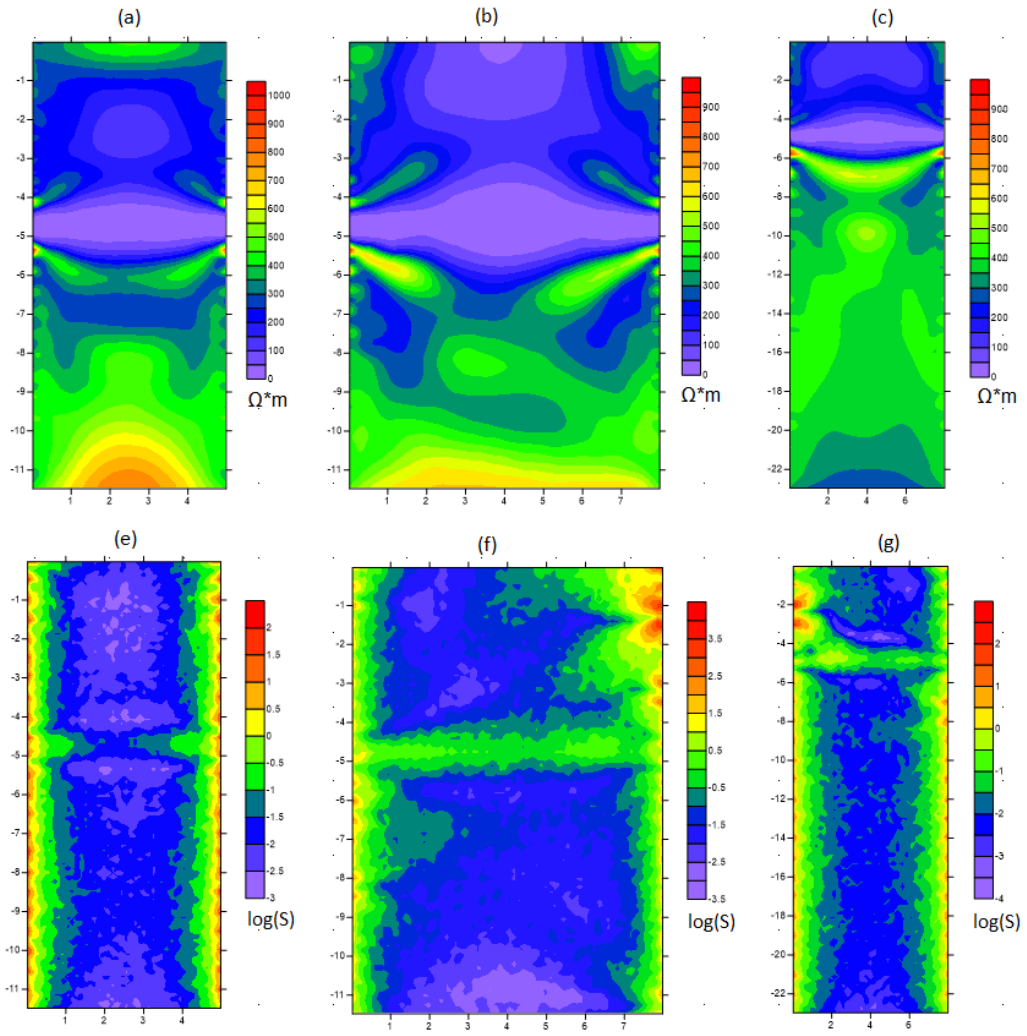

Figure 3.28 (a) Resistivity and (e) sensitivity sections obtained for subsoil model in Figure 3.27.a. (b) Resistivity and (f) sensitivity sections obtained for subsoil model in Figure 3.27.b. (c) Resistivity and (g) sensitivity sections obtained for subsoil model in Figure 3.27.c. Using an AB-MN array skip1

As previously discussed, the sensitivity decreases moving away from the electrode line. In this situation it is particularly clear as the conductive clay layer seems to have slightly a greater thickness halfway between the two holes, particularly in the survey with the two holes separated 8 m from each other and with electrodes spaced 0.5 m (Figure 3.28.b). The wells are located at a greater distance than half the length of the electrodes line in a hole and, as previously discussed, this is not the best configuration. In fact, if we check the other two resistivity sections obtained with a configuration of holes where the distance between them is less than half the length of a electrodes line in one well (Figure 3.28.a/c), it is evident that the thickness of the clay layer seems to remain

approximately constant also in the central part of resistivity sections. However, it should be noted that even with this configuration the tendency of the current lines to move in the most conductive layer and the excessive smoothing performed by the inversion code generate small artefacts. In fact, if we check the resistivity values close to the electrodes before the top and the bottom of the conductive layer, we find very high values, even double the real resistivities (300 Ω*m and 400 Ω*m). Because of this, in the central part of the section, there are small areas where the resistivity is underestimated compared to the real one. Furthermore, we can see that anomalous resistivity values also tend to arise at the vertical ends of the sections. It is important to note that the values of sensitivity in these areas are minimal and thus they should not be considered during the interpretation of the resistivity sections. Despite all this, it is evident that with a ERT cross-borehole survey we are able to correctly define the structure of the subsoil where a conductive layer is placed between two more resistive layers, also managing to define very precisely the thickness of each one. As we can see in Figure 3.29, if the thickness of the clay layer is increased to 2 meters (Figure 3.29.a), we are perfectly able to recognize it from the resistivity section (3.29.b), contrary to what we have seen for the resistivity sections obtained with ERT surface investigation.

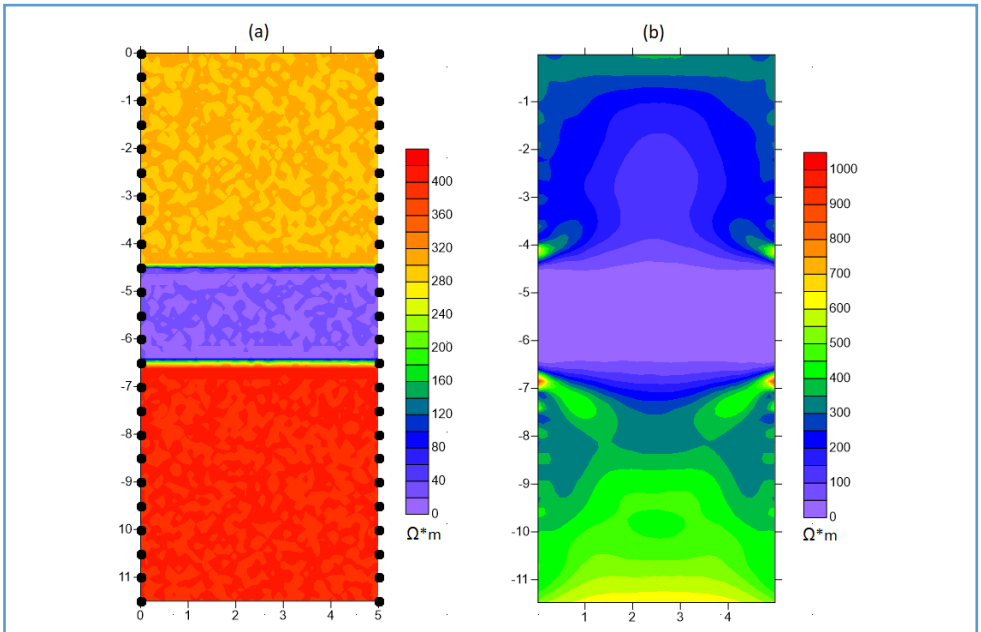

Figure 3.29 (a) Subsoil model and 48 electrode spaced 0.5 m in a cross-borehole configuration. (b) Resistivity section obtained for subsoil model (a) using an AB-MN array skip 1

Note that, the same small artefacts of the resistivity section in Figure 3.28.a are also present in the resistivity section of Figure 3.29.b. Despite this, we are perfectly able to recognize, from the two resistivity sections, a subsoil model with a clay layer of a few decimeters (Figure 3.27.a) from another one where the layer of clay is 2 meters thick (Figure 3.29.a), which is not possible in ERT surface surveys. We must underline that all the resistivity sections shown in this chapter have been obtained using a skip of 1. This is due to the fact that the resistivity sections achieved with higher skip (3 and 6) albeit they increase the penetration, as can be appreciated for example in Figures 3.30.b/d, they also increase the areas with resistivity artefacts in the center of the sections, as we can see for instance in Figures 3.30.a/c. Therefore, considering this kind of subsoil with a conductive layer in the middle of two more resistive, for the cross-borehole surveys it is more suitable the use of a no skip configuration, unlike the surface surveys where the investigations are more suitable to the use of higher skips, as we have seen in the previous chapter.

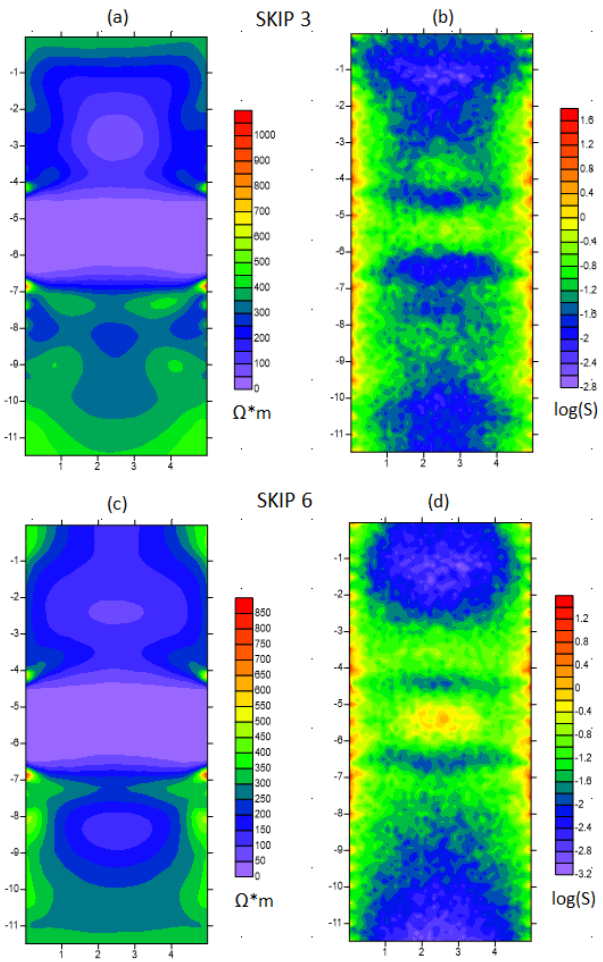

Figure 3.30 (a) Resistivity and (b) sensitivity sections obtained for the subsoil model of Figure 3.29.a using an AB-MN array with skip 3. (c) Resistivity and (d) sensitivity sections obtained for the subsoil model in Figure 3.29.a using an AB-MN array with skip of 6

3.3 Presence of a Discontinuous Clay Layer

3.3.1 Surface-Based Imaging

In this chapter we will highlight the ability of the ERT surface technique to locate discontinuities in the conductive clay layer. We will consider a subsoil model similar to those of the previous chapters but this time the conductive clay layer, with a thickness of few decimeters, will be discontinuous. The investigations will be simulated taking into account two different discontinuity values, 1 and 2 meters, various electrode spacing and configurations, in order to verify the link between them.

At first, we considered the subsoil model of Figure 3.31.a, where a discontinuous clay level (20 Ω*m) is placed in the middle of a more resistive one (400 Ω*m). The discontinuities of the clay layer are in the order of two meters and the surveys have been simulated using a line of 96 electrodes spaced 0.5 m. Figure 3.31 also shows the resistivity and sensitivity sections obtained simulating the measurements with this kind of subsoil model. It is clear that the short circuit phenomenon and the excessive smoothing performed by the inversion code also affect the investigation achieved with a discontinuous clay layer, in fact the latter seems to have a much greater thickness than the real one, as in the resistivity sections seen in chapter 3.2.1 with continuous clay layers. Furthermore, it is

evident that the Wenner array, as expected given the lower lateral sensitivity, does not allow us to detect the discontinuities, as well as the Dipole-dipole configuration with no skip, due to its poor penetration (Figure 3.31.e). Instead, the Dipole-dipole array with a skip of 6 is perfectly able to define the discontinuity of the clay layer and to locate it accurately , as shown in Figure 3.31.f.

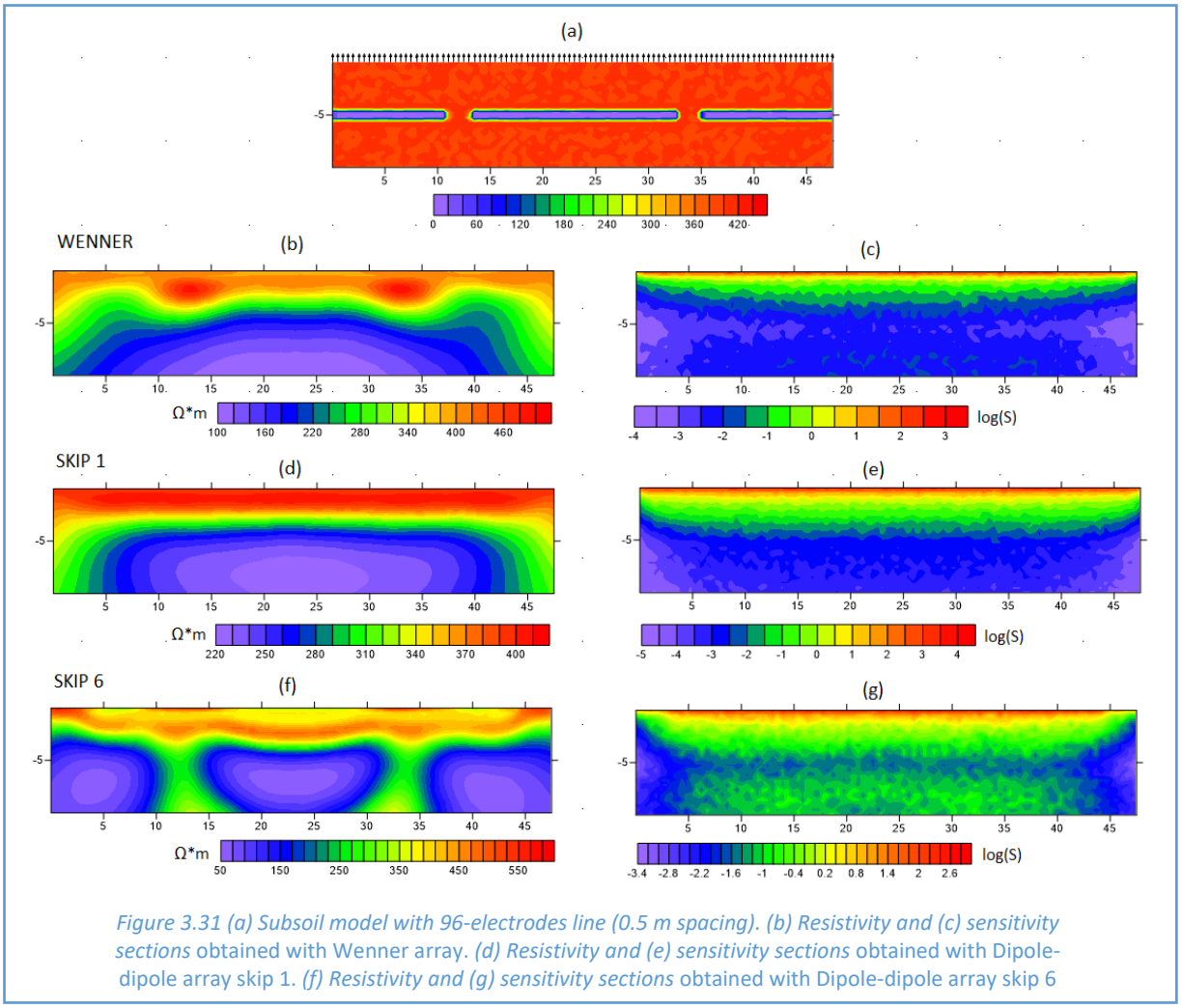

Figure 3.31 (a) Subsoil model with 96-electrodes line (0.5 m spacing). (b) Resistivity and (c) sensitivity sections obtained with Wenner array. *(d) Resistivity and (e) sensitivity sections* obtained with Dipole-dipole array skip 1. *(f) Resistivity and (g) sensitivity sections* obtained with Dipole-dipole array skip 6

If we consider discontinuities in the order of one meter, as in Figure 3.32.a, from the resistivity section (3.32.b) obtained using a Dipole-dipole array with skip of 6 it is still possible to appreciate the presence of the discontinuities, which however are much less clear than those of Figure 3.31.f. Instead, if we increase the spacing of the electrodes to 1 m, as shown in Figure 3.33.a, which is the same length as the discontinuities, the interpretation of the resistivity section (3.33.b) becomes more complicated and defining the discontinuities is much more difficult. In this situation, a solution to highlight the discontinuities is to use a logarithmic scale (Figure 3.33.c).

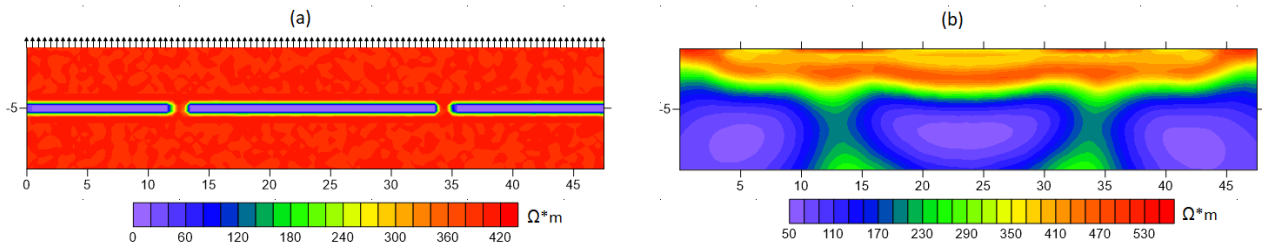

Figure 3.32 (a) Subsoil model with 96-electrodes line (0.5 m spacing) and (b) resistivity section obtained with a Dipole-dipole array skip 6

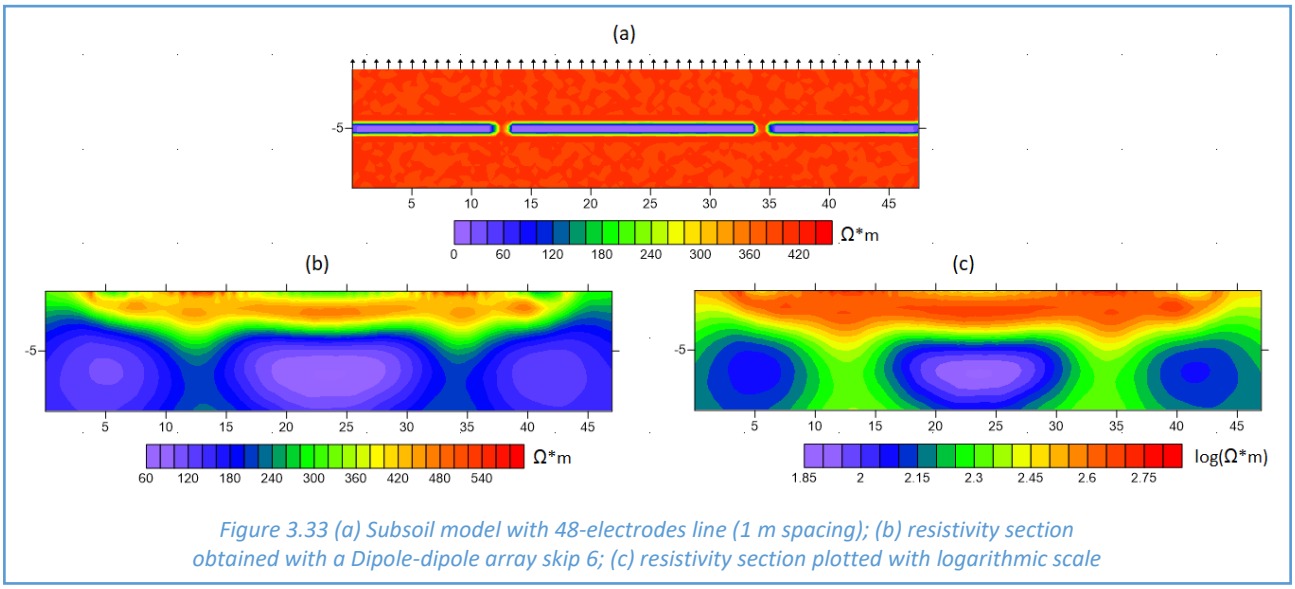

Figure 3.33 (a) Subsoil model with 48-electrodes line (1 m spacing); (b) resistivity section obtained with a Dipole-dipole array skip 6; (c) resistivity section plotted with logarithmic scale

Comparing Figures 3.31/32/33, it is clear that if the spacing of the electrodes is less than the length of the discontinuities, these last are easier to define while, the more the two have similar dimensions, the more difficult it is to detect the discontinuities. All this agrees with the sentences made in chapter 2.2, where we explained that the resolution of the survey is practically the same as the spacing. Obviously, if the spacing is even greater than the length of the discontinuities, detecting these last in the resistivity section (Figure 3.34.b/c) becomes very complicated, even if we use a logarithmic scale. Figure 3.34.a shown a line of 48 electrodes with 2 m of spacing that has been used to detect discontinuities of one meter in the clay layer.

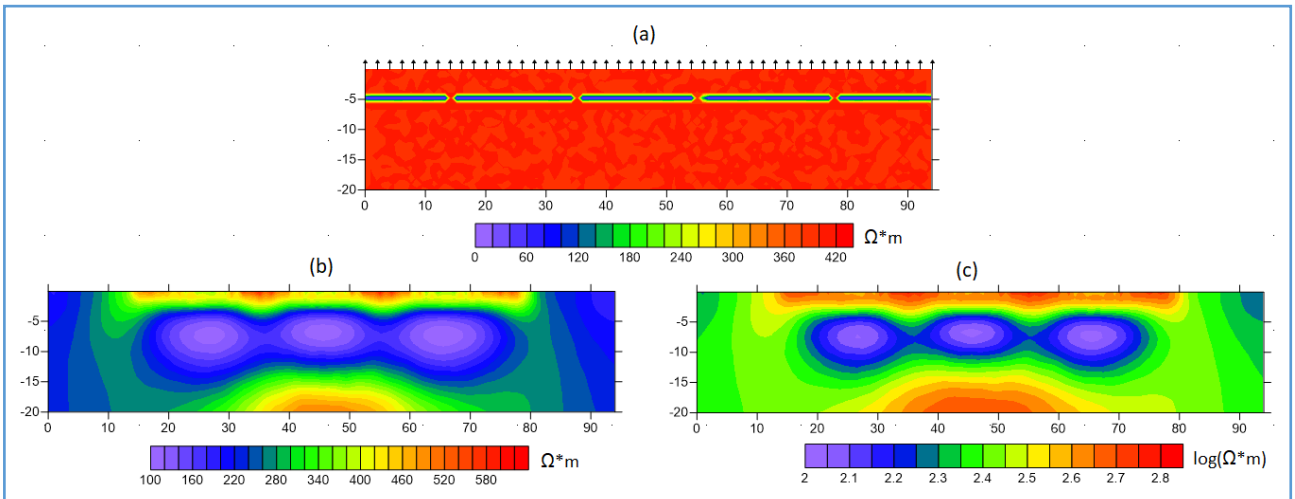

Figure 3.34 (a) Subsoil model with 48-electrodes line (2 m spacing); (b) resistivity section obtained with a Dipole-dipole array skip 6; (c) resistivity section plotted with logarithmic scale

Once again, we would like to highlight how the increase of the skip number shrinks laterally the validity of the resistivity section, particularly with a larger spacing of the electrodes as in this example. Despite this, from Figure 3.34 it is very clear that using a spacing of the electrodes which is greater than the length of the discontinuities does not allow us to identify effectively this latter, unlike the previous surveys where the discontinuities were much more evident, particularly when the spacing of the electrodes was less than their length (Figure 3.31).

3.3.2 Cross Borehole Based Imaging

In this chapter, we will apply the use of the ERT cross borehole technique to the study of discontinuous conductive clay layers. The resistivity sections of subsoil models where the clay layer is continuous will be compared with resistivity sections where the clay layer is instead discontinuous, in order to verify the differences between the two cases and to test the sensitivity of the ERT cross borehole technique to detect these discontinuities. As in the previous chapter, different lengths of the discontinuities and spacing of the electrodes will be taken into account, and the surveys will be steadily simulated using an AB-MN acquisition scheme with a skip of 1. At first, we considered two holes separated 5 meters from each other and 24 electrodes spaced 0.5 m in each hole. Three different subsoil models have been investigated, the first is the same as in Figure 3.27.a, with a continuous conductive clay layer in the middle of two more resistive ones, while the other two models have a discontinuous conductive clay layer placed in the middle of one more resistive, in one case the discontinuity have a length of 0.5 m (Figure 3.35.b) and in the other a length of 1 m (Figure 3.35.c). As we can see from the resistivity sections of Figure 3.35.d/e/f, we are able to define very precisely the thickness of the clay layer but the short circuit phenomenon and the excessive smoothing performed by the inversion code induce the formation of areas with unreal resistivity values (artefacts), such as already discussed in chapter 3.2.2. Furthermore, is clear that they also influence the resistivity values in the discontinuity area of the clay layer. Although in the resistivity sections is possible to define the presence of a discontinuity, particularly with the logarithmic scale (Figure 3.36.a/b), it is not possible to correctly evaluate its length.

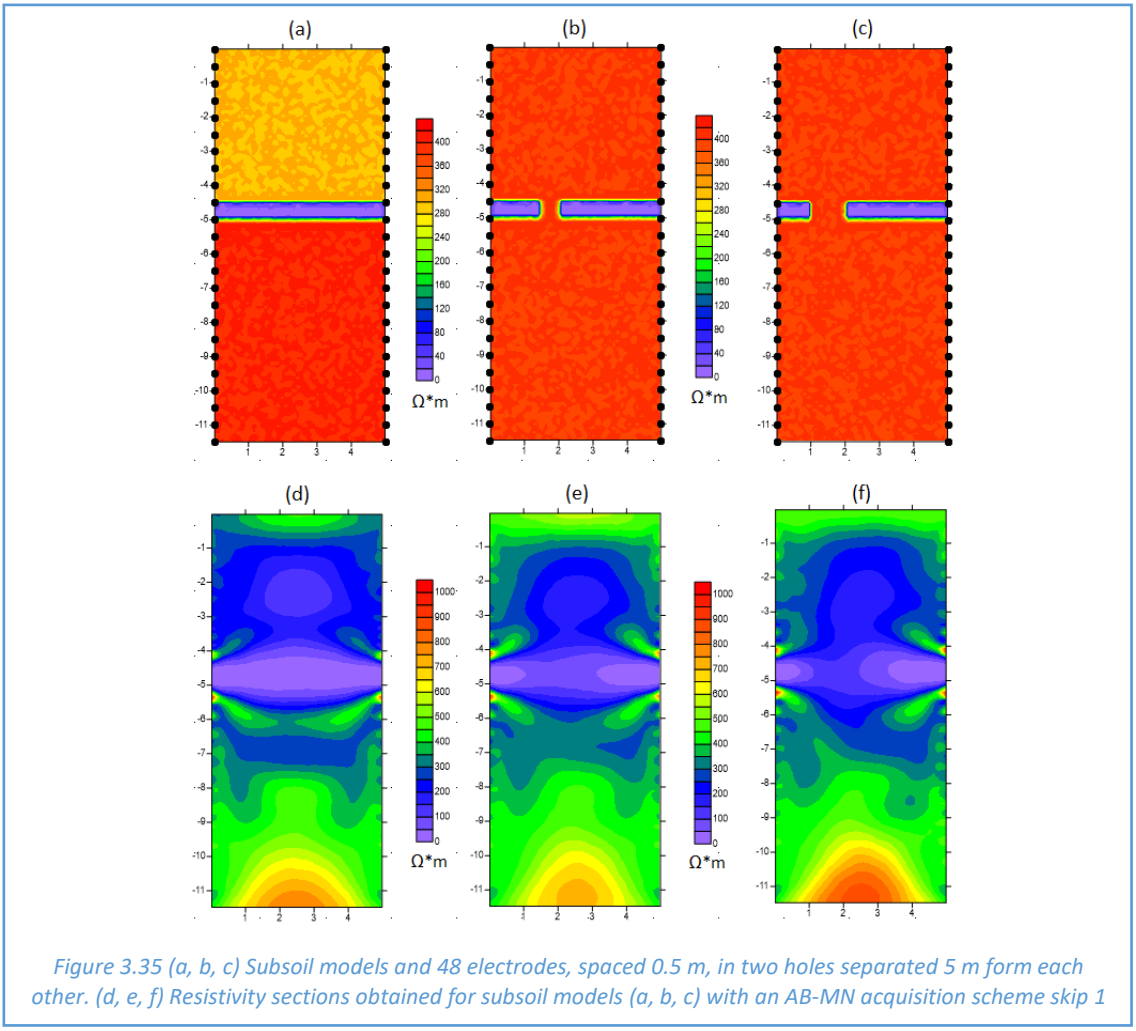

Figure 3.35 (a, b, c) Subsoil models and 48 electrodes, spaced 0.5 m, in two holes separated 5 m form each other. (d, e, f) Resistivity sections obtained for subsoil models (a, b, c) with an AB-MN acquisition scheme skip 1

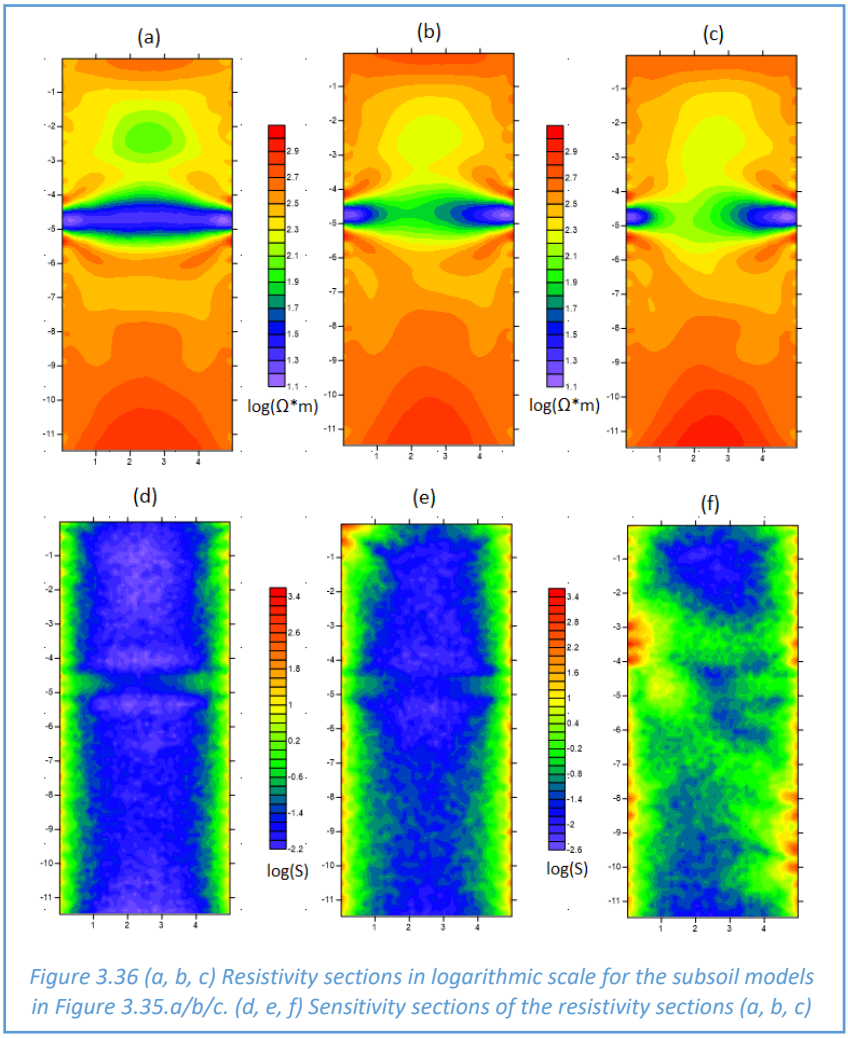

Figure 3.36 (a, b, c) Resistivity sections in logarithmic scale for the subsoil models in Figure 3.35.a/b/c. (d, e, f) Sensitivity sections of the resistivity sections (a, b, c)

As we can see from Figure 3.38, even by increasing the spacing of the electrodes to 1 meter (Figure 3.37), from the resistivity sections that we have obtained, we are able to correctly define the thickness of the impermeable clay layer and to understand that it is discontinuous. Despite this, due to the conductive layer and the excessive smoothing performed by the inversion code, it is practically impossible to define the real structure of the clay layer, particularly we are unable to correctly estimate the lengths of its discontinuities.

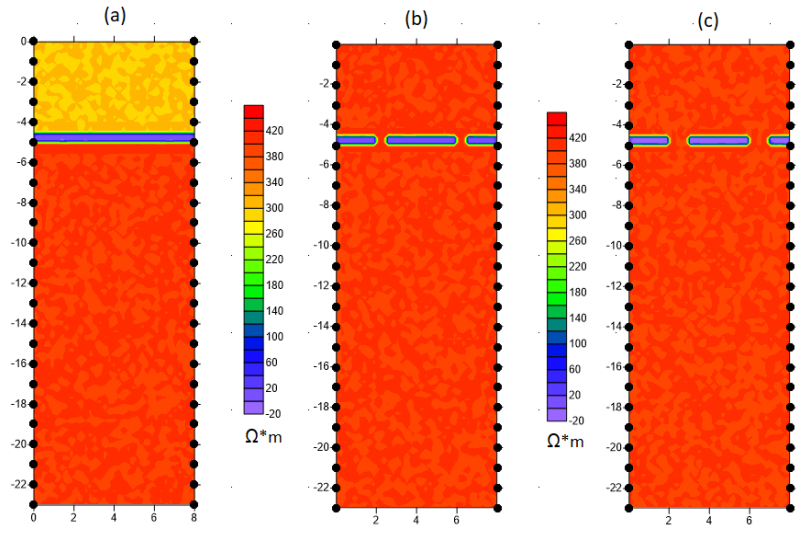

Figure 3.37 (a, b, c) Subsoil models and 48 electrodes, spaced 1 m, in two holes separated 8 m form each other

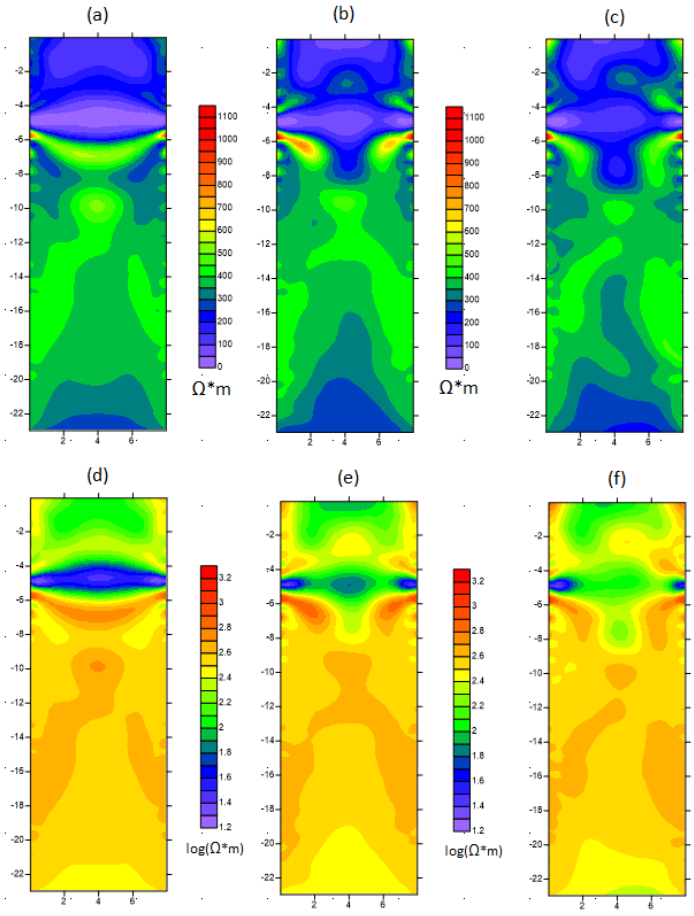

Figure 3.38 (a, b, c) Resistivity sections for the subsoil models in Figure 3.37.a/b/c.
(d, e, f) Resistivity sections in logarithmic scale for the subsoil models in Figure 3.35.a/b/c

After this analysis, it is clear that the use of the ERT cross borehole configuration helps us to see better the discontinuities, particularly with the logarithmic scale, even if their size is similar to the spacing of the electrodes. Nevertheless, the main limit of applying the cross borehole technique to the search of discontinuities is the fact that the area investigated is only between the two holes and therefore very limited, as opposed to the surface ERT technique which allows us to map much larger areas. Thus, as concerns the mapping of discontinuities of a layer, the ERT surface technique turns to be more advantageous than the cross-borehole configuration, which instead remains more advantageous for defining the correct thickness of the layers.

4. STUDY CASE

In this chapter, we will present an example of a real study case with a subsoil structure similar to the models that we described in chapter 3 with a conductive clay layer, probably a paleo-soil, in the middle of two more resistive layer of gravel. ERT surveys were part of the preliminary studies for the operation of remediation of a polluting industrial site, which name and exact location will not be provided in this thesis as the lawsuit is still pending, and their aim was mainly to define if the clay layer is continuous or not and to locate the position of any discontinuity. After a brief geological framing of the study area, we will present the results of the ERT surveys obtained from the surface and from a couple of cross-boreholes. Finally, we will present the results of a time-lapse ERT acquisition, performed with the cross-borehole technique, for a controlled irrigation experiment. This experiment was aimed to verify the correct working of a draining trench, completely filled with coarse gravel and therefore very permeable, that has been placed upstream to the industrial site and which function should be to prevent pollutants from reaching the aquifer below the investigated area, making the water infiltrate to the deeper aquifer before it reaches the subsoil of the industrial site.

4.1 Geological Framework

The investigation area is located in the province of Pordenone within the Friuli High Plain. The Friuli Plain is located at the north-eastern end of the Adria micro-plate and corresponds to the easternmost sector of the Po Valley, as is generally defined in Geography. It represents the eastern portion of the foreland area of the south-eastern alpine chain and the plain is therefore the expression of the progressive accumulation of sediments, transported by the rivers fed by the south-eastern Alps, which are progressively filling the depositional basin. The succession of deposits that make up the Friuli plain is not continuous, since most of them have been settled in an alluvial environment and are therefore also characterized in depth by the presence of erosive surfaces, not always clearly distinguishable, and by paleo-soils (Fontana et al., 2019). One of the most peculiar moment for the formation of the current Friuli plain was the Last Glacial Maximum, generally abbreviated to LGM. This period lasted on a global scale from 29.000 to 19.000 years ago (Clark et al., 2009) and corresponds to the phase during which huge glaciers occupied the main Alpine valleys and with their fronts reached the plains or close to it (Castiglioni , 2004; Monegato et al., 2007; 2017). During the LGM, the glacial and periglacial conditions in the mountain basins promoted a considerable production of debris in the Alpine and pre-Alpine area and, at the same time, the movement of the glaciers guaranteed an effective transport of sediments to the glacial fronts, feeding the fluvio-glacial systems with a considerable liquid and solid flow rate. In the Friuli plain, the great sedimentation promoted a fast and widespread (horizontal and vertical) development of the major river systems and therefore the formation of large alluvial megafans. Particularly, the Friuli plain has been essentially built by the depositional systems of Isonzo, Torre, Tagliamento, Cellina, and Meduna, which, from their valley outlets, generated large gravelly cones and alluvial megafans. The term megafan means a fan-shaped depositional system having an extension that can exceed thousands of km^2 and which is characterized by an apical portion, consisting of gravelly deposits, and by a distal portion, essentially composed by fine sediments (Fontana et al., 2004; 2008; 2014a). In the case of the Friuli plain, the thickness of sediments stored during the LGM is generally greater than 15 m, but can reach a maximum of 25-35 m, as documented in the megafans of Tagliamento, Cormor and Piave (Zanferrari et al., 2008a-b; Fontana et al., 2012 and 2014a; Hippe et

al., 2018). In the Lateglacial and especially in the initial Holocene, the withdrawal of glaciers within the Alpine valleys led to the confinement of river activity within engraved channels, causing, in addition to the terracing of the apical portion of the alluvial megafans, the transformation of large areas of the megafans into bypass surfaces without deposition. In the areas abandoned by the flood activity, soils with relatively homogeneous features have been developed throughout the plain. Particularly, the gravels of the high plain have been altered, generating soils with clay layers and accumulations of oxides that give to the soils a typical reddish color.

If we consider the subsoil of the investigated site, it is composed mainly by the Vivaro Unit, i.e. the alluvial deposits of the Cellina basin, related to the last aggradation phase of its alluvial fan which culminated in the LGM and continued until the end of the Lateglacial (Zanferrari et al., 2008a-b). Figure 4.1 shows an extract from the "Geological Map of Friuli Venezia Giulia" (2006) where we can appreciate the depositional area, during the LGM, of the Cellina alluvial megafan, where the survey site is located (check Figure 4.2 for the legend).

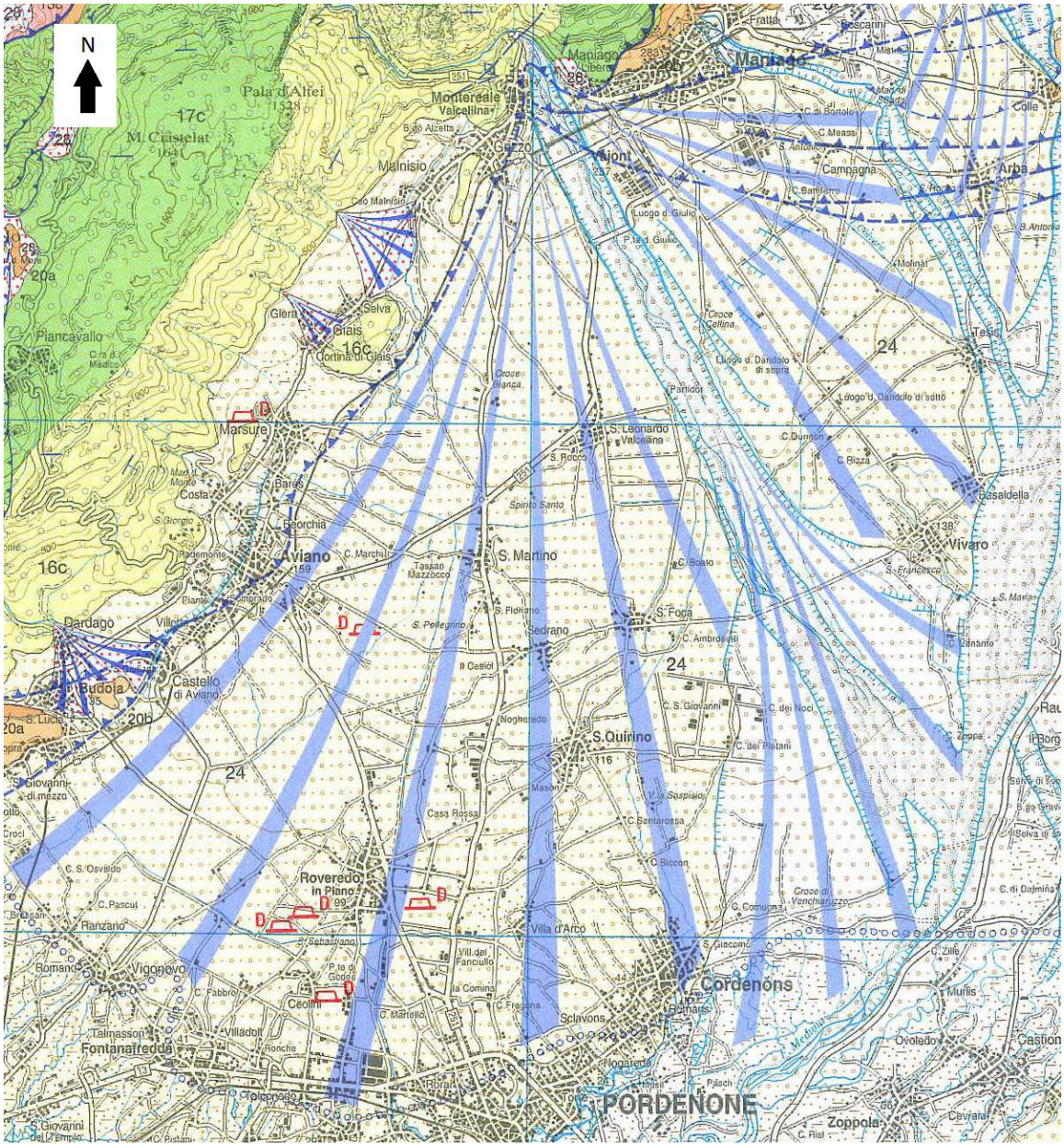

Figure 4.1 Extract from "Geological map of Friuli Venezia Giulia" (2006). Scale 1:150.000

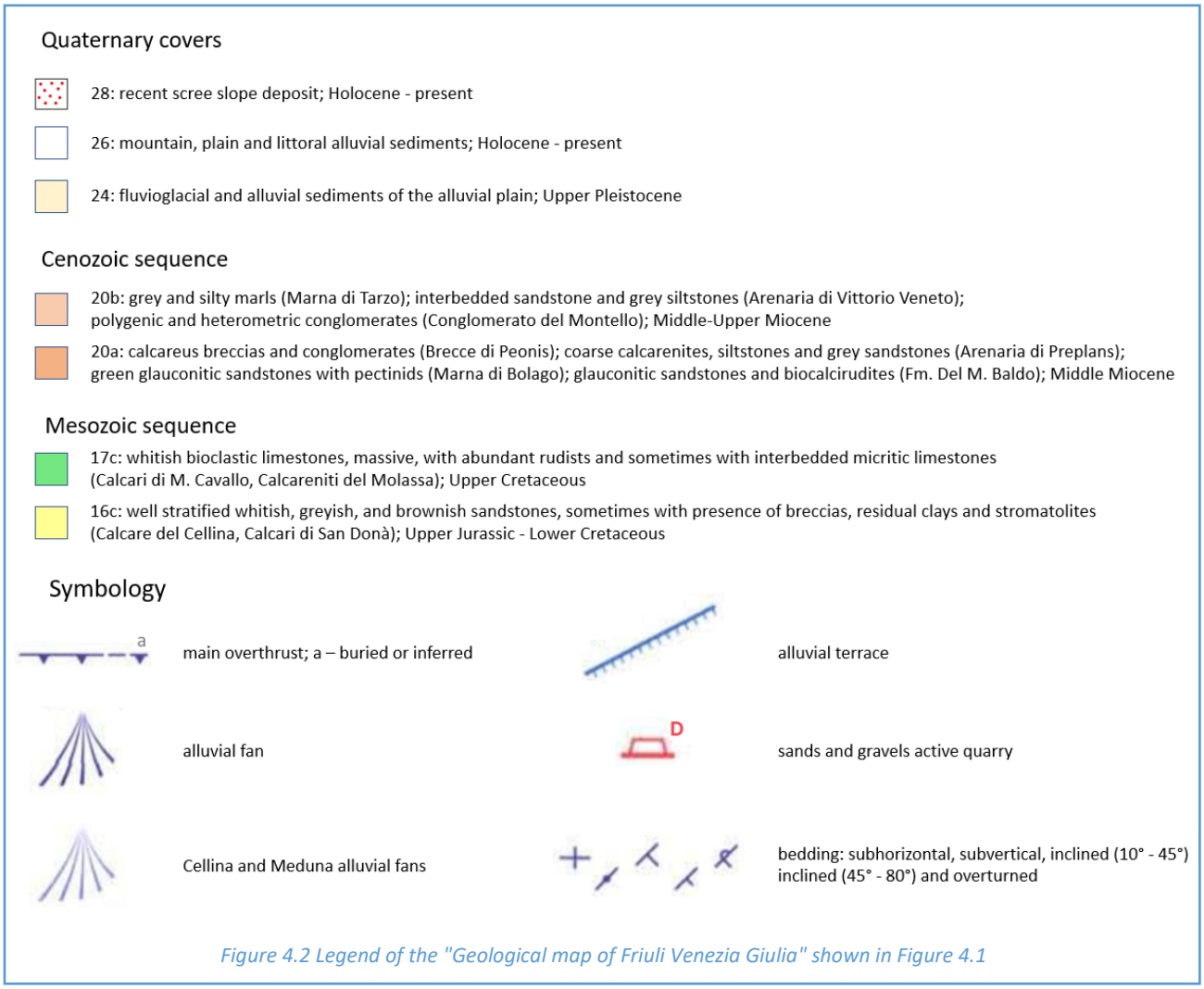

Figure 4.2 Legend of the "Geological map of Friuli Venezia Giulia" shown in Figure 4.1

In the high plain, the subsoil is mainly composed by alluvial deposits of a braided system which migrated continuously for subsequent avulsions. Therefore, in the evolution of the conoid, coarse sedimentation phases alternated with destructive and steady-state moments, even prolonged, which ensured the formation of soils that may have been subsequently buried. Therefore, in the high plain, the Vivaro Unit is mainly composed by gravels, with a sub-horizontal coarse stratification and sometimes with a slightly silty-sandy matrix, in which even buried paleo-soils can be interspersed (Fontana et al., 2019). The subsoil of the investigated site is preserved from the terracing action occurred during the early Holocene and it is mainly composed by layers of gravel, with a total thickness of even 40 meters. However, there is an intercalation of a very discontinuous clay layer, a few decimeters thick and probably representing a paleo-soil, at a depth of about 6-7 m. The discontinuities of this clay layer are very important as regards the underground hydrology of the area since the clay layer does not perfectly act as an aquiclude and therefore allows the communication between surface spillage of contaminants and the deep aquifer.

4.2 Surface Based Imaging

The measurements have been performed with the multielectrode instrument Syscal-Pro, owned by the Department of Geosciences of the University of Padua. Two surface lines have been realized with 120 electrodes spaced 0.80 meters, for a total length of 95.2 meters which, therefore, should have guaranteed a penetration of about 20 meters in depth. The measurements were performed

with a dipole-dipole configuration skip 8, with a complete acquisition of the reciprocals. The datasets have been subjected to direct and reciprocal checks with an error threshold of 10% as the survey environment was particularly noisy due to the presence of nearby hydraulic barriers and the need to drill the asphalt of the road to place the electrodes. The inversion process has been carried out with the CRTomo code (Kemna), using a preferential horizontal smoothing, and the obtained resistivity and sensitivity sections are plotted using the program Surfer (Golden Software). The main target of these surveys was to define if the clay layer is continuous or not, determining the location of the discontinuities.

The first line of electrodes "S1" follows exactly the path that was subsequently used for the construction of the drainage trench, upstream of the industrial plant under investigation. The obtained resistivity and sensitivity sections are shown below in Figure 4.3.a/b.

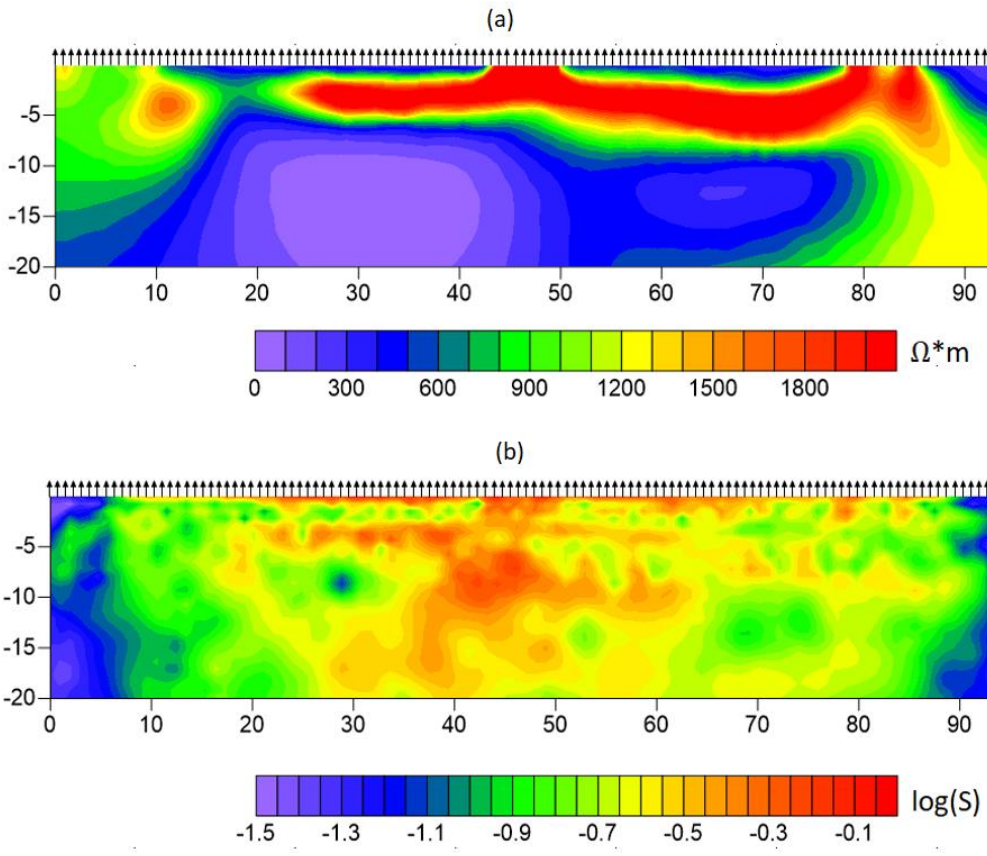

Figure 4.3 (a) Resistivity and (b) sensitivity sections obtained for the ERT surface survey S1 performed upstream of the industrial plant under investigation, with a line of 120 electrodes spaced 0.8 m and a Dipole-dipole configuration skip 8

The resistivity section of Figure 4.3.a confirms the problems discussed in chapter 3, due to the current line concentration in the conductive layer and the excessive smoothing performed by the inversion code, it is practically impossible to define the real thickness of the clay layer. Despite this, from the resistivity section, we can understand that the clay layer develops at a depth of 7-8 meters, but also that it seems to be interrupted at the right end of the section and to deepen at the left side. However, as we discussed in chapter 2.5, image appraisal with sensitivity maps can offer great insight to make assessments about the results and to define the section boundaries in the best way possible. From Figure 4.3.b, it is clear that the sensitivity is minimal at the lateral ends of the section. Furthermore, as we have shown with the direct models of chapter 3, by increasing the number of skips the validity of the resistivity section tends to shrink laterally. In this investigation, the skip is 8

and therefore even greater than that used in the direct models of chapter 3, where it was at most 6. Considering all this, it is possible to define the most likely boundaries to the resistivity section and obtain the result shown in Figure 4.4. where it is clear that the clay layer is continuous upstream of the industrial plant and develops approximately at a constant depth of 7-8 meters.

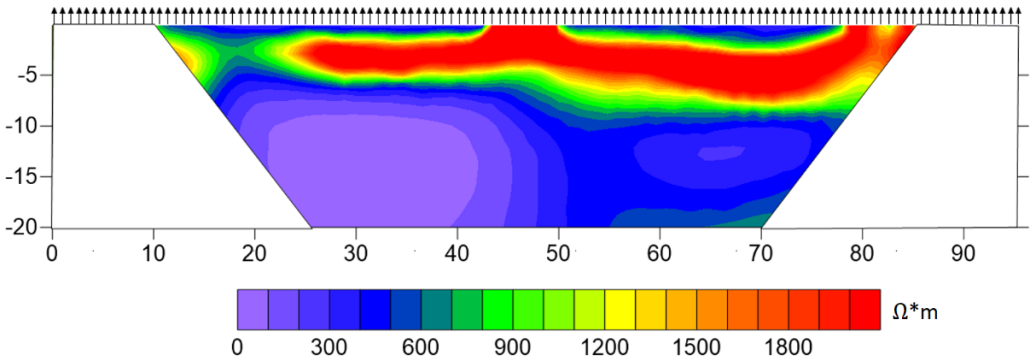

Figure 4.4 Final resistivity section obtained for the ERT surface survey S1 performed upstream of the industrial plant

The second electrodes line (S2) develops downstream the industrial plant, in a position where the discontinuity of the clay level is known thanks to pre-existing mechanical surveys. The obtained resistivity and sensitivity sections are shown below in Figure 4.5.a/b.

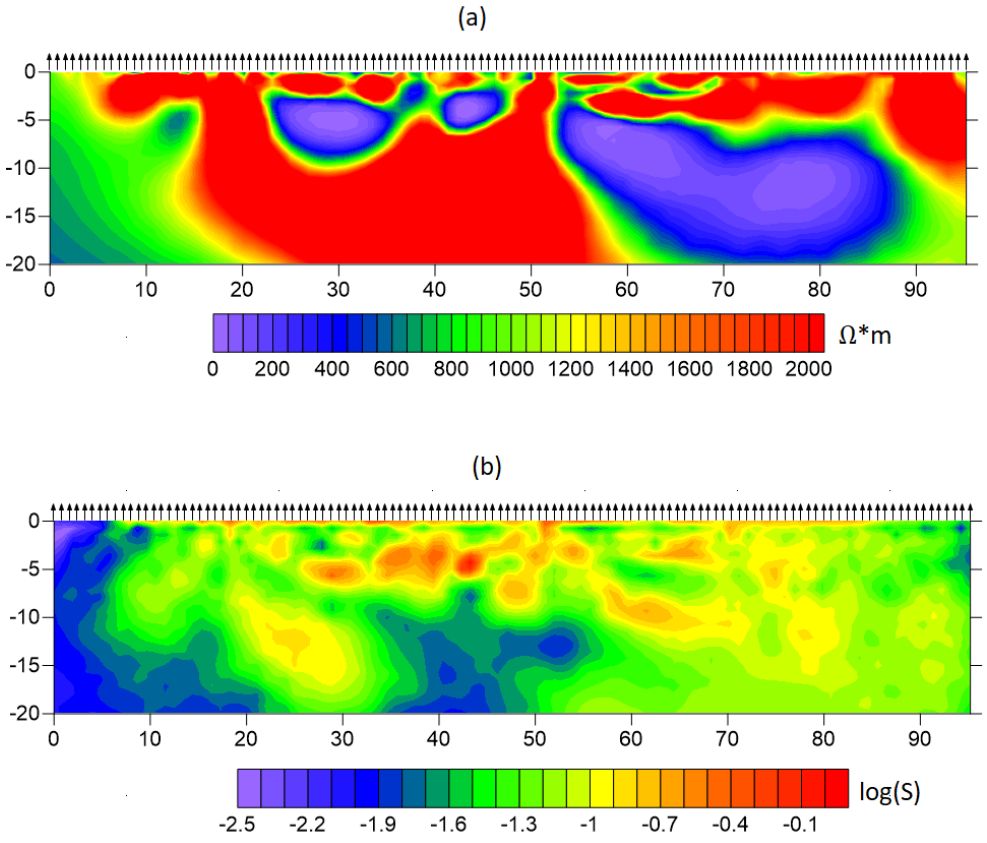

Figure 4.5 (a) Resistivity and (b) sensitivity sections obtained for the ERT surface survey S2 performed downstream of the industrial plant under investigation, with a line of 120 electrodes spaced 0.8 m and a Dipole-dipole configuration skip 8

As before, we defined the most likely boundaries to the resistivity section of Figure 4.5.a and we obtained the final result shown in Figure 4.6.

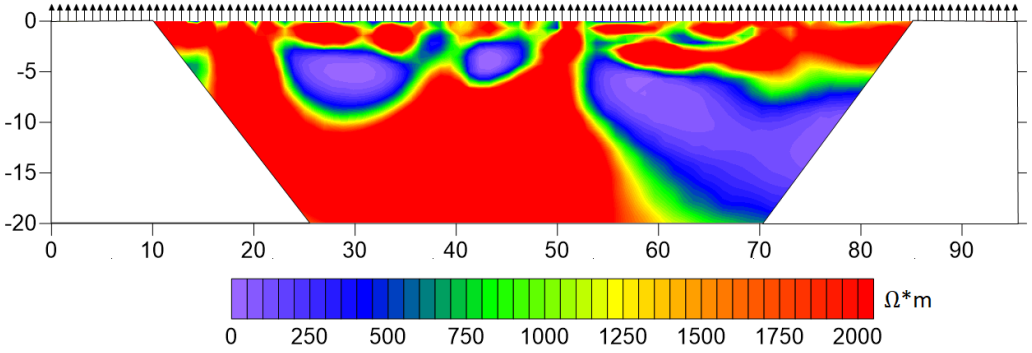

Figure 4.6 Final resistivity section obtained for the ERT surface survey S2 performed downstream of the industrial plant

As foreseen by the direct models of chapter 3, the resistivity section in Figure 4.6 shows with great clearness the presence of the clay level and its discontinuities, probably paleochannels. Therefore, the result confirms the capacity of the ERT surface survey to detect the discontinuities if they have a similar size, equal or greater, of the spacing of the electrodes but, even in this case, the thickness of the clay layer cannot be correctly defined.

4.3 Cross Borehole Based Imaging

Following the ERT surface surveys, two ERT investigations were carried out, upstream of the industrial plant, with the cross-borehole technique. Two pairs of holes (hole 1 - hole 3 and hole 2 - hole 4, in Figure 4.5) have been placed perpendicularly to the position foreseen for the construction of the drainage trench, approximately in the middle of the first ERT surface line S1 (chapter 4.2). All the holes are 8 meters apart from each other. In Figure 4.7 we can appreciate the scheme with which the two pairs of holes have been placed perpendicularly with respect to the first surface electrodes line S1 and the future position of the draining trench, not yet realized when the two ERT cross borehole surveys were carried out.

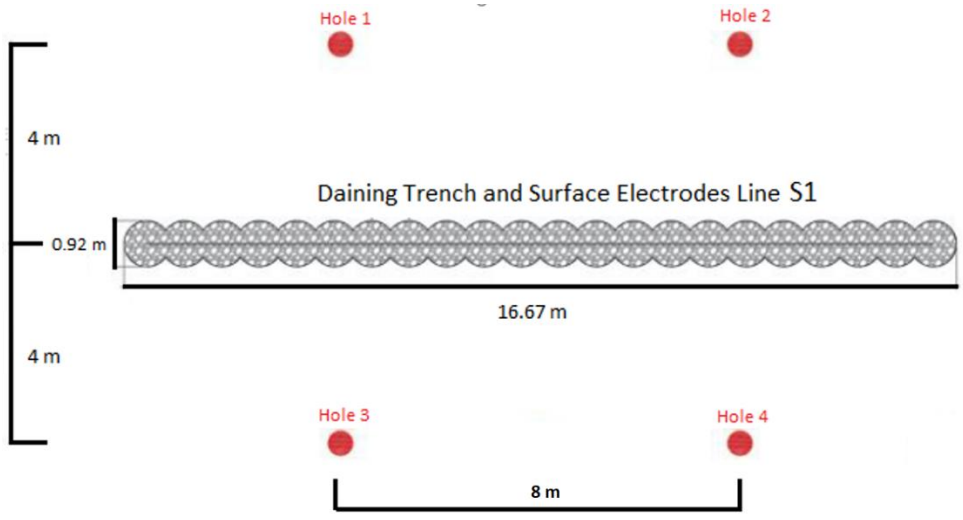

Figure 4.7 Position of the two pairs of cross boreholes with respect to the future draining trench

The monitoring wells have a depth of 20 meters, each one is equipped with 24 electrodes spaced 0.8 meters, starting from the first electrode at 1.6 meters of depth. Figure 4.8 shows the geometry with which each hole has been realized.

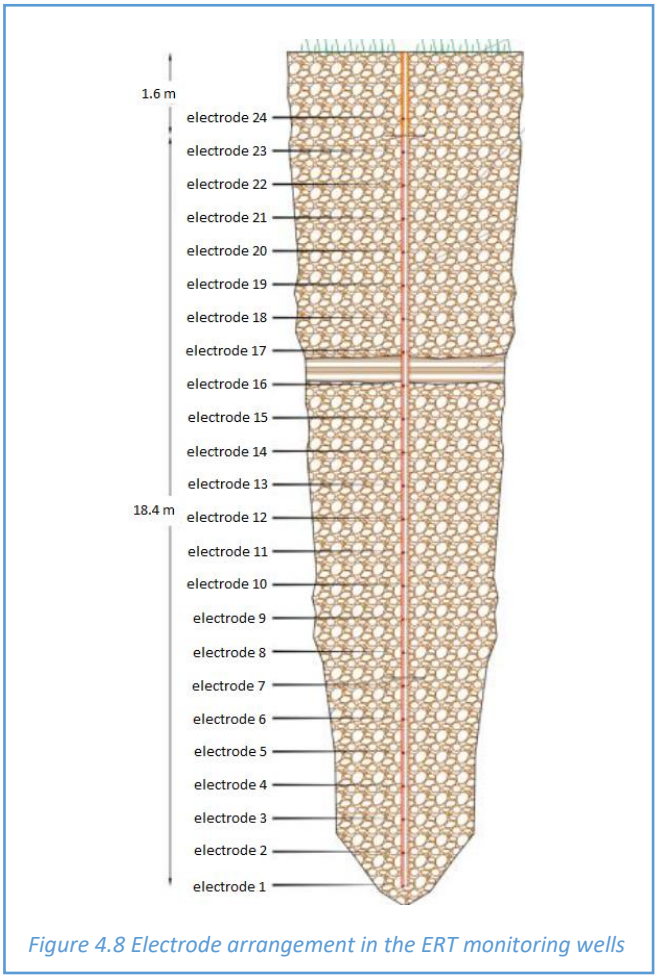

Figure 4.8 Electrode arrangement in the ERT monitoring wells

The measurements have been realized using an AB-MN configuration scheme with skip 4, with a complete acquisition of the reciprocals. As in the surface surveys of chapter 4.2, the datasets have been subjected to direct and reciprocal checks with an error threshold of 10% and the inversion process has been carried out with the CRTomo code (Kemna) using a preferential horizontal smoothing. The obtained resistivity and sensitivity sections, plotted using the program Surfer (Golden Software), are shown below in Figure 4.9 and 4.10.

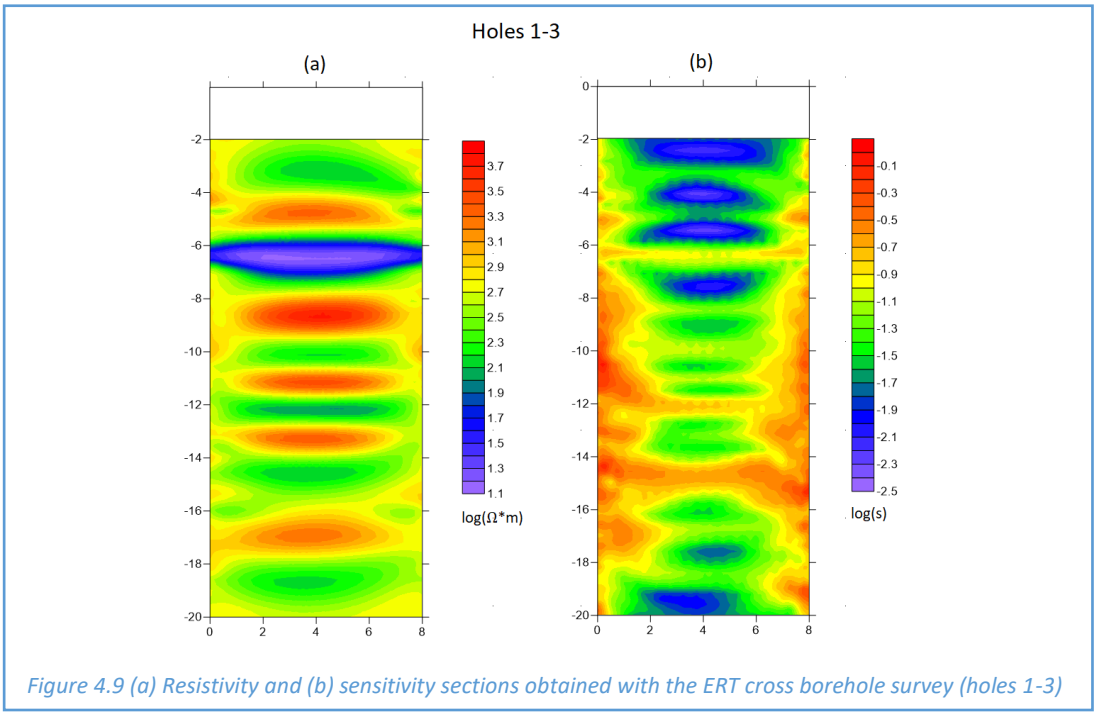

Figure 4.9 (a) Resistivity and (b) sensitivity sections obtained with the ERT cross borehole survey (holes 1-3)

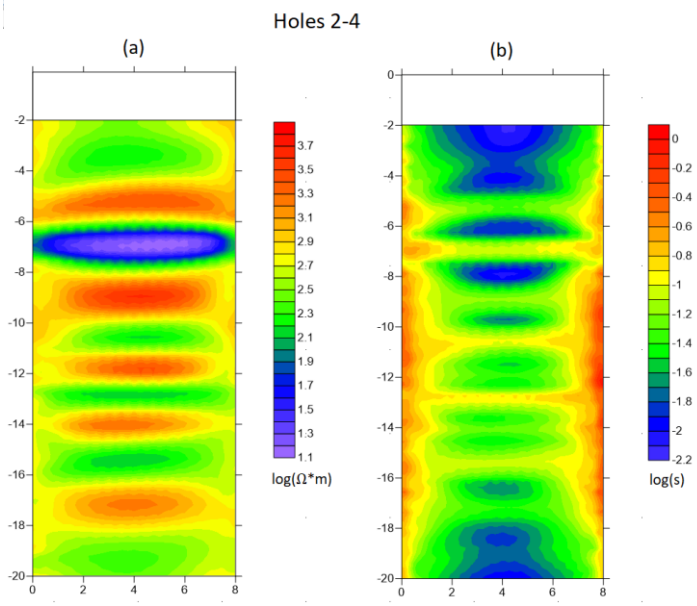

Figure 4.10 (a) Resistivity and (b) sensitivity sections obtained with the ERT cross borehole survey (holes 2-4)

The clay level at about 7 m depth is clearly identifiable on both the resistivity sections of Figure 4.9.a and Figure 4.10.a. As expected by the direct models developed in chapter 3, unlike the surface ERT surveys seen in chapter 4.2, with the cross borehole investigations we are able to define the real thickness of the clay layer, which is a few tens of centimeters and not much greater as it seems in the resistivity section of Figure 4.4. Therefore, we can confirm that, if the target of the investigation is to define the real thickness of an isolated clay layer, we cannot do it only with an ERT surface survey but it is necessary to use the ERT cross borehole technique.

4.4 Surface & Cross Borehole Based Imaging

In order to extend the correct information of the clay layer thickness, obtained from the cross-borehole surveys, also outside the area between the holes, we tried to use simultaneously, during the inversion process, the dataset obtained from the first long surface electrodes line S1 and the datasets obtained from the two pairs of cross-borehole. As we can see from Figure 4.7, the two pairs of holes, used for the ERT cross borehole surveys, are perpendicular to the long electrodes line S1 realized in surface. Therefore, we were forced to make an approximation and we hypothetically rotated the position of the holes so that they fell within the surface electrodes line. In Figure 4.11 we can appreciate the new hypothetical configuration of the electrodes used to carry out the inversion process by combining the three different datasets obtained separately from the three different surveys shown in the previous chapters.

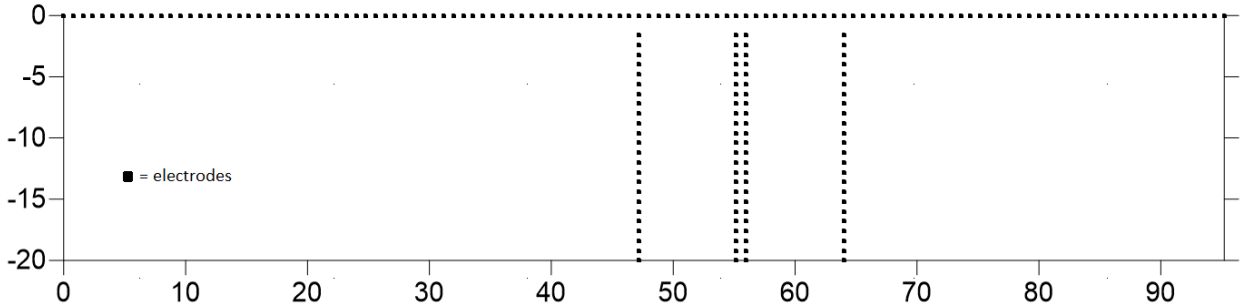

Figure 4.11 Electrodes configuration for the surface & cross-borehole based imaging

The inversion process has been realized again with the CRTomo code (Kemna), using a preferential horizontal smoothing, and below, in Figure 4.12, are shown the resistivity and sensitivity sections obtained and plotted with Surfer (Golden Software).

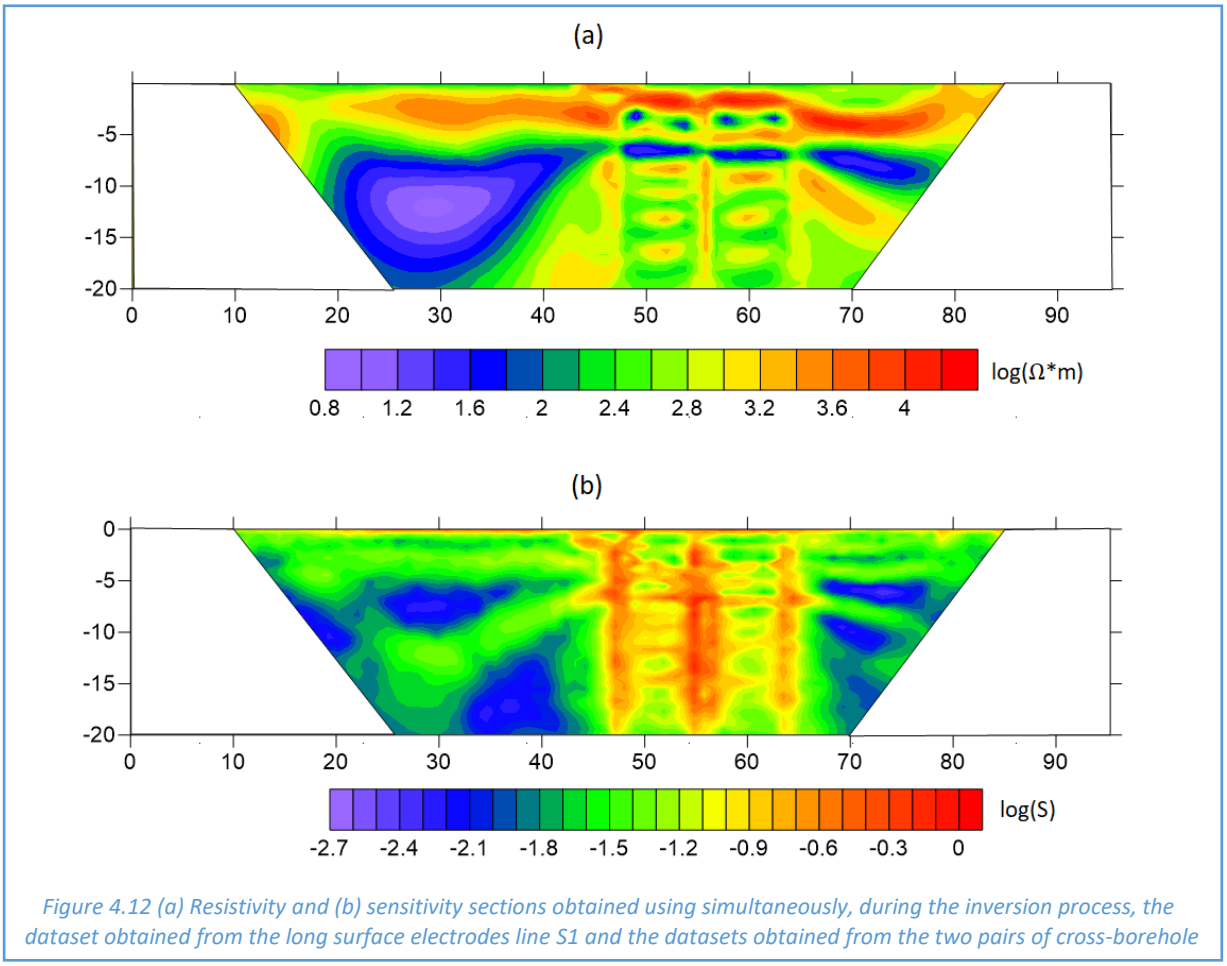

Figure 4.12 (a) Resistivity and (b) sensitivity sections obtained using simultaneously, during the inversion process, the dataset obtained from the long surface electrodes line S1 and the datasets obtained from the two pairs of cross-borehole

From Figure 4.12.a we can appreciate that combining the surface measurements and the cross-borehole measurements allows us to obtain a much more correct resistivity section than that obtained in chapter 4.2 using only the surface dataset (Figure 4.4). In fact, by comparing the resistivity sections of Figure 4.4 and Figure 4.12.a, it is clear that the cross-borehole datasets help to define much better the limited thickness of the clay layer even outside the area between the wells. Particularly, if we observe the right side of the section, towards which the wells have been placed, it is clear that the interpretation of the limited thickness of the clay layer is much easier than in the resistivity section of Figure 4.4. Note that, as expected, the sensitivity is greater near the electrodes (Figure 4.12.b), while it decreases as we move away from them. This allows us to estimate with great confidence the thickness of the clay layer between the holes, while, as we move away from them, the sensitivity decreases and consequently the information about the correct thickness of the clay layer, obtained by the cross-borehole datasets, is lost and the latter seems to be thicker. This is particularly clear by paying attention to the left side of the resistivity section of Figure 4.12.a, in fact greater is the distance from the holes and more the resistivity section tends to resemble to that of Figure 4.4, where the thickness of the clay layer seems to be several meters instead of a few decimeters as in reality.

4.5 Time-Lapse Based Imaging

The time-lapse investigation has been realized upstream of the draining trench, using 48 electrodes included in the holes 1 and 2 (24 electrodes in each well with a spacing of 0.8 m) and 4 electrodes positioned in the surface, with a spacing of 1 m, between the two holes. The irrigation lasted for 9 and a half hours, for a total of 16600 liters of water released into the soil through an infiltration box placed on the surface between the holes 1 and 2. The irrigation scheme and the acquisition times are shown in the following Table 4.1:

Time	H_2O	Acquisition time
Day 1		
12:00	Irrigation Start	t0
12:35	1000 l	t1
13:08	2000 l	t2
13:45	3000 l	t3
14:20	4000 l	t4
14:55	5000 l	t5
15:30	6000 l	t6
16:00	7000 l	t7
21:30	16600 l	x
	Stop Irrigation	
Day 2		
07:50	x	t8
10:00	x	t9
12:00	x	t10
14:00	x	t11
16:00	x	t12

Table 4.1 Irrigation scheme and acquisition times for the time-lapse survey

If we carry out the inversion processes of the acquired datasets individually and then we compare the obtained resistivity sections to study the infiltration process, we do not get significant results because they are very similar to each other and therefore we are unable to appreciate the infiltration process itself. For instance, we can check Figure 4.13 which shows the resistivity sections obtained, using the inversion code R2 (Binley) and a 10% error, for the dataset at time t0 and t1.

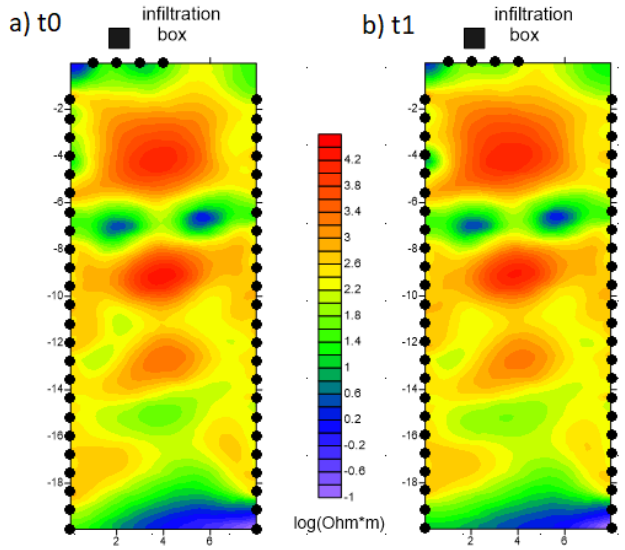

Figure 4.13 Obtained resistivity sections at time (a) t0 and (b) t1

From Figure 4.13 it is clear that the resistivity sections obtained at time t0 and t1 are practically the same and therefore it is impossible to study the infiltration process. But, as we introduced in chapter 2.2.3, in order to enhance the resistivity changes from one-time frame to the next, a ratio inversion approach is advisable to use. For each quadripole the data to be inverted at each time step are constructed from the ratio of resistances of that same quadripole in the current time step (R_t) and in the reference initial time step (R_0): $R_{ratio} = R_t/R_0$. The results of the inversion process are consequently given in terms of resistivity ratios with respect to the initial reference state R_0. Therefore, the sections that we obtain will be plotted in terms of percentage variations of resistivity with respect to the first measurement at time t0. In fact, if we apply this kind of inversion process to the datasets obtained from the infiltration test, we will obtain much more meaningful results. Figure 4.14 shows the percentage changes in resistivity of the first 7 measured datasets, compared to the reference resistivity section t0, obtained during the infiltration test in the time interval in which the water was released into the soil.

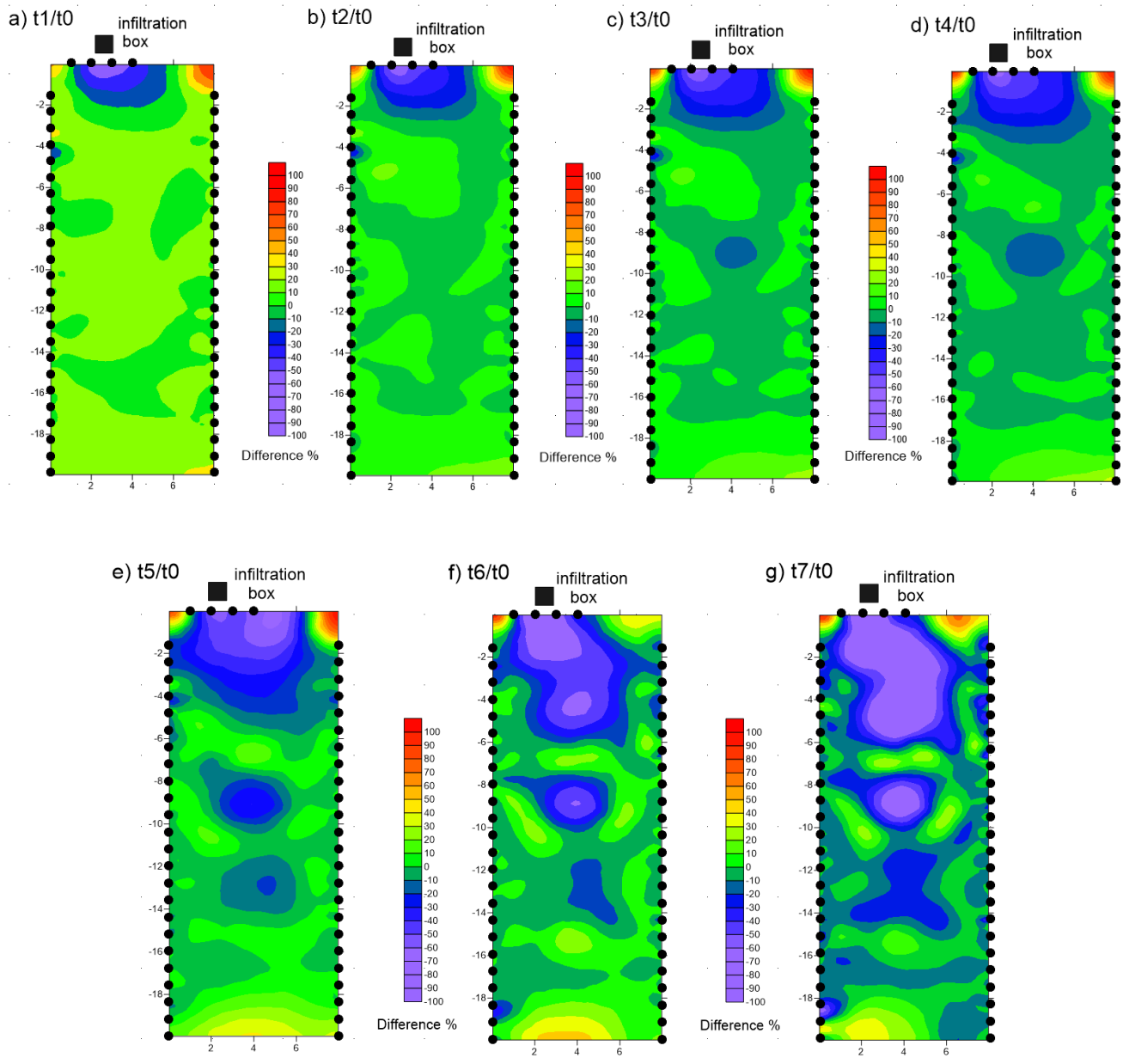

Figure 4.14 Resistivity ratio with respect to background (t0) at first seven time-steps of the infiltration test

From Figure 4.13 we were unable to notice any difference in resistivity between the time steps t0 and t1. On the contrary, in Figure 4.14.a it is clear that a change in resistivity between the two measurements has occurred. In fact, below the infiltration box, we can clearly appreciate how the resistivity decreased following the start of the irrigation test. As the experiment continues, the infiltration depth increases but does not exceed 7-8 m. The presence of the clay layer at that depth, appreciable in Figure 4.14.g with a green colour where the resistivity variations are practically nil, prevents the water from further infiltrating vertically along that path. Despite this, even at greater depths, under the clay layer, there are perceptible decreases in resistivity, starting already from Figure 4.14.c, that gradually increase in size and values as the experiment continues. These negative changes in resistivity can be attributed to the presence of the downstream drainage trench. The latter allows the water to flow through it, to overcome the clay layer and thus to reach greater depths. In fact, we must consider that the water does not only infiltrate below the irrigation box but follows much more complicated paths in the three dimensions and which have allowed it to reach the drainage trench as well. These are important results because they demonstrate, in addition to the high impermeability of the clay layer, the correct working of the drainage trench. Finally, Figure 4.15 shows the obtained percentage changes in resistivity following the closure of the irrigation box.

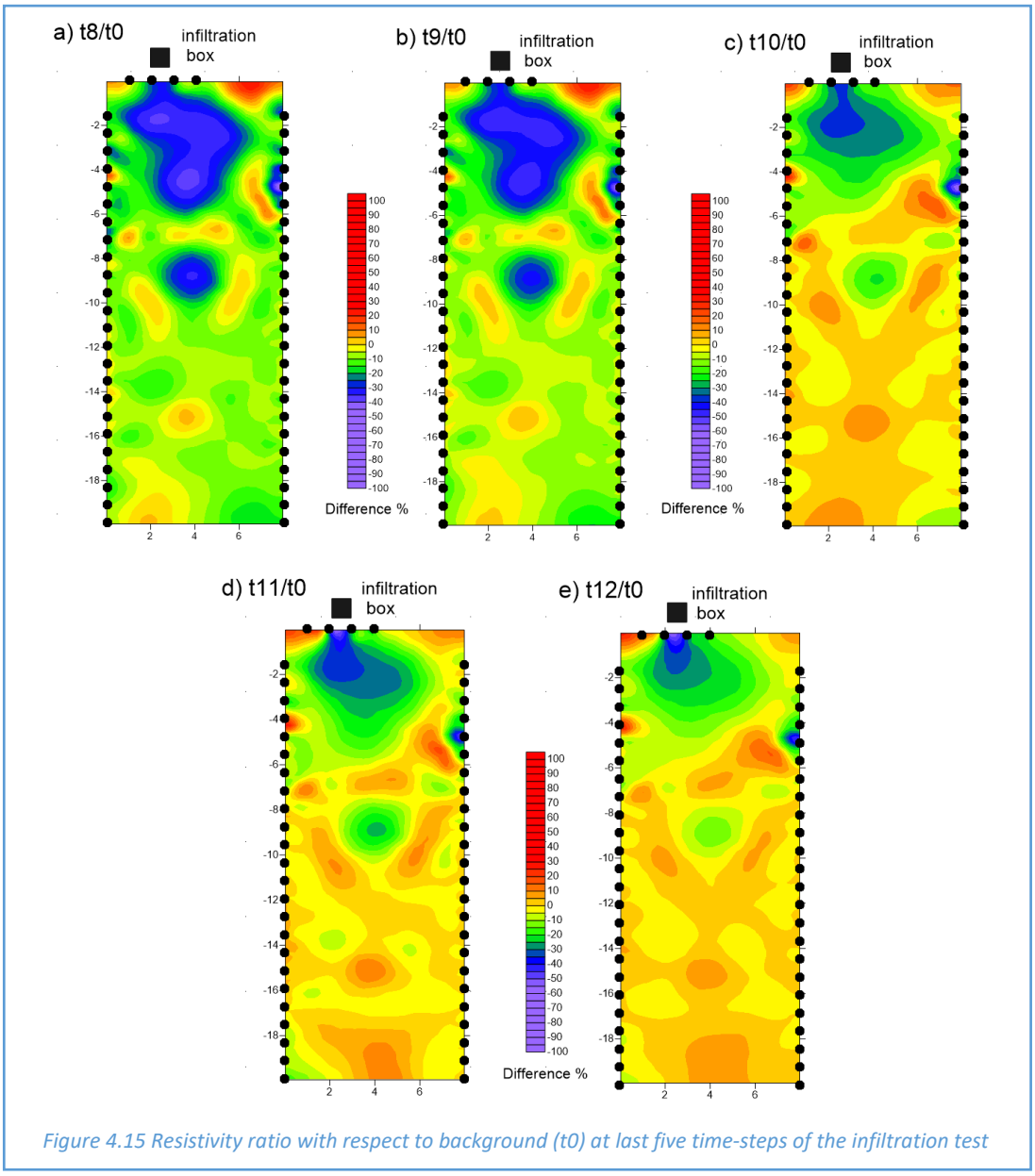

Figure 4.15 Resistivity ratio with respect to background (t0) at last five time-steps of the infiltration test

From Figure 4.15 we can appreciate how, even after the irrigation box has been closed, the changes in resistivity are still negative in the most superficial gravel layer. The clay layer in fact hinders the vertical infiltration of the water below the irrigation box and therefore the water tends to remain in the upper layer itself. Even after 18 hours from the end of irrigation (t12) the resistivity variations are still negative in the surface layer of gravel and this proves the high impermeability of the clay layer which does not allow the water to infiltrate vertically below the irrigation box, slowing down considerably the return to the initial conditions (t0) of the upper gravel layer itself. On the contrary, in the lower gravel layer, the resistivity values tend to return more quickly to the initial ones (t0) as the water, which arrived previously thanks to the draining trench, managed to infiltrate vertically. Moreover, also after stopping the irrigation, we can see clearly a negative resistivity variation area below the clay layer. This once again demonstrates the correct working of the drainage trench which allows the water, accumulated in the upper layer of gravel, to infiltrate even vertically, obviously only where the drainage trench is located (downstream from the location of the infiltration box). In conclusion we can say that the experiment clearly demonstrates the enormous potential of time-lapse investigations to study infiltration processes of the water in the subsoil, and therefore also of possible pollutants carried by the water itself, obviously only in case that the data processing is correctly performed using a ratio inversion approach to enhance the resistivity changes from one-time frame to the next.

5. SUMMARY

As all geophysical investigations, electrical surveys must be realized if we have a specific target and after having collected as much preliminary information as possible. Before carrying out the investigation, it is necessary to understand if the DC resistivity method is sensitive to the type of problem that we face, particularly if there are sufficiently high electrical conductivity contrasts in the subsoil. We must evaluate whether the target of the investigation can be identified, in particular we need to consider the size and depth of the target; as we have discussed in chapter 2, we cannot achieve deep and high resolutive investigations, since the number of electrodes is always limited. It is also necessary to consider if the survey is suitable, in terms of logistics issues that can limit survey length and extension. If possible, it is convenient to calculate forward models before carrying out field surveys, simulating the results that we can expect with the measurements in the field. This allows us to make assessments on the length and spacing of the electrode line that should be used (depending on the target of the survey and the environment), as well as on the most appropriate kind of configuration (Wenner, Dipole-dipole, etc). On the field, before starting the measurements, we need to check that all the electrodes are correctly connected and that the contact resistances are not too high. The measurements must be taken with the largest number of stacks as possible and, if possible, with reciprocals. This will allow us to evaluate the quality of our dataset and to realize an inversion process as coherent as possible. Even during the inversion process, we can use the prior knowledges about the site and the investigated target, to obtain a resistivity section that allows us to interpret the subsoil model as correctly as possible. Furthermore, image appraisal with sensitivity maps can offer great insight into the reliability of the final model, as well as being helpful to make assessments about the results and to define section boundaries in the best way possible.

From the analysis realized in chapter 3, we defined the importance of having a priori information regarding the investigation site and the use of them to create, before the measurements are performed in the field, direct models which can be used to define the best configuration of the electrodes line (length, spacing, type of array) able to highlight the target of the survey. For instance, if we consider the subsoil model of Figure 3.8.a and the target of the investigation is to detect the presence of a third more resistive layer with an ERT surface survey, we cannot use a 48-meter electrodes line but we must use lines of greater length and/or high skip. The use of high skip, while decreasing the resolution, guarantees greater penetration but tends to laterally shrink the validity of the resistivity section, particularly with a larger spacing of the electrodes. To face this last problem, we can use various skip together in order to preserve the great penetration of the survey and don't lose information laterally. An alternative is to use the roll-along technique, described in chapter 2.2.1. Obviously, in both cases, the duration of the measurements is considerably larger. Despite this, it should be noted that even if we are able to detect the presence of the third layer using the appropriate configuration of electrodes, its depth is significantly emphasized than the real one due to the current line concentration in the conductive layer and the excessive smoothing performed by the inversion code which make the thickness of the clay layer much greater than the real one. Thus, if the target of the investigation is to define the real thickness of an isolated clay layer, from the direct models that we have obtained, we are aware that we cannot do it only with an ERT surface survey, regardless of the electrode line configuration (length, spacing, type of array). For this kind of target, it is suggested to use the ERT cross borehole technique. The borehole ERT, even if presents some of the same problems, such possible artefacts due to the excessive smoothing

in the inverted resistivity section, allows us to accurately estimate the thickness of each layer, even if the spacing of the electrodes is greater than thickness of the conductive clay layer itself. Moreover, in the same chapter 3 we have shown that during the inversion process even with a discontinuous clay layer the same problems seen so far are encountered. On the other hand, the ERT surface technique allows us to easily detect the discontinuities if they have a similar size of the spacing of the electrodes. However, from the resistivity sections it is practically impossible to define the real length of the discontinuities, even using an electrode spacing smaller than the length of the discontinuity and adopting a logarithmic scale. Anyway, ERT surface surveys are very useful because usually, for the environmental purposes, the target is just to detect whether an impermeable clay layer is continuous or not, determining the location of the discontinuities. Examples of this kind of investigations have been reported in the study case of chapter 4. The surveys have been performed in the province of Pordenone (NE Italy) and has demonstrated the difficulty of the ERT surface technique to correctly estimate the thickness of a shallow clay layer (Figure 4.4) but at the same time it shows the reliability in detecting discontinuities of the same conductive layer (Figure 4.6). Instead, the use of the cross-borehole technique has allowed us to define with great precision the thickness of the clay layer, and therefore the correct structure of the subsoil under investigation. To extend the correct information even outside the area between the holes (Figure 4.12), it is possible to use simultaneously, during the inversion process, the datasets obtained from the surface survey and from the cross-borehole measurements. Finally, we have demonstrated the enormous potential of the ERT cross borehole technique to monitor infiltration processes of the water in the subsoil, through the time-lapse measurements described in chapter 2.2.3. This kind of investigation has been also carried out in the study case near Pordenone and the results obtained highlighted the high impermeability of the clay layer in the subsoil and the correct working of the draining trench located downstream of the survey site.

In conclusion, with this thesis, we want to demonstrate the great advantages to apply the ERT technique to shallow environmental and hydrological studies. In fact, the use of ERT investigations from surfaces allows us to evaluate the continuity of clay layers, which can act as aquicludes, without the need to drill the soil. Instead, to precisely define the structure of the subsoil, only surface ERT investigations are no longer enough but it is also necessary to integrate ERT cross-borehole surveys. This will allow us to define with extreme confidence the thickness of the layers, with different lithology or saturation in water, in the area between the two holes. Therefore, these types of geophysical surveys can give a significant contribution for the characterization of the investigated areas, providing considerable support for the correct knowledge of the subsoils under investigation. However, we must underline the importance of carefully plan the ERT surveys before their realization in the field (configuration, spacing, skip, position and length of the electrodes line) using a priori information and direct models. Moreover, it is important to carry out the inversion process of the datasets in the most appropriate way as possible evaluating the inversion error with the control of the reciprocal datasets. It is essential to follow all these indications if we want the surveys fit the requested targets or, even worse, to avoid wrong results due to inversion artifacts.

6. REFERENCES

- Anderson MP and Woessner WW. Applied groundwater modeling simulation of flow and advective transport. Academic Press. San Diego, California; 1992.

- Barker RD. A simple algorithm for electrical imaging of the subsurface. First Break 10(2), 53–62; 1992.

- Archie GE. The Electrical Resistivity Log as an Aid in Determining Some Reservoir; 1942.

- Binley A, Shaw B and Henry Poulter S. Flow pathways in porous media – electrical tomography resistance and dye stanning image verification. Meas. Sci. Tech. 7, 384-390; 1996.

- Binley A, Winship P, West LJ, Pokar M, and Middleton R. Seasonal variation of moisture content in unsaturated sandstone inferred from borehole radar and resistivity profiles. J. Hydrol. 267, 160–172; 2002.

- Binley A, Cassiani G, Middleton R, and Winship P. Vadose zone model parameterisation using crossborehole radar and resistivity imaging. J. Hydrol. 267, 147–159; 2002b.

- Binley A. http://www.es.lancs.ac.uk/people/amb/Freeware/Profiler/Profiler.htm (ProfileR version 2.5 October 2003).

- Binley A and Kemna A. DC resistivity and induced polarization methods. Rubin Y and Hubbard SS (editor in chiefs), Hydrogeophysics, pp. 129–156; 2005.

- Binley A. Tools and Techniques: Electrical Methods. Treatise on Geophysics, Gerald Schubert (editor in chief), 2nd edition, Vol 11. Oxford: Elsevier; pp. 233-259; 2015.

- Binley A. http://www.es.lancs.ac.uk/people/amb/Freeware/R2/R2.htm (R2 version 4.0 November 2019).

- Carulli GB, Della Vedova B, Podda F, Slejko D and Zanolla C. Carta delle unità geologiche della pianura del Friuli Venezia Giulia alla scala 1:150.000. Regione Autonoma Friuli Venezia Giulia; 2006.

- Cassiani G, Bruno V, Villa A, Fusi N, and Binley A. A saline trace test monitored via time-lapse surface electrical resistivity tomography. Journal of Applied Geophysics 59, 244–259; 2006.

- Cassiani G, Boaga J, Rossi M, Putti M, Fadda G, Majone B and Bellin A. Soil–plant interaction monitoring: small scale example of an apple orchard in Trentino, North-Eastern Italy. Science of the Total Environment 543, 851–861; 2016.

- Castiglioni GB. The eastern sector of the Italian Alps. In Gibbard P & Ehlers J - Quaternary Glaciations. Developments in Quaternary Science, 2, Part 1, 209-214; 2004.

- Clark PU, Dyke AS, Shakun JD, Carlson AE, Clark J, Wohlfarth B, Mitrovica JX, Hostetler SW and McCabe AM. The Last Glacial Maximum. Science, 325, 710-714; 2009.

- Constable S, Parker R, and Constable C. Occam's inversion: A practical algorithm for generating smooth models from electromagnetic sounding data. Geophysics 52(3), 289–300; 1987.

- Dahlin T and Loke MH. Quasi-3D resistivity imaging/mapping of three dimensional structures using two dimensional DC resistivity techniques. Proceedings of the 3rd Meeting of the Environmental and Engineering Geophysical Society, Aarhus, Denmark, pp. 143–146; 1997.

- Dahlin T. The development of DC resistivity imaging techniques. Computers and Geosciences 27, 1019–1029; 2001.

- Daily WD, Ramirez AL, LaBrecque DJ and Nitao J. Electrical resistivity tomography of vadose water movement. Water Resources Res. 28, 1429-1442; 1992.

- Daily WD, LaBrecque DJ, Ramirez Al and Barber W. Electrical resistance tomography experiments at the Oregon Graduate Institute. J. Appll. Geophys. 33, 227-237; 1996.

- Doetsch J, Coscia I, Greenhalgh S, Linde N, Green A, and Gunther T. The borehole-fluid effect in electrical resistivity imaging. Geophysics 75(4), F107–F114; 2010.

- Doetsch J, Linde N, Pessognelli M, Green AG, and Gunther T. Constraining 3D electrical resistance tomography with GPR data for improved aquifer characterization. Journal of Applied Geophysics 78, 68–76; 2012.

- Doetsch J, Linde N, Vogt T, Binley A, and Green A. Imaging and quantifying salt tracer transport in a riparian groundwater system by means of 3D ERT monitoring. Geophysics 77(5), B207–B218; 2012b.

- Fontana A. Tra Tagliamento e Livenza. In Bondesan A & Meneghel M - Geomorfologia della provincia di Venezia. Esedra, Padova, 195-217; 2004.

- Fontana A, Mozzi P and Bondesan A. Alluvial megafans in the Venetian-Friulian Plain (north-eastern Italy): Evidence of sedimentary and erosive phases during Late Pleistocene and Holocene. Quaternary International, 189, 71-90; 2008.

- Fontana A, Bondesan A, Meneghel M, Toffoletto F, Vitturi A and Bassan V. Note illustrative della Carta Geologica d'Italia alla scala 1:50.000 - Foglio 107 Portogruaro. Regione Veneto, Infocartografica, Piacenza: 2 fogli, 168 pp; 2012.

- Fontana A, Mozzi P and Marchetti M. Alluvial fans and megafans along the southern side of the Alps. Sedimentary Geology, 301, 150-171; 2014a.

- Fontana A, Monegato G, Rossato S, Poli ME, Furlani S and Stefani C. Carta delle unità geologiche della pianura del Friuli Venezia Giulia alla scala 1:150.000 e note illustrative. Regione Autonoma Friuli Venezia Giulia, Servizio Geologico, Trieste, 80 pp., 1 foglio allegato; 2019.

- French HK, Hardbattle C, Binley A, Winship P, and Jakobsen L. Monitoring snowmelt induced unsaturated flow and transport using electrical resistivity tomography. J. Hydrol. 267, 273-284; 2002.

- Gerya T. Introduction to numerical geodynamic modelling. Cambridge University Press; 2010.

- Geuzaine C. and Remacle JF. Gmsh: a three-dimensional finite element mesh generator with built-in pre- and post-processing facilities. International Journal for Numerical Methods in Engineering 79(11), pp. 1309-1331; 2009.

- Hippe K, Fontana A, Hajdas I and Ivy-Ochs S. A high-resolution 14C chronology tracks pulses of aggradation of glaciofluvial sediment on the Cormor megafan between 45 and 20 ka BP. Radiocarbon, 1-22; 2018.

- Kemna A. Tomographic inversion of complex resistivity—Theory and application, PhD Thesis, Bochum Ruhr-Univ., Germany (published by: Der Andere Verlag, Osnabrück, Germany); doi:10.1111/1365-2478.12013, 2000.

- Kemna A., Vanderborght J, Kulessa B, and Vereecken H. Imaging and characterisation of subsurface solute transport using electrical resistivity tomography (ERT) and equivalent transport models. J. Hydrol. 267, 125–146; 2002.

- La Brecque DJ, Ramirez Al, Daily WD, Binley A and Schima S. ERT monitoring of environmental remediation process. Meas. Sci. Tech. 7, 375-383; 1996.

- LaBrecque D and Yang X. Difference inversion of ERT data: Fast inversion method for 3D in situ monitoring. Journal of Environmental and Engineering Geophysics 6(2), 83–89; 2001.

- LaBrecque D, Heath G, Sharpe R, and Versteeg R. Autonomous monitoring of fluid movement using electrical resistivity tomography. Journal of Environmental and Engineering Geophysics 9, 167–176; 2004.

- Lewis FD, Johnson CD, Singha K and Lane JW. Best practices in electrical resistivity imaging: data collection and processing, and application to data from Corinna, Maine.

- Menke W. Geophysical Data analysis: Discrete Inverse Theory. New York: Academic Press; 1984.

- Monegato G, Ravazzi C, Donegana M, Pini R, Calderoni G and Wick L. Evidence of a two-fold glacial advance during the last glacial maximum in the Tagliamento end moraine system (eastern Alps). Quaternary Research, 68, 284-302; 2007.

- Monegato G, Scardia G, Hajdas I, Rizzini F and Piccin A. The Alpine LGM in the boreal ice-sheets game. Scientific Reports, 7, 1-8; 2017.

- Nimmer RE, Osiensky JL, Binley AM, and Williams BC. Three-dimensional effects causing artifacts in two-dimensional, cross-borehole, electrical imaging. Journal of Hydrology 359, 59–70; 2008.

- Osiensky J. Ground water modeling of mise-a-la-masse delineation of contaminated ground water plumes. J. Hydrol. 197, 146–165; 1997.

- Osiensky J, Nimmer R, and Binley A. Borehole cylindrical noise during hole-surface and hole–hole resistivity measurements. Journal of Hydrology 289, 78–94; 2004.

- Parasnis DS. Reciprocity theorems in geoelectric and geoelectromagnetic work. Geoexploration 25, 177–198; 1988.

- Park SK and Van GP. Inversion of pole–pole data for 3D resistivity structure beneath arrays of electrodes. Geophysics 56, 951–960; 1991.

- Pavoni M. Analysis of electrical resistivity tomography data uncertainty. Bachelor's Degree in Geological Sciences. Department of Geosciences, Padua; 2018.

- Ramirez A, Daily W, LaBrecque W, Owen E, and Chesnut D. Monitoring an underground steam injection process using electrical resistance tomography. Water Resour. Res. 29, 73-87; 1993.

- Ramirez Al, Daily WD, Binley A, LaBrecque DJ and Roelant D. Detection of leaks in underground storage tanks using electrical resistance methods. J. Environ. Eng. Geophys. 1, 189-203; 1996.

- Roy A and Apparao A. Depth of investigation in direct current methods. Geophysics 36(5), 943–959; 1971.

- Schima S, LaBrecque DJ and Lundegard PD. Using resistivity tomography to monitor air sparging. Ground Water Monitoring and Remediation 16, 131–138; 1996.

- Schmalholz SM and Kaus BJP. Introduction to finite element modelling in geosciences. ETH Zurich; 2008.

- Slater LD, Zaidman MD, West LJ and Binley A. Electrical imaging of saline tracer migration for the investigation of unsaturated zone transport mechanism. Hydrology and Earth System Sci. 1, 291-302; 1997.

- Slater L, Binley A, Daily W, and Johnson R. Cross-hole electrical imaging of a controlled saline tracer injection. J. Appl. Geophys. 44, 85–102; 2000.

- Slater L and Binley A. Synthetic and field based electrical imaging of a zerovalent iron barrier: Implications for monitoring long-term barrier performance. Geophysics 71(5), B129–B137; 2006.

- Tikhonov AN and Arsenin VY. Solutions of Ill-Posed Problems. New York: Wiley; 1977.

- Ursino N, Cassiani G, Deiana R, Vignoli G and Boaga J. Measuring and modelling water related soil–vegetation feedbacks in a fallow plot. Hydrol. Earth Syst. Sci. 18, 1105-2014; 2014.

- Van Schoor M and Binley A. In-mine (tunnel-to-tunnel) electrical resistance tomography in South African platinum mines. Near Surface Geophysics 8, 563–574; 2010.

- Vernon RW. Leo Daft and 'The Electrical Ore-Finding Company Limited'. Alfred Williams (editor in chief), British Mining 86: 4–30; 2008.

- Winship P, Binley A and Gomez D. Flow and transport in the unsaturated Sherwood Sandstone: characterization using cross-borehole geophysical methods. Barker, Tellam (Eds.), Fluid Flow and Solute Movement in Sandstones: The Onshore UK Permo-Triassic Red Bed Sequence. Geological Society, London, Special Publications 263, pp. 219–231; 2006.

- Zanferrari A, Avigliano R, Monegato G, Paiero G and Poli ME. Note illustrative della Carta Geologica d'Italia alla scala 1:50.000 - Foglio 066 "Udine". Graphic Linea, Tavagnacco, Udine, 176 pp; 2008a.

- Zanferrari A, Avigliano R, Grandesso P, Monegato G, Paiero G, Poli ME and Stefani C. Note illustrative della Carta Geologica d'Italia alla scala 1:50.000 - Foglio 065 "Maniago". Graphic Linea, Tavagnacco, Udine, 224 pp; 2008b.

- Zohdy A. A new method for the automatic interpretation of Schlumberger and Wenner sounding curves. Geophysics 54(2), 245–253; 1989.